Modelling sediment dynamics at the basin scale:

Implications of changes in climate and hydrological regimes

by

Kai Tsuruta

A THESIS SUBMITTED IN PARTIAL FULFILLMENT OF
THE REQUIREMENTS FOR THE DEGREE OF

DOCTOR OF PHILOSOPHY

in

The Faculty of Graduate and Postdoctoral Studies

(Forestry)

THE UNIVERSITY OF BRITISH COLUMBIA

(Vancouver)

November 2017

Abstract

Basin-wide sediment dynamics are closely linked to hydrological processes and landscape and therefore expected to be susceptible to climate change. Simulating sediment transport through large basins presents a challenging problem to modellers; the relationship between water flux and sediment load is complex and non-linear, and significant sediment generation can occur over small spatial and time scales. To date, most studies have employed lumped empirical models that predict annual load at the outlet of a study basin, but do not consider variability across the basin or sub-annually. In this study, we adapt a physically-based, distributed suspended sediment transport model for large-scale use. The sediment model is integrated into the Terrestrial Hydrology Model with Biochemistry (THMB) as a routine to make use of THMB's dynamic water routing. The coupled model is applied to the 230,000 km^2 Fraser River Basin (FRB) in British Columbia, Canada using 1) historical hydrological input to test the model and 2) synthetic input derived from Intergovernmental Panel on Climate Change (IPCC) scenarios A1B, A2, and B1 to study potential impacts of climate change. In both cases the input data is provided by the Pacific Climate Impacts Consortium (PCIC) and comes from simulations using the Variable Infiltration Capacity (VIC) model.

Simulation results using historical inputs are compared with observations at five stations using the coefficient of determination (R^2), Nash-Sutcliffe coefficient of efficiency (NSE), and percent bias (PBIAS) metrics. Overall, simulated load values match well with observed values, with the monthly simulations at the station nearest the outlet scoring $R^2 = 0.78$, NSE = 0.77, and PBIAS = -20%. Simulation results using climate scenario-driven inputs are studied for potential future changes in sediment dynamics. Results reveal a general shift in hillslope erosion and sediment yield towards larger values from autumn to spring, reduced summer values, and an overall annual increase, with hillslope generation growing 35-45% from baseline levels and yield at the basin's outlet increasing 10-15%. These physically-based results offer unique insights into the impacts of climate change on sediment processes within a large basin and their potential implications.

Lay Summary

Water quality and relative sea level rise are tied to the movement of mud and sand through river systems and therefore the dynamics of river basin sediment have important effects on humans and animals. Many studies have concluded that shifts in water dynamics and landscape are likely to arise due to changes in regional and global climate, but few have investigated the secondary effects of these changes on sediment, in part because appropriate models for such studies are rare. This work adapts a model capable of simulating sediment processes within a large basin and uses it to study the impacts of climate change in the Fraser River Basin in British Columbia, Canada. The study finds that warmer temperature and earlier snowmelt cause peaks in sediment erosion and yield to occur earlier in the year, potentially effecting the spawning cycle of fish within the system.

Preface

The contents of this manuscript represent the independent, original, and unpublished work of Kai Tsuruta. Chapters 2-4 have been written in preparation for submission to peer-reviewed journals. As a result, there is some overlap in the contents, mostly background and study site information, of these chapters. Citation formatting and references have been made uniform for consistency.

Table of Contents

Appendices

List of Tables

List of Figures

Acknowledgments

I am deeply grateful for the support and advice of my committee members throughout the process of creating this work. Younes Alila, Marwan Hassan, and Simon Donner have all provided deep insights and a considerable amount of their valuable time and energy. I consider them all to be my supervisors on this project in some way and could not have completed this manuscript without each of them. I must also thank Markus Schnorbus who provided the hydrological data to make this work possible, Doris Leong who helped acquaint me with the hydrological model used my study, Eric Leinberger who prepared the figures used in this manuscript, and Vincent Kujala whose technical support was indispensable.

Everything in life is speaking in spite of its apparent silence
- Hazrat Inayat Kahn

Love,

Tobi

Chapter 1

Introduction

1.1 Research Problem

The sediment dynamics of a river basin are dependent on the basin's water flux and landscape and therefore likely to be affected by climate change and anthropogenic activities such as damming or urbanization (*Walling* [2009]). Changes in these dynamics may have important consequences; suspended sediment yield and concentration levels can play significant roles in coastal retreat/advance (*Syvitski et al.* [2005]), contaminant transport and water quality (*Motew et al.* [2017]), and the health of aquatic biota (*Kerr* [1995]). Because of these potential implications, in recent years there has been a call, either directly or indirectly, to begin bolstering hydrological models with sediment transport routines. Unfortunately, there are currently few existing sediment transport models that adequately simulate the processes of sediment erosion, deposition, and transport (*Praskievicz and Chang* [2011]). To properly model these processes, *Smith et al.* [2011] and *Pelletier* [2012] argued the need for sediment models to be distributed, while *Bathurst* [2010] stated that physically-based, distributed models were the ones best suited for projecting climate-related changes to sediment. Lumped linear regression models commonly used to predict sediment loads from water flux do not account for any variability in sediment processes within the basin. This is problematic as significant sediment events can be highly localized in nature (*Smith et al.* [2011]). Distributed, empirical models such as the one presented in *Pelletier* [2012] can be useful for estimating current or historical sediment processes, but in order to make long-term projections, must assume that the driving empirical relationship remains stationary throughout the simulation period. By contrast, physically-based models rely on equations such as force and mass balance; these relationships are likely to remain valid in perpetuity.

Development of such a physically-based, distributed model is difficult. The transport of fine particle sediment is often supply rather than fluvially driven, which makes modelling sediment by water flux alone untenable. The relationship that does exist between sediment load and water flux is complex

and non-linear, meaning that any errors in water flux propagate and magnify in sediment load. Over large basins, these issues exist in addition to the challenges associated with modelling a highly localized phenomenon over a heterogeneous area at a coarse scale. While a handful of fine-scale mechanistic distributed models such as KINEROS (*Beasley et al.* [1980]), WEPP (*Nearing et al.* [1989]), and the model developed in *Patil et al.* [2012] exist, any attempt at upscaling one for large-scale use must resolve these issues of heterogeneity both within a coarse grid cell and throughout a large basin. Because of the difficulties associated with coarse resolution and upscaling, continental and regional scale models are still in their infancy (*Wood et al.* [2011]). Developing a large-scale, distributed, mechanistic model would provide a useful tool for studying long-term regional sediment processes and the potential changes to these dynamics due to climate or landscape shifts. The intent of this study is to adapt such a model and use it to investigate the role of shifts in climate and hydrology in changes to the sediment dynamics of a large basin.

1.2 Research Objectives and Strategies

The two primary goals of this research project are to 1) develop a mechanistic distributed sediment transport model for use on large river systems and 2) use the developed model to investigate the potential impacts of climate change on the sediment dynamics of a large-scale basin. To accomplish these goals, I identify four main objectives:

• Adapt the semi-distributed, small-scale mechanistic sediment transport model developed in *Patil et al.* [2012] for use on large-scale basins.

• Validate the adapted model against observed data within British Columbia, Canada's Fraser River Basin (FRB).

• Simulate future sediment dynamics within the FRB using the validated model with hydrological data derived from future emission scenarios.

• Investigate potential future changes in the sediment dynamics of the FRB.

Physical characteristics of the FRB are described in Chapters 2-4. The basin was chosen for our study because it is large, relatively free of anthropogenic influences, and culturally and economically important to the

province of British Columbia (B.C.). Additionally, observed data as well as the necessary climatic input data for both historical and climate scenario simulations are available for the FRB. Details of the model developed in *Patil et al.* [2012] are given in Chapter 3. It was chosen for adaptation because it is mechanistic, distributed, relatively computationally inexpensive, and has been shown to be effective on a small scale.

To accomplish my research objects, I first integrate the model developed in *Patil et al.* [2012] as a sediment routine in the Terrestrial Hydrology Model with Biochemistry (THMB), a dynamic hydrological routing model. Next, I identify the major controls on sediment dynamics that need to be included or modified in the large-scale adaptation of the *Patil et al.* [2012] model. Once these changes are implemented, I run historical sediment simulations, driving the transport model with outputs from a historical run of the Variable Infiltration Capacity (VIC) land surface hydrological model. Outputs from the VIC simulations were provided by the Pacific Climate Impacts Consortium (PCIC) and not performed in this study. To test the adapted sediment transport model, simulated sediment loads are compared to historical observations. Once the ability of the transport model to match historical sediment loads is established, it is run from 1965-2094 using as drivers the results from climate scenario-driven simulations of VIC performed in *Shrestha et al.* [2012]. Potential future changes in sediment dynamics are then investigated by comparing dynamics from 1965-1994 to those of 2065-2094.

1.3 Structure of Dissertation

The structure of this dissertation is intended to systematically detail the work performed towards accomplishing the stated research objectives and goals. While chapters build upon the contents of previous chapters, each is intended to be self-contained. Hence, several chapters have overlapping information such as background details and study site descriptions. The primary purpose of each chapter is as follows:

Chapter 1: Introduction of research problem, objectives, and structure.

Chapter 2: Description of gridded river direction computations. This chapter details the novel method used to generate river directions which accurately describe the Fraser River. The method is assessed by comparing the sub-basin areas it delineates to values reported by the Water Survey of Canada (WSC). A comparison of our method to more standard methods is

also given.

Chapter 3: Adaptation of the *Patil et al.* [2012] model and validation against observed historical data. The model of *Patil et al.* [2012] is adapted for large-scale basins and run on the FRB using a historical run of VIC provided by PCIC. Model performance is evaluated by R^2, Nash-Sutcliffe Efficiency, and percent bias metrics. As an example of the model's utility, the FRB's sediment dynamics are simulated and analyzed beyond the period of available observations.

Chapter 4: Simulations of sediment dynamics under climate change scenarios. The adapted model is run on the FRB using as inputs the results of climate scenario-driven VIC simulations performed by PCIC in *Shrestha et al.* [2012]. Potential future changes in sediment dynamics are investigated by comparing a historical period to a future period. Basin-wide hillslope generation, storage, sediment yield, inter-annual peak sediment load variability, and sediment hydrograph timing are analyzed as are inter-scenario and inter-model variability.

Chapter 5: Conclusions, implications, and future work. General conclusions regarding the results of my work are given. Implications for humans, habitat, and biota are described. Strengths and limitations of the research methods used are discussed as is potential future work in evolving the adapted model and applying it to other basins for other purposes.

Chapter 2

River Delineation

2.1 Introduction

River direction and slope play an important role in large-scale distributed water and sediment transport modelling. Global studies such as *Syvitski et al.* [2003] have found long-term sediment yield to depend non-linearly on topographic relief. However, river networks and slopes are difficult to resolve at global scales using coarse ($\sim 5^\circ$ lat $\times 5^\circ$ lon) digital elevation maps (*Pelletier* [2012]). Intuitively, this difficulty is not surprising as the portion of a 5° lat $\times$ 5° lon grid cell (in our study site $\sim$ 25km^2) that is considered "river" is relatively small and therefore does not play a large role in the cell's topographical value.

Studies such as *Coe* [2000] and *Leong and Donner* [2015] used 5° lat $\times$ 5° lon river direction maps from the Center for Sustainability and the Global Environment (SAGE) at the University of Wisconsin-Madison which were derived from the Global DEM5 digital elevation model (*GETECH* [1995]) and manually adjusted to improve accuracy. However, this method doesn't address the issue of inaccurate river slopes and presents no clear method for how to rescale the map to other resolutions. Furthermore, depending on the study basin, manual correction may be impractical because of the number of cells requiring adjustment.

In *Pelletier* [2012], the author avoided defining river slopes as simply the topographic difference between a cell and its lowest neighbor and instead assigned the slope as the maximum of this value and the cell's topographic value divided by its along-channel distance to the ocean. In this way, the slope took on the value of the first type in mountainous regions and the second type for relatively low-gradient rivers. Still, this method does not illuminate how to accurately assign river direction so that "along-channel distance" can be properly defined. Efforts in our study site to assign river direction using steepest descent alone have proven to be highly inaccurate.

In this work, as part of a larger effort to model sediment transport, we present a simple method to define gridded, basin-wide river direction and slope and apply the method to the Fraser River Basin (FRB) in British

Columbia, Canada to generate river direction and slope at a scale matching that of the sediment transport model (1/16° lat × 1/16° lon). The principal idea is to use a weighted "topographic" map to compute direction and slope with the weights being determined by fine resolution flow accumulation. In this way, sub-grid "river" cells (those that accumulated the most flow) are more influential in the computation of the coarse grid cell's topographic value. Though other automated upscaling techniques that make use of sub-grid cell data exist (e.g. *Arora and Boer* [1999]; *Döll and Lehner* [2002]), we do not make comparisons between our algorithm and these methods. Instead, we present our computation as a simple alternative to the standard gradient descent and compare our results to this method.

2.2 Study Site and Input Data

2.2.1 Study Site

The 230,000 km^2 FRB is the largest watershed in British Columbia. The main stem of the Fraser River runs 1,400 km from headwaters in the Rocky Mountains to its outlet into the Pacific Ocean at Vancouver. The basin is often divided into three regions: i) an eastern mountain portion (Rocky Mountains), ii) an interior plateau, and iii) a coastal mountain portion. The mountainous eastern portion has the highest elevations and is characterized by steep valleys shaped by glaciers, while the interior plateau has the lowest mean elevation and is characterized by relatively low topography and topographical gradient (Figure 2.1). The diverse terrain within the FRB provides an opportunity to test our river delineation method under a variety of topographical conditions.

While the hydrology of the FRB has been extensively studied and modelled, to the author's knowledge, no accurate distributed river map for the basin is readily available. Modelling efforts such as *Schnorbus et al.* [2010] and *Shrestha et al.* [2012] have instead relied on transfer functions to estimate flow from sub-basins. However, more dynamic distributed hydrological models such THMB require a distributed river direction map. Efforts to assign river direction within the FRB using a topographic map have proven to be highly inaccurate at the 1/16° scale (see Section 2.4), presenting a need for an alternative method to generate accurate, coarse scale river direction maps for the FRB.

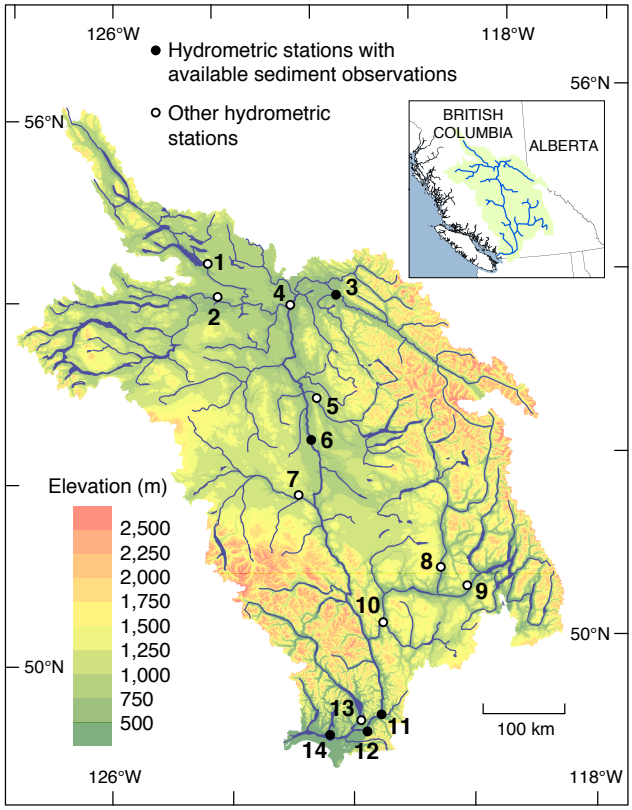

Figure 2.1: Fraser River Basin (FRB) topography and river network. Numbers 1-14 correspond to the hydrometric stations (Table 2.1) used in this study.

Table 2.1: Hydrometric stations used in study and corresponding sub-basins.

Station number	Sub-basin name	WSC ID	Sub-basin area ([km^2])	Station number	Sub-basin name	WSC ID	Sub-basin area ([km^2])
1	Stuart	08JE001	14600	8	North Thompson	08LB064	19600
2	Nechako	08JC001	25100	9	South Thompson	08LE031	16200
3*	Hansard	08KA004	18000	10	Thompson	08MF005	54900
4	Shelley	08KB001	32400	11*	Hope	08MF005	217000
5	Quesnel	08KH006	11500	12*	Agassiz	08MF035	218000
6*	Marguerite	08MC018	114000	13	Harrison	08MG013	7680
7	Chilcotin	08MB005	19300	14*	Mission	08MH024	228000

* Indicates stations with available sediment observations.

2.2.2 Input Data

The primary input data used in this study is the United States Geological Survey's 15 arc-second Global Multi-resolution Terrain Elevation Data (GMTED) map (*Danielson and Gesch* [2011]). We use the GMTED map, despite the existence of finer resolution digital elevation maps (SRTM, ASTER), because of its immediate availability to the authors and level of performance in this study (see Section 2.4). In the FRB, 15 arc-seconds corresponds to roughly 460 m $\times$ 260 m at 56° lat and 460 m $\times$ 310 m at 48° lat. Due to the change in absolute area of grid cells from north to south within the basin, southern grid cell's should be viewed as having a lower resolution than northern cells.

We evaluate our results at 14 FRB sub-basins using sub-basin areas reported by the Water Survey of Canada (WSC) (Table 2.1) and visually using a rivers and lakes map provided by the Canadian Ministry of Energy and Mines (CMEM) (Figure 2.1).

2.3 Methods

To determine river direction at the $1/16° \times 1/16°$ scale, we first assign river direction at the 15 arc-second scale using the topographic map TM_{15} provided by *Danielson and Gesch* [2011] (Figure 2.2a). For a given 15" cell $(i,j)_{15}$, we assign a downstream cell $(i + \mathrm{lon}_\delta, j + \mathrm{lat}_\delta)_{15}$ corresponding to the neighbor of $(i,j)_{15}$ with the lowest topography. Here variables lon_δ and lat_δ can each take any value from the set $\{-1, 0, 1\}$. Using the 15" river direction map DM_{15} we can determine the river's path from any given cell within the basin to the basin's outlet. A 15" flow accumulation map AM_{15} is generated by assigning to each cell $(i,j)_{15}$ a value equal to the number of cells whose paths go through $(i,j)_{15}$ (Figure 2.2b).

Next, a $1/16° \times 1/16°$ weighted "topographical" map $\mathrm{TM}^{\mathrm{w}}_{1/16}$ is generated from TM_{15} using AM_{15} as weights (Figure 2.3a). For a given 1/16° cell $(i,j)_{1/16}$, we compute its value in $\mathrm{TM}^{\mathrm{w}}_{1/16}$ as

$$\mathrm{TM}^{\mathrm{w}}_{1/16}(i,j) = \frac{1}{N \cdot AS(i,j)_{1/16}} \sum_{(k,l)_{15} \in (i,j)_{1/16}} \mathrm{TM}_{15}(k,l) \cdot \mathrm{AM}_{15}(k,l), \quad (2.1)$$

where, $(k,l)_{15} \in (i,j)_{1/16}$ denotes the set of all 15" cells $(k,l)_{15}$ within

$(i,j)_{1/16}$, N is the size of this set, and

$$AS(i,j)_{1/16} = \sum_{(k,l)_{15} \in (i,j)_{1/16}} \mathrm{AM}_{15}(k,l). \tag{2.2}$$

A 1/16° river direction map $\mathrm{DM}^{\mathrm{w}}_{1/16}$ and flow accumulation map $\mathrm{AM}^{\mathrm{w}}_{1/16}$ are then generated from $\mathrm{TM}^{\mathrm{w}}_{1/16}$ by methods analogous to those used to generate DM_{15} and AM_{15}.

To evaluate $\mathrm{DM}^{\mathrm{w}}_{1/16}$, we analyze the map's ability to delineate the 14 sub-basins listed in Table 2.1 by comparing the sub-basin areas determined by $\mathrm{AM}^{\mathrm{w}}_{1/16}$ to those reported by WSC. Additionally, to place our results in the context of standard river direction maps, we create un-weighted 1/16° river direction and flow accumulation maps $\mathrm{DM}^{\mathrm{uw}}_{1/16}$ and $\mathrm{AM}^{\mathrm{uw}}_{1/16}$ for a standard 1/16° topographical map $\mathrm{TM}^{\mathrm{uw}}_{1/16}$ and compute the corresponding sub-basin areas.

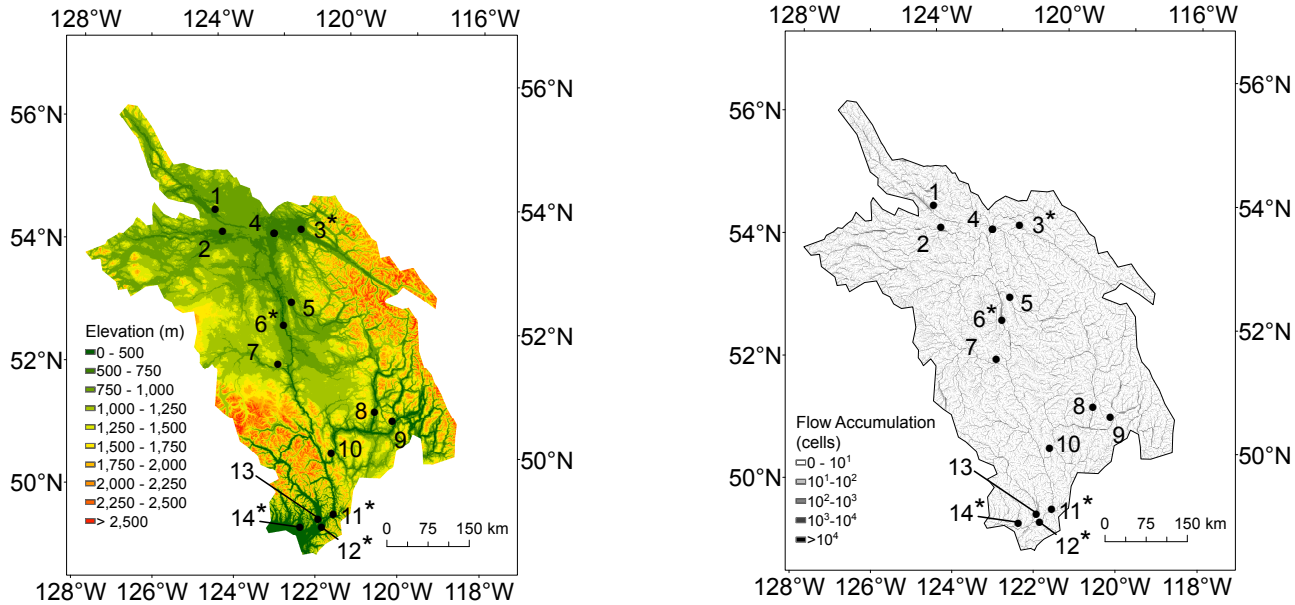

(a) TM_{15}

(b) AM_{15}

Figure 2.2: 15 arc-second a) topographical map TM_{15} and b) flow accumulation map AM_{15}.

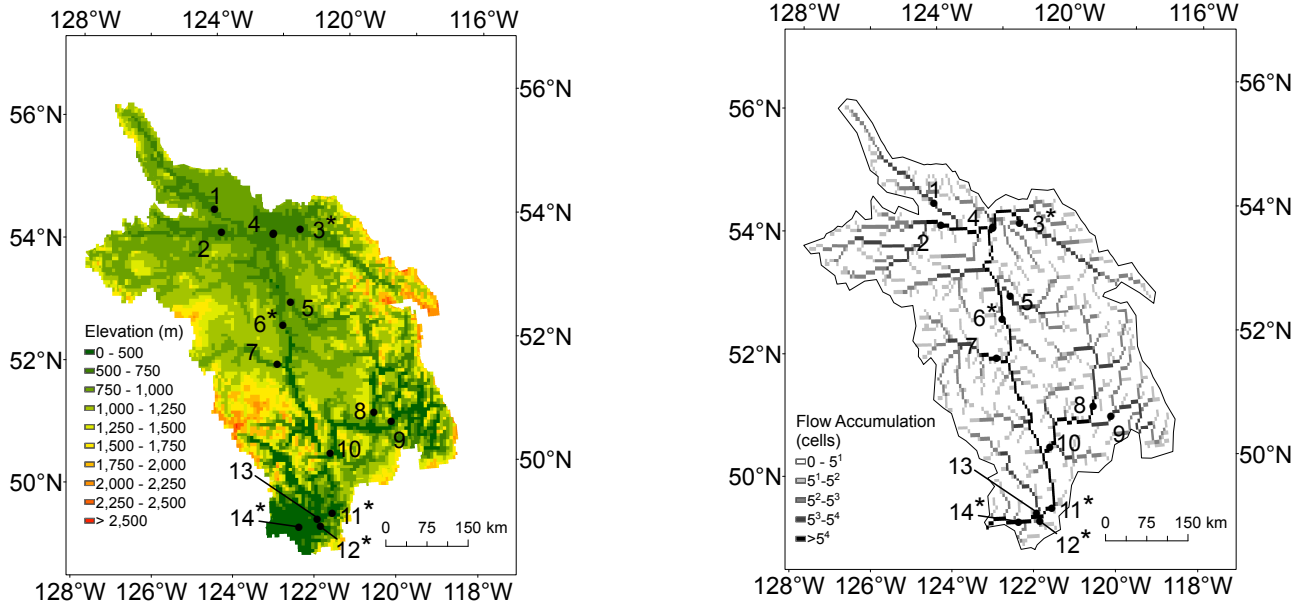

(a) $TM^{w}_{1/16}$

(b) $AM^{w}_{1/16}$

Figure 2.3: 1/16° weighted a) "topographical" map $TM^{w}_{1/16}$ and b) flow accumulation map $AM^{w}_{1/16}$.

2.4 Results

The percent difference between the sub-basin area determined by $\mathrm{AM}^{\mathrm{w}}_{1/16}$ and the area given by WSC was under 10% in 13 of 14 basins; Hansard, the remaining sub-basin, had a percent difference of 20% (Table 2.2). Sub-basin area results using $\mathrm{AM}^{\mathrm{w}}_{1/16}$ were better than the results using $\mathrm{AM}^{\mathrm{uw}}_{1/16}$ for 13 of the 14 sub-basins. At the remaining watershed, Quesnel, the percent error of the calculated area was 9% using both $\mathrm{AM}^{\mathrm{w}}_{1/16}$ and $\mathrm{AM}^{\mathrm{uw}}_{1/16}$. In many of the sub-basins, the percent error in basin area using $\mathrm{AM}^{\mathrm{w}}_{1/16}$ was one to two orders of magnitude smaller than the results using $\mathrm{AM}^{\mathrm{uw}}_{1/16}$. For instance, three mutually disconnected watersheds: Stuart, Nechako, and South Thompson had un-weighted percent area differences of 137%, 363%, and 134%, respectively and weighted percent area differences of 7%, 1%, and 3%. The basin as a whole was not well delineated by $\mathrm{AM}^{\mathrm{uw}}_{1/16}$, which under predicted the area upstream of Mission by 100% (compared to a prediction within 1% by $\mathrm{AM}^{\mathrm{w}}_{1/16}$).

The un-weighted method's most problematic areas appear to occur within the interior plateau where $\mathrm{AM}^{\mathrm{uw}}_{1/16}$ prescribes a large sink between the Nechako and Shelley outlets and near the transition from the interior plateau to the coastal mountains where $\mathrm{AM}^{\mathrm{uw}}_{1/16}$ disconnects the north-western and south-eastern parts of the basin (Figure 2.4c). On the other hand, strictly mountainous watersheds, such as Harrison and Hansard, were delineated with generally lower percent area differences (32% and 7% for Hansard and Harrison, respectively).

.

Table 2.2: Comparison of sub-basin area as reported by WSC and as computed by $AM^{w}_{1/16}$ (W) and $AM^{uw}_{1/16}$ (UW)

Station number	Sub-basin name	Sub-basin area ([km^2])	W ΔArea (%)	UW ΔArea (%)
1	Stuart	14600	-7	137
2	Nechako	25100	- 1	363
3	Hansard	18000	-20	32
4	Shelley	32400	<1	-26
5	Quesnel	11500	9	-9
6	Marguerite	114000	1	-65
7	Chilcotin	19300	6	34
8	North Thompson	19600	4	-22
9	South Thompson	16200	3	134
10	Thompson	54900	-2	-93
11	Hope	217000	<1	-94
12	Agassiz	218000	<1	-89
13	Harrison	7680	5	7
14	Mission	228000	<1	-100

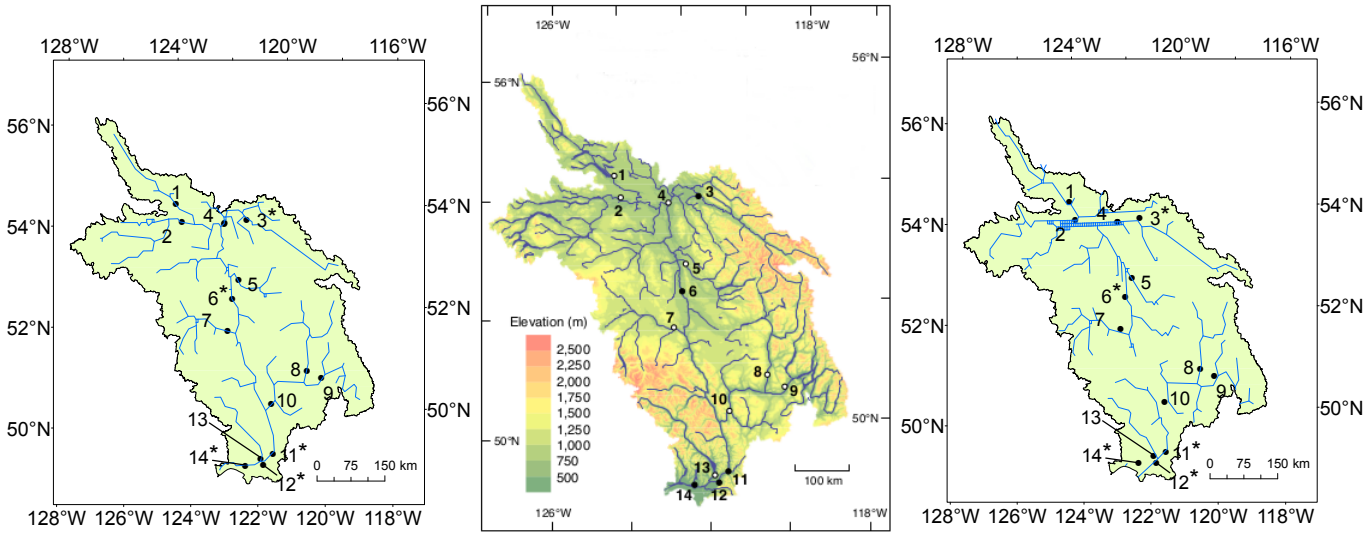

(a) $\mathrm{RM}^{\mathrm{w}}_{1/16}$ (b) CMEM (c) $\mathrm{RM}^{\mathrm{uw}}_{1/16}$

Figure 2.4: Main FRB river system as delineated by various methods.

2.5 Discussion and Conclusions

Using watershed area as a metric, river delineation by a weighted "topographical" map out-performed standard upscaling techniques in 13 of the 14 FRB sub-basins studied in this work. In many of these watersheds, the difference in performance was on the order of one to two magnitudes. At the remaining sub-basin, both methods performed equally well. The weighted method appears to be particularly advantageous in the interior plateau, where topographic gradients between cells are relatively small. In this region, the standard method did not properly connect the upper portion of the basin to its outlet, instead prescribing a sink in the northern region of the watershed. The results of the interior plateau suggest that the weighted method of river delineation may be advantageous in other low-gradient basins such as the Mississippi and many of its sub-basins.

By the area metric, the most problematic sub-basin for the weighted method was the Hansard watershed within the Rocky Mountains whose calculated area was 20% different from its reported area. The Nechako sub-basin, located in the north-western portion of the FRB also had some struggles regarding river direction within its lakes. Fixing these issues required 24 of the 7,771 cells in $\mathrm{DM}^{\mathrm{w}}_{1/16}$ be manually corrected using physical maps, at which point all sub-basins had a computed area within 10% of the WSC reported area. Conversely, because of the large area differences in multiple, disconnected sub-basins, it is questionable if similar performance is even feasible by manual correction of $\mathrm{DM}^{\mathrm{uw}}_{1/16}$.

Finally, though the weighted method of river delineation appears to have performed well in the FRB, care must be applied when using a weighted "topographic" map for other purposes. We suggest that while it is reasonable to use such maps to identify river direction and slope, for general topographical purposes a standard upscaled map is more appropriate as, by its construction, $\mathrm{TM}^{\mathrm{w}}_{1/16}$ is biased towards the lowest portions within a grid cell.

Chapter 3

Model Development and Historical Simulation of the FRB

3.1 Introduction

Changes to the sediment dynamics of the world's large river basins can have important consequences to humans and biota both within the basin and globally. Terrestrial sedimentation is considered an active carbon sink on the global scale (*Walling* [2009]; *Stallard* [1998]; *Harden et al.* [1999]; *Van Oost et al.* [2007]); reservoir sedimentation has been shown to effect the efficiency of dams and their long-term ability to provide energy and control over downstream water flux (*Schleiss et al.* [2016]); sedimentation in delta regions can play significant roles in coastal retreat/advance (*Syvitski et al.* [2005]) and floodplain agriculture (*Manh et al.* [2015]); and suspended sediment yield and concentration levels are closely tied to contaminant transport and water quality (*Motew et al.* [2017]) and the health of aquatic biota (*Kerr* [1995]; *Sternecker et al.* [2013]). Understanding the dynamics of suspended sediment across large river basins is therefore important for predicting how changes in land use or climate can impact the basin and its inhabitants and making appropriate land management and policy decisions.

Prediction of fine sediment transport remains a difficult problem. For many watersheds, suspended sediment is largely supply controlled, yet the principal sediment sources and processes controlling hillslope entrainment and delivery to the river channel are complex and not well understood (*Collins and Walling* [2004]). Many of these processes occur over relatively short time and spatial scales making them difficult to observe and model throughout a large basin. Furthermore, supply limitations make the relation between fine sediment transport and water flux complicated and indirect. Exacerbating these complexities is the understanding that erosion, transport, and deposition of fine sediment are non-linear processes with re-

spect to both supply and water flux. Hence, small errors in these inputs can translate into large errors in sediment transport (*Smith et al.* [2011]).

Despite these challenges, many attempts have been made to predict sediment loads. Because sediment dynamics are closely linked to hydrology (*Walling* [2009]), a common method to estimate sediment loads is to employ an empirical model that uses observational analysis to relate sediment to more fundamental hydrological variables such as water flux or river slope. A number of these empirical sediment models that are used for large-scale studies (*Hovius* [1998]; *Syvitski et al.* [2003]; etc.) are lumped and only predict load at the basin-scale with no consideration of variability within the basin (*Pelletier* [2012]). *Smith et al.* [2011] and *Pelletier* [2012] both argued that because a large portion of sediment within a basin is often supplied by small, low-order streams, a spatially distributed model is essential. Distributed empirical models have been developed in *Prosser et al.* [2001] (SEDNET) and *Pelletier* [2012]; however, both models run at an annual temporal scale and are not suited to capture the individual events that *Smith et al.* [2011] argued can characterize annual sediment load. A problem common to both lumped and distributed empirical models is the assumption of stationarity: that the underlying characteristics of the watershed will remain unchanged throughout the simulation. Assuming stationarity limits the ability of empirical models to study changes within the catchment such as land use or climate change.

For small scale basins ($< 50\ \mathrm{km}^2$), several distributed or "semi-distributed," mechanistic models have been developed, including ANSWERS (*Beasley et al.* [1980]), KINEROS (*Smith* [1981]), WEPP (*Nearing et al.* [1989]), and perhaps the most commonly used transport model, SWAT (*Arnold et al.* [1998]; *Arnold and Fohrer* [2005]). Typically, the computational and data demands of these models are intensive and simulations are restricted to smaller basins for discrete events (i.e. days) (*Srinivasan and Engel* [1994]; *Elliott et al.* [2012]). However in *White et al.* [2014], the authors were able to simulate long-term sediment and nutrient transport in the Mississippi Basin using SWAT. In part, this large-scale use of SWAT was possible because the model is "semi-distributed" in the sense that it does not simulate sediment dynamics on a cell-by-cell basis, but rather divides a watershed into sub-watersheds and further divides these sub-watersheds into hydrologic response units (HRUs) that are treated as homogeneous (*Gassman et al.* [2007]). However, *White et al.* [2014] only evaluated the simulation's ability to reproduce long term (47 year) annual averages and did not demonstrate that SWAT was capable of simulating inter-annual or even year-to-year variability in sediment yields.

Modelling sediment transport across large scales (>1000 km^2) is challenging because of the heterogeneity of the land surface and climate. A large basin can host a range of climates, vegetation, soils, land uses, topography, and landscape history, that create high spatial variability in sediment erosion, deposition, and transport across the basin. Low order streams with conducive physical characteristics such as steep slopes and high sediment supply can act as significant sediment sources (*Smith et al.* [2011]). However, computational and data limitations typically necessitate a coarse spatial resolution and a number of lumped, or partially lumped, parameters. Such limitations can restrict a model's ability to describe key processes and physical features such as river slope, which has been shown to be inaccurate when calculated directly from coarse resolution elevation data (*Singh and Frevert* [2002]; *Wu et al.* [2011]), or lead to heavily parameterized models which are challenging to calibrate and suffer from equifinality (*Kumarasamy and Belmont* [2017]; *Beven* [2006]). To assess sediment load at a large scale, physically-based, distributed models should resolve these issues of heterogeneity.

Patil et al. [2012] developed a physically-distributed model that was tested on a small basin (<50 km^2), but is well-suited to modification for large-scale applications. It is semi-distributed in the sense that it divides a watershed into several Representative Elementary Watershed (REW) reaches which are treated as homogeneous, it is relatively computationally simplistic, and is effective at estimating sediment load on a small scale. Its simulation of Goodwin Creek, a sub-watershed of the Mississippi, correlated well with observed data for daily, monthly, and annual sediment loads. Though upscaling any model for use on large, heterogeneous basins has a number of difficult challenges, the specific characteristics of the model in *Patil et al.* [2012] make it a viable candidate for such an adaptation.

In this chapter, we adapt and expand the work of *Patil et al.* [2012] into a mechanistic, distributed and size-selective sediment transport model for large river basins. The sediment model is integrated into the Terrestrial Hydrology Model with Biochemistry (THMB) presented in *Coe* [2000], making use of the dynamic water routing in THMB to simulate water flux as well as hydraulic geometry. A preliminary version of this integrated modelling system was used to simulate sediment-bound phosphorus transport through a moderately-sized (1,000 km^2) Midwest U.S. watershed (*Motew et al.* [2017]). The integrated model is driven by outputs provided by the Pacific Climate Impacts Consortium (PCIC) from their simulation of the FRB's land-surface hydrology using the generalized Variable Infiltration Capacity (VIC) model. The VIC simulation results are derived from historical climate

and precipitation data; details are provided in *Shrestha et al.* [2012]. We test the integrated model by simulating historic sediment transport within the Fraser River Basin (FRB), a 230,000 km^2, complex watershed in SW British Columbia, Canada. After the model's ability to reproduce observed loads has been verified, we demonstrate the model's utility by simulating sediment dynamics within the FRB from 1965-2004, analyze spatial and temporal trends during this period, and compare the annual basin yield from 1987-2004 (when no long-term observed sediment load data is available) to the yield from 1965-1986 (when observed sediment load is available). This paper describes the model framework, testing of the model against historical monthly river discharge and suspended sediment loads at five stations across the basin, analysis of model limitations and parameter sensitivity, and the results of a 40-year simulation of sediment transport across the FRB.

3.2 Models

3.2.1 Model Overview

The sediment routine is integrated into the hydrological routing and biogeochemical cycling model THMB and driven by precipitation, surface runoff, and subsurface drainage from VIC. At each time step and grid cell, THMB provides dynamic water fluxes and hydraulic geometry to the sediment model. The sediment routine then uses these variables along with landscape data to calculate erosion, deposition, and transport of suspended mud (<0.0625 mm) and fine sand (0.0625-0.5 mm) at each time step and grid cell (Figure 3.1). Simulations for this study are conducted at a 1 hour time step and a 1/16° latitude × 1/16° longitude spatial resolution.

Below, we briefly describe VIC, THMB, and the sediment routine adapted and expanded from *Patil et al.* [2012]. For more detail on the VIC model, the reader is referred to *Liang et al.* [1994] and *Liang et al.* [1996] for its development and *Schnorbus et al.* [2011] and *Shrestha et al.* [2012] for details on the VIC simulation that created the climate drivers for this study. For more details on THMB, the reader is referred to *Coe* [2000] and *Coe et al.* [2008].

3.2.2 Land-Surface Hydrology Model: VIC

VIC is a land surface hydrological model developed in *Liang et al.* [1994] and *Liang et al.* [1996]. It is intended for incorporation into general circulation models (GCMs) which simulate the circulation of the Earth's atmosphere

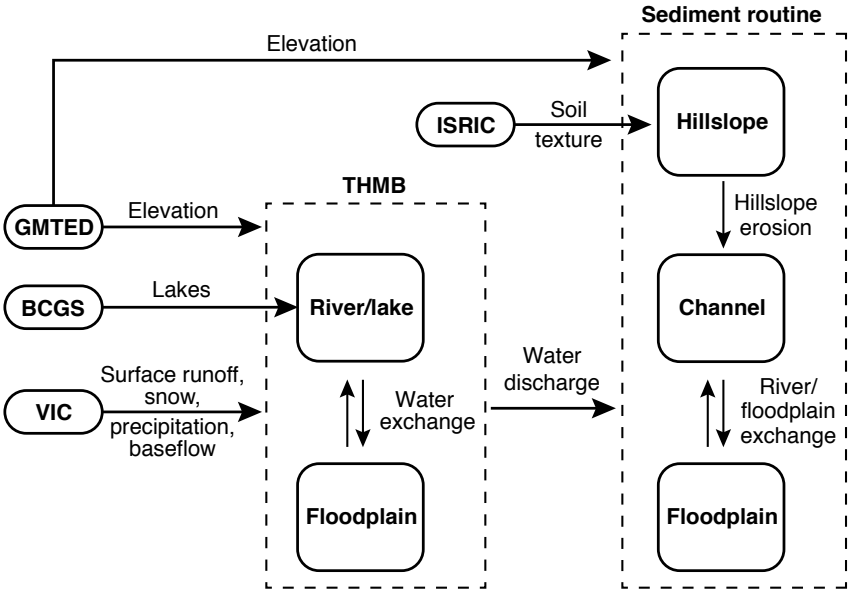

Figure 3.1: Flowchart of models used

and are often used for projecting changes in climate resulting from alterations in greenhouse gas emissions. VIC is forced by precipitation, maximum and minimum daily temperatures, and wind speed. Drivers for our study are provided by a previous historical run of VIC performed in *Shrestha et al.* [2012] accessed from *PCIC* [2014]. In that study, 61 sub-basins of the FRB were delineated using Water Survey of Canada (WSC) gauge data from Environment Canada (EC). Five model parameters and their probable ranges were chosen based on previous success in calibrating VIC for the FRB in *Schnorbus et al.* [2011]. These parameters were: the variable infiltration curve parameter, soil moisture content at which non-linear flow occurs, baseflow velocity at which non-linear flow occurs, maximum baseflow velocity, and the variation of hydraulic conductivity with soil moisture.

These parameters were calibrated using the Multi-Objective Complex Evolution Method developed in *Yapo et al.* [1998]. This method allows for the incorporation of several "objective functions" which calibration attempts to maximize. The objective functions chosen typically measure different ways in which a model deviates from physical observations and thus when used in concert give a more holistic view of the model's performance. In *Shrestha et al.* [2012], three metrics of model performance were used as objective functions: the Nash-Sutcliffe coefficient of efficiency (NSE), the Nash-Sutcliffe coefficient of efficiency of the log-transformed discharge (LNSE), and the water balance error. These metrics indicate the overall fit, fit of low flow, and fit of cumulative discharge, respectively. Of the three metrics, the NSE is most sensitive to extreme high values and is therefore likely best suited to evaluate the model's ability to characterize the high flows during which sediment transport is ostensibly highest.

Validation of the calibrated VIC was then performed for a 5-year period on 11 sub-basins. Results are given in detail in *Shrestha et al.* [2012]. Generally, peak discharge was matched closely throughout most sub-basins and years with NSE and LNSE values being greater than 0.70 for 9 of 11 sub-basins.

3.2.3 Water Routing Model: THMB

THMB simulates the time-dependent flow and storage of water and nutrients in rivers, lakes, wetlands, and human-made constructions such as dams. The model has been used to simulate several North American basins including the Athabasca River Basin in Alberta, Canada (*Leong and Donner* [2015]). The model requires as inputs topography, water surface evaporation, precipitation, surface runoff, and subsurface drainage (water that has drained

through the grid cell's soil column). THMB is typically run at a spatial resolution of $5'$ lat $\times$ $5'$ lon, but the model is scalable, and has been executed at resolutions as high as 220 m $\times$ 220 m (*Motew et al.* [2017]).

THMB characterizes the river flow volume at a cell (i, j) as a dynamic, rectangular box. The length of this box l is given by $l = d \cdot sinu$, where d is the distance between the center of (i, j) and the center of its downstream neighbor (i_{ds}, j_{ds}) and $sinu$ is the sinuosity of the river at (i, j). For the FRB, we assume that at all grid cells, $sinu = 1$. The width w and height h of the river are calculated at each time step by assuming an empirical power relationship with river discharge Q at (i, j). For the FRB, these relationships were determined using WSC records provided by EC from 14 stations and are given by:

$$w = 6.6588 \min\{Q, Q_{bf}\}^{0.4967} \qquad \mathrm{R}^2 = 0.80 \tag{3.1}$$

$$h = 0.2307 \min\{Q, Q_{bf}\}^{0.4123} \qquad \mathrm{R}^2 = 0.71. \tag{3.2}$$

Here, Q_{bf} is the bank-full discharge at (i, j). One of the primary functions of Q_{bf} in our simulations is to estimate the median grain size, D_{50} (see Section 3.2.4, Equation 3.6). For our study, based on performance estimating D_{50}, we set Q_{bf} at each cell as the value of a large event with a 1.75 year return period $Q_{1.75}$, which is computed at each cell using the Pearson Log III method and river discharges from a 20 year THMB simulation with no flooding.

If at any time step $Q > Q_{bf}$, the river flow volume at (i, j) ceases to grow and THMB uses water in excess of Q_{bf} to flood a fraction of the grid cell. The fraction flooded is calculated as the cumulative probability of z_x defined as

$$z_x = \log(W_f/W_{50}), \tag{3.3}$$

where W_f is the floodplain flow volume, W_{50} is 50% of the cell's potential volume and z_x is assumed to follow a normal distribution centered at zero with σ given by the standard deviation of the cell's sub-grid elevation data. Flow velocity through the floodplain is then estimated based on both slope and the wetted perimeter of the floodplain using a Chezy-like formula. Details on the calculations of inundated floodplain area and velocity are provided in *Coe et al.* [2008].

River directions are determined by topography using a digital elevation map (DEM) provided by the United States Geological Survey (USGS) (*Danielson and Gesch* [2011]) (see Section 3.3.2). If the flow path goes through a lake, the lake is filled to its outlet cell's elevation and any excess

water is routed through the lake's outlet. Changes in the potential water surface's volume are stored at the outlet grid cell and distributed throughout the surface water at each time step to determine its elevation relative to the outlet.

3.2.4 Sediment Transport Model

We base our transport routine on the *Patil et al.* [2012] semi-distributed network model that attempts to simulate fluvially-driven sediment transport from individual hillslopes through a watershed (Figure 3.2). The governing equations for sediment transport follow *Patil et al.* [2012] with key differences described below. A summary of the key variables used in the sediment routine is found in Tables 3.1-3.3.

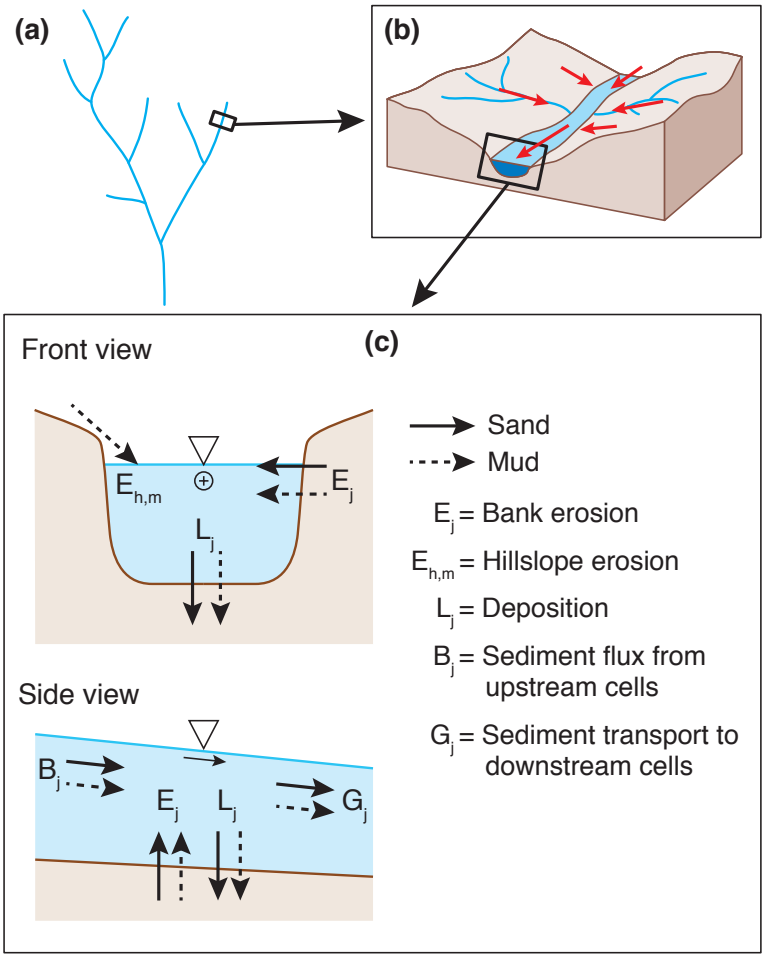

Figure 3.2: Schematic of sediment model at a) watershed scale, b) river reach scale, c) grid cell scale

Table 3.1: General transport variables and parameters

Symbol	Description	Equation/Value	Reference
A	Grid cell area		
A_r	Longitudinal river reservoir area	$A_r = d \cdot 6.6588 \min\{Q, Q_{bf}\}^{0.4967}$	Data from WSC
h	Height of river reservoir	$h = 0.2307 \min\{Q, Q_{bf}\}^{0.4123}$	Data from WSC
h_{bf}	Bank-full height of river reservoir	$h_{bf} = 0.2307 Q_{bf}^{0.4123}$	*Coe* [2000]
V	Volume of river reservoir	$V = A_r h$	
ρ_w	Density of water	$\rho_w = 1000$ kg/m^3	
ρ_s	Density of sediment	$\rho_s = 2650$ kg/m^3	Density of quartz
ρ_b	Bulk density of sediment	$\rho_b = \rho_s(1 - n_p)$	*Patil et al.* [2012]
n_p	Channel porosity	$n_p = 0.1$	
β_t(p)	Characteristic settling time parameter	$\beta_t = 10$	

(p) Indicates a calibrated parameter.

Table 3.2: Sand transport variables and parameters

Symbol	Description	Equation/Value	Reference
$E_{5,i}$	Entrainment rate of D_i at 5% h	$E_{5,i} = \nu_i \cdot \frac{\beta_e(\lambda X_i)^5}{1+\frac{\beta_e}{0.3}(\lambda X_i)^5} \cdot \rho_s A_r$	*Wright and Parker* [2004]
E_i	Channel erosion rate of D_i	$E_i = F_i E_{5,i}$	*Wright and Parker* [2004]
L_i	Deposition rate of D_i	$L_i = \frac{\overline{C_i}}{INT(Z_{Ri})}\nu_i \rho_s A_r$	*Abad et al.* [2008]
B_i	Rate of D_i entering from upstream		
G_i	Transport rate of D_i	$\max\{E_i + B_i - L_i, 0\}$	
X_i	Entrainment parameter	$X_i = S^{0.08}\left(\frac{u_{*sk} \cdot Re_{p_i}^{0.6}}{\nu_i}\right)\left(\frac{D_i}{D_{50}}\right)^{0.2}$	*Wright and Parker* [2004]
$INT(Z_{Ri})$	Approximation of Einstein integral	See *Abad and García* [2006]	*Abad and García* [2006]
Re_{pi}	Dimensionless sediment Reynolds # for D_i	$Re_{p_i} = \sqrt{RgD_i}D_i/\kappa$	
ν_i	Vertical settling velocity of D_i	$\nu_i = gD_i^2R/(18\kappa)$	Stoke's law
u_{*sk}	Shear velocity due to skin friction	See *Wright and Parker* [2004]	*Wright and Parker* [2004]
τ_{*bf}	Bank-full channel Shields stress	gravel: 0.049, sand: 1.86	*Parker* [2008]
$\overline{C_i}$	Depth-averaged concentration of ith class	$\overline{C_i} = \left(\frac{E_i + B_i}{\rho_s V}\right)(\beta_t 0.05h/\nu_i)$	*Patil et al.* [2012]
F_i	Fraction of bed in ith class	[vf, f, m] = [0.003, 0.01, 0.1]	Data from WSC
β_e	Wright-Parker constant	$\beta_e = 7.8 \times 10^{-7}$	*Wright and Parker* [2004]
λ	Mixture suppression parameter	$\lambda = (1 - 0.28\sigma_\phi)$	*Wright and Parker* [2004]
σ_ϕ (p)	std on sedimentological scale	sand: 0.6, gravel: 2.6	
D_i	ith grain class representative	[vf, f, m] = [0.0088, 0.18, 0.35] mm	
D_{50}	Mean grain size in a given cell	$D_{50} = \frac{h_{bf} S \rho_w}{\tau_{*bf}(\rho_s - \rho_w)}$	*Parker* [2008]

(p) Indicates a calibrated parameter.

Table 3.3: Mud transport variables and parameters

Symbol	Description	Equation/Value	Reference
$E_{h,m}$	Hillslope erosion rate of mud	$E_{h,m} = \max\{\beta_h F_m(\tau_h - \tau_{hc})A, 0\}$	*Patil et al.* [2012]
E_m	Channel erosion rate of mud	$E_m = \max\{e_0 \cdot (\frac{\tau_b}{\tau_c} - 1)A_r, 0\}$	*Patil et al.* [2012]
L_m	Deposition rate of mud	$L_m = \max\{(1 - \frac{\tau_b}{\tau_c})\nu_m C_m A_r, 0\}$	*Patil et al.* [2012]
B_m	Rate of mud entering from upstream		
G_m	Transport rate of mud	$G_m = \max\{E_m + B_m - L_m, 0\}$	
τ_h	Hillslope shear stress	See *Patil et al.* [2012]	
τ_b	Channel shear stress	See *Patil et al.* [2012]	
$\tau_{hc}(p)$	Critical hillslope shear stress	$\tau_{hc} = 0.1$ N/m^2	
τ_c	Critical channel shear stress	$\tau_c = k_\tau(\rho_b - \rho_w)^{0.73}$	*Mitchener and Torfs* [1996]
F_m	Fraction of hillslope soil in mud class	From ISRIC data	*Pelletier* [2012]
C_m	Depth-averaged concentration of mud in channel	$C_m = \frac{E_m}{V}(\beta_t h/\nu_{m(t-1)})$	
ν_m	Settling velocity of mud	See *Patil et al.* [2012]	*Hwang* [1989]
Hy	Hysteresis parameter		
β_r(p)	Rising limb threshold coefficient for hysteresis	$\beta_r = 2.4$	
β_f(p)	Falling limb threshold coefficient for hysteresis	$\beta_f = 0.4$	
κ_τ(p)	Critical channel shear stress parameter	Hy = 0: 0.003, Hy = 1: 0.006	*Mitchener and Torfs* [1996]
e_0	Erosion coefficient rate	$e_0 = 2.0 \times 10^{-4}$ kg/m^2/s	*Patil et al.* [2012]
β_h(p)	Hillslope proportionality constant	$\beta_h = 1.8 \times 10^{-6}$ s/m	*Patil et al.* [2012]

(p) Indicates a calibrated parameter.

Patil et al. [2012] assumed a uniform bed grain size of 0.35 mm. The variability of grains within the river beds of the FRB make this assumption inappropriate for our study. In our model, we remove the assumption of a uniform grain size and transport three classes of sand grains, $0.0625 - 0.125$ mm, $0.125 - 0.25$ mm, and $0.25 - 0.5$ mm each represented by their geometric means. For each class, the entrainment at 5% of river depth $E_{5,i}$ at a given time step and grid cell comes from an empirical formula developed in *García and Parker* [1991] and refined in *Wright and Parker* [2004].

In *Patil et al.* [2012], the sand entrainment rate is for uniform grains and comes from Equation (38) of *García and Parker* [1991]. We instead use the non-uniform entrainment rate given in *Wright and Parker* [2004]. For each grain size class i, we have:

$$E_{5,i} = \nu_i \cdot \frac{\beta_e(\lambda X_i)^5}{1 + \frac{\beta_e}{0.3}(\lambda X_i)^5} \cdot \rho_s A_r, \tag{3.4}$$

where ν_i is the settling velocity of the *ith* class representative D_i, $\beta_e = 7.8 \times 10^{-7}$, $\lambda = (1 - 0.28\sigma_\phi)$ and σ_ϕ is the standard deviation of the bed distribution on the sedimentological scale, and X_i is the entrainment parameter defined in *Wright and Parker* [2004]:

$$X_i = S^{0.08}\big(\frac{u_{*sk} \cdot Re_{p_i}^{0.6}}{\nu_i}\big)\big(\frac{D_i}{D_{50}}\big)^{0.2}. \tag{3.5}$$

Here, S is the river slope, u_{*sk} is the shear velocity due to skin friction (computed as in *Wright and Parker* [2004]), Re_{p_i} is the dimensionless sediment Reynolds number of D_i defined using kinematic viscosity $\kappa = 1.307 \times 10^{-6}$ m^2/s, and D_{50} is the median grain size. For our study, σ_ϕ takes on one calibrated, fixed value for all cells identified as sand-bed $\sigma_{\phi s}$, and a second calibrated, fixed value for all cells identified as gravel-bed $\sigma_{\phi g}$. To estimate D_{50}, we use a competency calculation based on the bank-full Shields number τ_{*bf} expressed as

$$\tau_{*bf} = \frac{h_{bf} \cdot S \cdot \rho_w}{D_{50}(\rho_s - \rho_w)}, \tag{3.6}$$

where h_{bf} is the bank-full height (provided by the hydraulic geometry of THMB). We solve Equation (3.6) for D_{50} and complete the calculation using the approximation

$$\tau_{*bf} = \begin{cases} 0.049 & \text{if gravel-bed} \\ 1.86 & \text{if sand-bed} \end{cases} \tag{3.7}$$

given in *Parker* [2008].

Though observed grain size distributions are limited in the FRB, *McLean* [1990] reported a median grain size of 0.34 mm at Mission (sand-bed) and 12 mm at the Yaalstrick Bar (gravel-bed) roughly 10 km upstream of Mission, and *McLean et al.* [1999] reported median surface grain sizes of 42 mm at Agassiz (gravel-bed) and 100 mm at Hope (gravel-bed). At these locations, our model estimates D_{50} as 0.71 mm, 18 mm, 77 mm, and 130 mm, respectively. These results appear to indicate that our method of approximating D_{50} may be biased towards overestimation, but produces reasonable results at least near the basin's outlet.

From the entrainment rate, we compute the rate of sand of class i entering suspension from erosion as $E_i = F_i E_{5,i}$, where F_i is the fraction of bed composed of grains within the *ith* class. For sand-bed streams, we assume a normal distribution and use D_{50} and σ_ϕ to compute F_i. For gravel-bed streams, which typically have a bi-modal distribution, we set F_i to 0.003 for very fine sand, 0.01 for fine sand, and 0.1 for medium sand. These values were chosen so that percent finer distributions of simulated sand loads roughly match WSC observations from EC (see Section 3.3.2).

Sand Deposition

For the *ith* grain class, we use the deposition rate L_i used in *Patil et al.* [2012], which originated from *Abad et al.* [2008], but with physical variables computed specifically for the representative diameter D_i:

$$L_i = \frac{\overline{C_i}}{INT(Z_{Ri})} \nu_i \rho_s A_r, \tag{3.8}$$

where $INT(Z_{Ri})$ is an approximation of the suspended sediment concentration profile used in *Patil et al.* [2012] and presented in *Abad and García* [2006] and $\overline{C_i}$ is the depth-averaged volumetric concentration of the *ith* class. In our work, we compute $\overline{C_i}$ as:

$$\overline{C_i} = \left(\frac{E_i + B_i}{\rho_s V} \right) \left(\beta_t 0.05 h / \nu_i \right). \tag{3.9}$$

Here, B_i is the rate (kg/s) of suspended sand of class i entering the cell from upstream cells, V is the water volume within the cell's river flow volume, and β_t is a dimensionless, calibrated parameter. The transport rate G_i is then given by $G_i = \max\{E_i + B_i - L_i, 0\}$.

Mud Erosion

Like *Patil et al.* [2012], we assume that only mud originally generated from hillslope erosion can be eroded in the river channel and the rate of hillslope erosion $E_{h,m}$ is proportional to the amount of hillslope shear stress τ_h over some critical value τ_{hc}. However, following *Pelletier* [2012], we additionally assume $E_{h,m}$ within a cell is proportional to the fraction of soil texture within the clay or silt class (< 0.0625 mm) F_m:

$$E_{h,m} = \max\{\beta_h F_m(\tau_h - \tau_{hc})A, 0\}. \tag{3.10}$$

Here, β_h is the proportionality constant with units s/m. As in *Patil et al.* [2012], τ_{hc} and β_h take single, fixed values obtained through calibration.

As in *Patil et al.* [2012], the mud supply can be eroded from the river at a rate determined by the channel shear stress τ_b and a critical shear stress threshold τ_c:

$$E_m = \max\{e_0 \cdot (\frac{\tau_b}{\tau_c} - 1)A_r, 0\}, \tag{3.11}$$

where $e_0 = 2.0\times10^{-4}$ kg/m^2/s. To compute τ_c, like *Patil et al.* [2012] , we use the formula suggested by *Mitchener and Torfs* [1996]: $\tau_c = k_\tau(\rho_b - \rho_w)^{0.73}$. Here, k_τ is a dimensionless coefficient and ρ_b is the bulk density of the sediment and is dependent on channel porosity n_p as $\rho_b = \rho_s(1 - n_p)$. For beds composed overwhelmingly of mud, it is typical for $k_\tau = 0.015$. This was the value of k_τ used by *Patil et al.* [2012]. However, *Mitchener and Torfs* [1996] noted that the erosion rate of mud decreases with increasing sand content. Based on observed data, we conceptualize the river beds of the FRB as having significant sand content in this regard throughout the year and particularly high sand content during periods of high flow where the mud supply is exhausted. We therefore allow k_τ to take on two potential values:

$$k_\tau = \begin{cases} k_{\tau_L} & \text{if} \quad Hy = 0 \\ k_{\tau_H} & \text{if} \quad Hy = 1. \end{cases} \tag{3.12}$$

In (3.12), $k_{\tau_H} > k_{\tau_L}$ and Hy is a binary variable (which we call the hysteresis parameter) that takes the value 1 during the period when the rising/falling of sediment load rates appears to be disconnected from the rising/falling of water flux rates, and the value 0 when the two rates rise/fall in concert. For our study, k_{τ_H} and k_{τ_L} are single, fixed calibrated values and in a given year y, Hy is set to 1 the first time Q exceeds $\beta_r\overline{Q_y}$ and returned to 0 the first time Q falls below $\beta_f\overline{Q_y}$. Here, $\overline{Q_y}$ is the average discharge for year

y and the threshold coefficients β_r and β_f are calibrated. In *Patil et al.* [2012], the value of n_p was calibrated between 0.1-0.5; however, because we calibrate k_τ, it is unnecessary to calibrate n_p and we instead set it to a fixed value $n_p = 0.1$. While this decision does not affect the results of the process of tuning the model, it will impact the values of k_τ; if we had instead set $n_p = 0.5$, values of k_τ would be roughly three times larger.

Mud Deposition

We compute the rate of mud deposition as in *Patil et al.* [2012]:

$$L_m = \max\{(1 - \frac{\tau_b}{\tau_c})\nu_m C_m A_r, 0\}. \tag{3.13}$$

In (3.13), C_m is the mass concentration of mud (kg/m^3) and ν_m is the settling velocity of mud. To compute C_m at a given time step t, we use:

$$C_m = \frac{E_m}{V}(\beta_t h/\nu_{m(t-1)}). \tag{3.14}$$

Here, $\nu_{m(t-1)}$ is the value of ν_m at the grid cell in the previous time step and is initialized at 1×10^{-4} m/s. The transport rate of mud G_m is given by $G_m = \max\{E_m + B_m - L_m, 0\}$, where B_m is the rate (kg/s) of suspended mud entering the cell from upstream cells.

Transport in Lakes and Floodplains

We assume that lake cells can only transport or deposit suspended sediment (lakes are not allowed to eroded sediment into suspension). In these cells, transport is computed as $G_i = \max\{B_i - L_i, 0\}$ and $G_m = \max\{B_m - L_m, 0\}$, where the governing equations of the transport rates are the same as those for sand and mud within the river, but the geometry used is that of the lake. In floodplains, we assume sediment is mainly supplied by the river when bank-full discharge is exceeded and that the river is only capable of supplying mud since suspended sand concentration at or above bank-full discharge is expected to be essentially zero. These two assumptions allow us to simplify floodplain computations to only consider the dynamics of mud. Mud exchange between the river and floodplain is determined by mud concentration and the water flux between the flow volumes. Flow height and velocity through the floodplain are estimated as outlined in Section 3.2.3 and detailed in *Coe et al.* [2008]. The governing equations for mud transport and concentration through the floodplain are the same as those through the river reservoir, but use the geometry and flow properties of the floodplain.

3.2.5 Metrics for Analysis

We compare our model's simulations of sediment load to observed values using the R^2, NSE, and percent bias (PBIAS) metrics. The coefficient of determination, R^2 is a commonly used metric that measures the percent of the model variance that is explained by the variance of observations. By its construction, it emphasizes a model's ability to mimic high extreme events and is insensitive to proportional and additive differences between observations and simulations (*Legates and McCabe* [1999]). The NSE measures a model's ability to predict observations relative to the predictive ability of the mean observation. It is defined as

$$\text{NSE} = 1 - \frac{\sum_{t=1}^{n}(sim(t) - obs(t))^2}{\sum_{t=1}^{n}(\overline{obs} - obs(t))^2}, \tag{3.15}$$

where $sim(t)$ and $obs(t)$ are the simulated and observed values at time step t, respectively, and $\overline{obs}$ is the mean of the n observations. The NSE is sensitive to high extreme values, but unlike R^2, it is also sensitive to differences in simulated and observed means and variances (*Legates and McCabe* [1999]). Both R^2 and NSE are measures of the magnitude of error between simulations and observations and neither accounts for a model's potential bias to overestimate or underestimate observed values; the PBIAS statistic, defined as

$$\text{PBIAS} = \frac{\sum_{t=1}^{n}(sim(t) - obs(t))}{\sum_{i=1}^{n} obs(t)}, \tag{3.16}$$

measures this tendency. A positive PBIAS value indicates a tendency to over-predict while a negative value indicates a tendency to under-predict. The degree of this bias is given by the magnitude of the PBIAS. The NSE and PBIAS metrics were given qualitative ranges for water flux and sediment load in *Moriasi et al.* [2007] (Table 3.4).

3.3 Study Site and Input Data

3.3.1 Study Site

At 230,000 km^2 in drainage area, the FRB is the largest watershed in British Columbia, Canada (B.C.). It is both recreationally and economically important to the province of B.C. The river system provides habitat for over 100 species of fish including all five species of pacific salmon. Over 75% of the basin is forested (*Schnorbus et al.* [2010]) and accounts for a large percentage of the trees used in B.C.'s harvesting industry. Overall, 80% of

Table 3.4: Qualitative ranges for NSE and PBIAS metrics. "VG", "G", "S", and "US" are "very good", "good", "satisfactory", and "unsatisfactory, respectively. Table is taken from *Moriasi et al.* [2007]

		PBIAS	
	NSE	Streamflow	Sediment
VG	$0.75 < \text{NSE} \leq 1.00$	$\text{PBIAS} < \pm 10$	$\text{PBIAS} < \pm 15$
G	$0.65 < \text{NSE} \leq 0.75$	$\pm 10 \leq \text{PBIAS} < \pm 15$	$\pm 15 < \text{PBIAS} \leq 30$
S	$0.50 < \text{NSE} \leq 0.65$	$\pm 15 < \text{PBIAS} \leq \pm 25$	$\pm 30 < \text{PBIAS} \leq 55$
US	$\text{NSE} \leq 0.50$	$\text{PBIAS} \geq \pm 25$	$\text{PBIAS} \geq \pm 55$

the provincial gross domestic product and 10% of the federal GDP comes from within the FRB (*Canadian Heritage Rivers Systems* [2015]). More than 60% of the B.C. population resides within the FRB, with many people living on floodplains.

Hydrology and Climatology

The FRB runs 1,400 km from headwaters in the Rocky Mountains to its outlet into the Pacific Ocean at Vancouver. Hydro-climatically, the basin is often divided into three regions: i) an eastern mountain portion (Rocky Mountains), ii) an interior plateau, and iii) a coastal mountain portion. The mountainous eastern portion has the highest elevations and is characterized by steep valleys shaped by glaciers. Average annual runoff and precipitation are highest in the coastal mountains and lowest in the interior plateau (Figure 3.3). Runoff in the Rocky and coastal mountains is snowmelt driven while the interior plateau contains hybrid and rain dominated regimes. Peaks in both runoff and sediment flux tend to occur in late spring or early summer with sediment peaks occurring first and showing some hysteresis relative to water flux.

Sediment Sources

Slaymaker [1977] identified five main sources of sediment and solute in temperate alpine environments such as those found within the mountainous regions of the FRB: 1) atmosphere, 2) biosphere, 3) surface erosion, 4) subsurface erosion, and 5) bank erosion. Of these sources, the author concluded surface and subsurface erosion are the dominant mechanisms of sediment yield in such environments. Subsequent studies (*Jordan* [1991]; *Slaymaker*

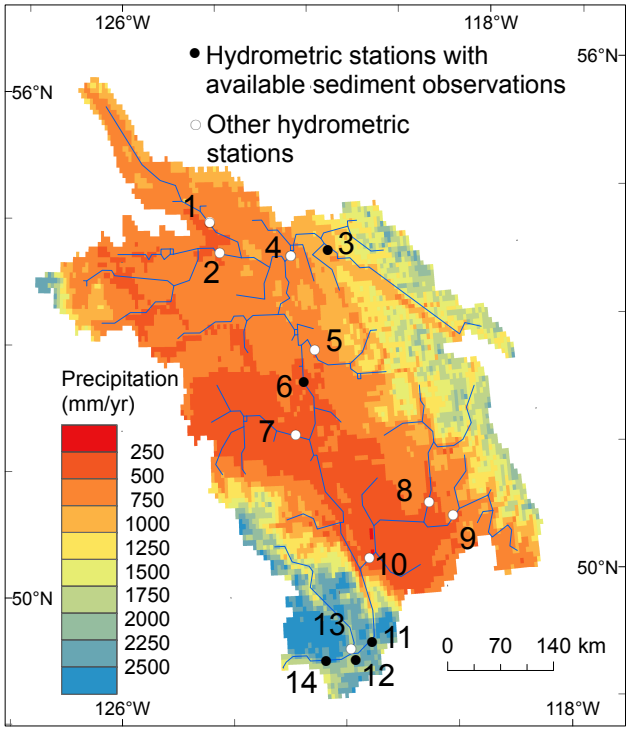

Figure 3.3: Average annual precipitation across the FRB during 1965-2004.

[1993]) of the Lillooet basin within the coastal mountains have used lake sedimentation rates and the sediment budget concept to conclude that primary denudation alone does not account for the sediment yield out of the basin and show the importance of the FRB's glacial history in its sediment yield. Indeed, significant glaciation occurred throughout the FRB during the Pleistocene Epoch leaving behind thick glacio-lacustrine, glacio-fluvial, and glacial deposits along the main valleys (*McLean et al.* [1999]). These sediments were then incised post-glacially by the Fraser River and its main tributaries and act as the primary supply source for these channels directly through bank or terrace erosion (*Church* [1990]).

Because of the Quaternary sediments left from glaciation, the specific sediment yield (yield per basin area) of British Columbia basins does not scale with basin area as conventional wisdom predicts (*Church et al.* [1989]; *Church and Slaymaker* [1989]). While specific sediment yield is typically expected to decrease with basin area as sediment sinks such as lakes and hillslope bottoms act to disconnect sediment sources from the basin's out-

let, the remobilization of glacial sediment in the coastal mountains causes positive allometry within its basins. Heterogeneity prevents extrapolation of this allometry to the entire FRB; while specific sediment yield decreases with basin size in the coastal mountains, *Schiefer* [1999] and *Schiefer et al.* [2001] found negative allometry within the Nechako Plateau and lowlands of the interior plateau and *Church and Slaymaker* [1989] showed a break in the allometric relationship of B.C.'s specific sediment yield at a basin area of 3×10^4 km^2.

The Fraser River has a well document transition from a gravel to sand dominated bed just before the Mission basin station (*Venditti and Church* [2014]). Accordingly, for the purposes of computing D_{50} using Equation (3.6), our model assumes the bed is gravel-dominated at each grid cell upstream of the Mission station and composed of sand beginning at Mission and continuing downstream.

In our simulation of the FRB, we only explicitly model hillslope erosion due to overland flow. In many watersheds, hillslope erosion rates can be dominated by factors including earthquakes and landslides or mass wasting (*Parker et al.* [2011]; *Pearce and Watson* [1986]), fires (*Warrick and Rubin* [2007]; *Warrick et al.* [2012]), and land use and urbanization (*Manh et al.* [2015]; *Yang et al.* [2015]; *Warrick et al.* [2013]; *Warrick et al.* [2015]). While in reality a number of these factors may influence the sediment dynamics of the FRB, we view accounting for them as being outside the scope of our study. There has been a historical lack of earthquakes affecting the FRB, anthropogenic influence is minimal upstream of Mission, and using data from *Canadian Forest Service* [2016], we estimate that an average of only 23,000 ha of the FRB (0.1% of the basin's total area) is affected by wildfire. Though landslides and mass wasting do occur within the basin and may affect small order streams, the sediment they generate is typically disconnected from the main channel network and we expect sediment transport along the main stem to see minimal effects during our simulation period. The largest mass movement event listed by *Boyer et al.* [2013] from 1965-2004 (the 1975, 13 million cubic meter Devastation Glacier landslide) occurred when sediment load observations were available and both the year and five year period after the landslide showed below average annual sediment yield at the Mission station downstream of the event's location.

Selection Rationale

The FRB was chosen to test our adapted model for three main reasons. First, historical sediment load and river discharge data are available from

the WSC for several stations across the basin (Table 2.1). Second, the diverse landscape, ecology, and climate represent the heterogeneity common in large basins. Third, the basin experiences relatively low anthropogenic disturbance upstream of Mission, with agricultural and urban influences either limited in scale or confined to the basin's delta, less than 5% of B.C.'s population residing upstream of Mission, and only two small hydroelectric dams in the Nechako (25,000 km^2 drainage area) and Bridge-Seton (4,700 km^2 drainage area) sub-basins. The decrease in discharge at the Fraser River outlet due to the Nechako reservoir has been calculated to range from 1 to 6 percent the annual mean flow (*Moore* [1991]). Furthermore, it is located in the interior plateau where sediment generation is already expected to be at a minimum.

3.3.2 Input Data

From 1965-1986 the WSC collected sediment load data at six gauges along the main stem of the Fraser River (one gauge, located at Port Mann downstream of Mission, is not included in this study because it is within an estuary). The WSC's reported suspended loads at a gauge were typically based on 150-220 manually collected samples at single vertical sections. During the freshet period, where the majority of suspended load is transported, daily samples were taken, while measurements were infrequent from October-March when only a small amount of the basin's suspended load is moved. To properly depth-integrate the single vertical observations, a correction factor K was computed as the ratio of the mean concentration computed with five vertical observations c_5 and the mean concentration computed with a single vertical observation c_1. To compute c_5, WSC took load samples at five vertical sections 10-15 times a year. Daily sediment loads g_i were computed as $g_i = KQ_iC_i$ where Q_i is the daily mean water flux and C_i is the daily mean sediment concentration. For more details on the sampling and correction process, see *McLean et al.* [1999]. We use observed sediment data from five stations (indicated by a * in Table 2.1). The locations of these stations, as well as those of the river discharge gauges are displayed in Figure 2.1.

To tune river discharge, we use observations of water flux provided by WSC at 14 stations during the time period that corresponds to that of sediment concentration measurements (1965-1986) and at 13 stations over the remaining period of the simulation (from 1987-2004, river discharge data are unavailable at Agassiz) (Figure 2.1). Five of the 14 stations during the first period and four of the 13 stations during the second period correspond to locations of sediment concentration measurement. Because the Nechako

reservoir delays and reduces flow out of the Nechako basin, simulations are compared against naturalized flow at Nechako, Hope, and Mission (PCIC). Naturalized flow was not available from PCIC for Marguerite and Agassiz. These stations will be affected by the reservoir, but the impact is relatively small as the water flux diverted from Nechako is roughly 6.5% and 3.5% of the river discharge at Marguerite and Agassiz, respectively.

River elevation, river direction, and slopes at $1/16^\circ \times 1/16^\circ$ resolution across the basin were derived from USGS's 15 arc-second Global Multi-resolution Terrain Elevation Data map (*Danielson and Gesch* [2011]). River direction and river slope are computed using the automated process and manual corrections described in Chapter 2. The hillslope value of a given $1/16^\circ \times 1/16^\circ$ cell is calculated as the difference between the maximum and minimum values of the 15 arc-second data within that cell divided by the cell length in the direction normal to flow as determined by the river direction map.

Lakes are simulated by THMB prior to the sediment run using outlet locations determined by a georectified, rasterized lake map provided by the British Columbia Geological Survey (BCGS). Texture data is provided by the International Soil Reference and Information Centre (ISRIC). River height and width relations are calibrated using WSC data.

Stationary Inputs

By running the model as tuned for the 1965-1986 period over the 1965-2004 time period, we implicitly assume several variables and relationships remain stationary throughout the time of simulation; these include the hydrometric relationships that determine river width and height, the hysteresis parameters that dictate critical channel shear stress, and bank-full height. We also assume that the mechanism for hillslope erosion and sediment will continue to be overland flow. While it is possible that a combination of changes to land use, vegetation, dominate hillslope detachment mechanisms, and potential mass wasting events such as a large-scale fire or landslides may violate these assumptions, we view these possibilities as outside of the scope of our study. The largest landslide in the basin listed by *Boyer et al.* [2013] during the 1987-2004 was the Hummingbird Creek event in 1997 that generated 76,000 m^3, or roughly 0.2 Mt, of sediment (*Pearce and Watson* [1986]). By contrast, the average annual observed sediment load at Hansard is 3.7 Mt. The average area annually affected by wildfires is roughly 0.1% of the basin area and according to data from *Canadian Forest Service* [2016], the average area annually affected by wildfires during the 1987-2004 period (11,500 ha)

was roughly the same as the area during 1965-1986 (12,300 ha).

Perhaps the biggest change to land use and vegetation in the region during the 1987-2004 period relates to the mountain pine beetle (MPB) outbreak that began in the early 1990's and persisted through the remainder of the simulation period. During the outbreak, the MPB infested and killed trees within the FRB and may have affected sediment dynamics directly by generating more hillslope erosion through detachment by rainfall or indirectly by changing the flow regime within the basin. *Schnorbus et al.* [2010] concluded that flow regimes in alpine and sub-alpine regions, where most of the sediment within the FRB is generated, have low sensitivity to these forest disturbances. Therefore flow regime changes caused by the MPB are only likely to influence sediment dynamics in infested regions disconnected from the coastal and Rocky mountains such as Stuart and Nechako.

We expect the direct influence of the MPB on sediment processes to have been mitigated within the interior plateau by the understorey left after the infestation. This growth was still likely to act as a rainfall intercept (*Schmid et al.* [1991]), reducing the possibility that the infestation caused rainfall detachment within the interior plateau to become significant relative to generation by overland flow in the mountainous regions. After the infestation, there was an increase in clear-cutting in the FRB as a means of salvage harvesting which would have removed any understorey and affected the local sediment dynamics. However, the clear-cutting does not appear to be widespread enough to impact the flow regimes of sub-basins (see Section 3.4) from 1987-2004.

Our confidence that the stationarity assumptions we have made are reasonable is bolstered by the understanding that events such as wildfires and landslides appear to have occurred with roughly the same frequency during the period of 1965-1986 as during the period of 1987-2004. In Section 3.4, we will demonstrate that despite our model not accounting for these factors, we are able to reproduce observed sediment yield values from 1965-1986. Furthermore, though sediment observations are not available from 1987-2004, flow data is available during this period. If widespread changes to vegetation, climate, or land use occurred in the FRB from 1987-2004, they would likely manifest as some change to the flow regime, yet we will demonstrate in Section 3.4 that using our stationary assumptions, our model still adequately simulates the water flux throughout the basin.

3.4 Results

Our simulation of the FRB is performed at a 1/16° lat × 1/16° lon spatial scale and 1 hour timescale. To validate the model, we performed a simulation from 1965-1986 during which period sediment observations are available. We then executed the model over the 1965-2004 period to analyze any long-term trends in sediment load.

3.4.1 Historical Comparison (1965-1986)

Metric Performance

The mean coefficient of determination between simulated and recorded values of river discharge and sediment load across all stations were 0.85 and 0.70, respectively during the validation period 1965-1986 (Tables 3.5-3.6). For river discharge, NSE values were "very good" (> 0.75), using the standard outlined in *Moriasi et al.* [2007], for 12 of 14 stations (Table 3.5). The remaining stations, Nechako and Stuart, had "good" (> 0.65) and "satisfactory" (> 0.50) NSE values, respectively. The percent bias (PBIAS) was at least "satisfactory" ($< \pm 25\%$) for all of the stations but Nechako, where naturalized streamflows were used as observations. Eight of the stations had a "very good" PBIAS ($< \pm 10\%$).

Table 3.5: R^2, Nash-Sutcliffe Efficiency, and percent bias in river discharge simulation

	1965-1986			1987-2004		
	R^2	NSE	PBIAS (%)	R^2	NSE	PBIAS (%)
Agassiz	0.90	0.86^{**}	8^{**}	NA	NA	NA
Chilcotin	0.77	0.79^{**}	$17^{\S}$	0.80	0.68^{*}	$27^{\dagger}$
Hansard	0.82	0.77^{**}	$22^{\S}$	0.78	0.74^{*}	5^{**}
Harrison	0.88	0.78^{**}	5^{**}	0.86	0.68^{*}	13^{*}
Hope	0.91	0.88^{**}	-7^{**}	0.89	0.87^{**}	-1^{**}
Marguerite	0.85	0.82^{**}	4^{**}	0.85	0.76^{**}	-9^{**}
Mission	0.98	0.98^{**}	2^{**}	0.99	0.98^{**}	1^{**}
Nechako	0.87	0.71^{*}	$-27^{\dagger}$	0.81	0.66^{*}	$-25^{\dagger}$
North Thompson	0.85	0.82^{**}	$16^{\S}$	0.64	0.79^{**}	6^{**}
Quesnel	0.90	0.86^{**}	$16^{\S}$	0.89	0.87^{**}	8^{**}
Shelley	0.83	0.80^{**}	7^{**}	0.80	0.72^{*}	-1^{**}
South Thompson	0.89	0.89^{**}	-3^{**}	0.91	0.88^{**}	2^{**}
Stuart	0.58	$0.54^{\S}$	14^{*}	0.58	0.56	8^{**}
Thompson	0.92	0.90^{**}	9^{**}	0.88	0.86^{**}	8^{**}

§, *, **, and † indicate satisfactory, good, very good, and unsatisfactory metric values, respectively (as dictated by *Moriasi et al.* [2007]).

Table 3.6: R^2, Nash-Sutcliffe Efficiency, and percent bias in sediment load simulation. Only years where a station had a complete set of observations were used to calculate these metrics.

Station	R^2	NSE	PBIAS (%)	Years[a]	# Years
Agassiz	0.75	0.71^{*}	13^{**}	1967-1986	20
Hansard	0.70	$0.39^{\dagger}$	-18^{*}	1976-1980	5
Hope	0.73	0.72^{*}	8^{**}	1966-1979	14
Marguerite	0.54	$0.53^{\S}$	-11^{**}	1974-1986	13
Mission	0.78	0.77^{**}	-20^{*}	1966-1986	21

[a] "Years" indicate range for which complete set of observations exist.
§, *, **, and † indicate satisfactory, good, very good, and unsatisfactory metric values, respectively (as dictated by *Moriasi et al.* [2007]).

For sediment load simulations, NSE was "very good" (> 0.75) at Mission, "good" (> 0.65) at Hope and Agassiz, "satisfactory" (>0.50) at Marguerite, and "unsatisfactory" (>0.50) only at Hansard, by far the smallest basin. PBIAS was "very good" ($< \pm 15\%$ for sediment loads) at Agassiz, Hope, and Marguerite and "good" ($< \pm 30\%$) at Hansard and Mission (Table 3.6). Figure 3.4 shows scatter plots of observed versus simulated loads at each station for years when the station had a complete set of sediment observations. Generally, the figures show a tendency to underestimate peak loads and over estimate very small loads. Indeed, between 1965-1984, on an annual average, the largest 10% of daily observed flows at Mission corresponded to 40% of the observed annual suspended sediment yield and the largest 50% of observed flows corresponded to 93% of the observed yield. Comparatively, the largest 10% and 50% of simulated daily flows corresponded to 30% and 86% of the simulated suspended sediment yield.

Lake Sedimentation and Yield

While observations of yield from lakes within the FRB are not available from the WSC, several studies have used clastic sediment to estimate the long-term rates of sedimentation at a number of the FRB's lakes. At Lillooet Lake upstream of the Harrison gauging station, *Gilbert* [1970] estimated the sedimentation rate to be 1.8-4.4 Mt/a, *Gallagher et al.* [2004] estimated the sedimentation rate of Kamloops Lake downstream of the confluence of the South and North Thompson Rivers to be roughly 0.7 Mt/a, and *McLean et al.* [1999] found the Harrison River downstream of both Lillooet and Harrison Lake transported an average of 0.12 Mt/a of suspended sediment to

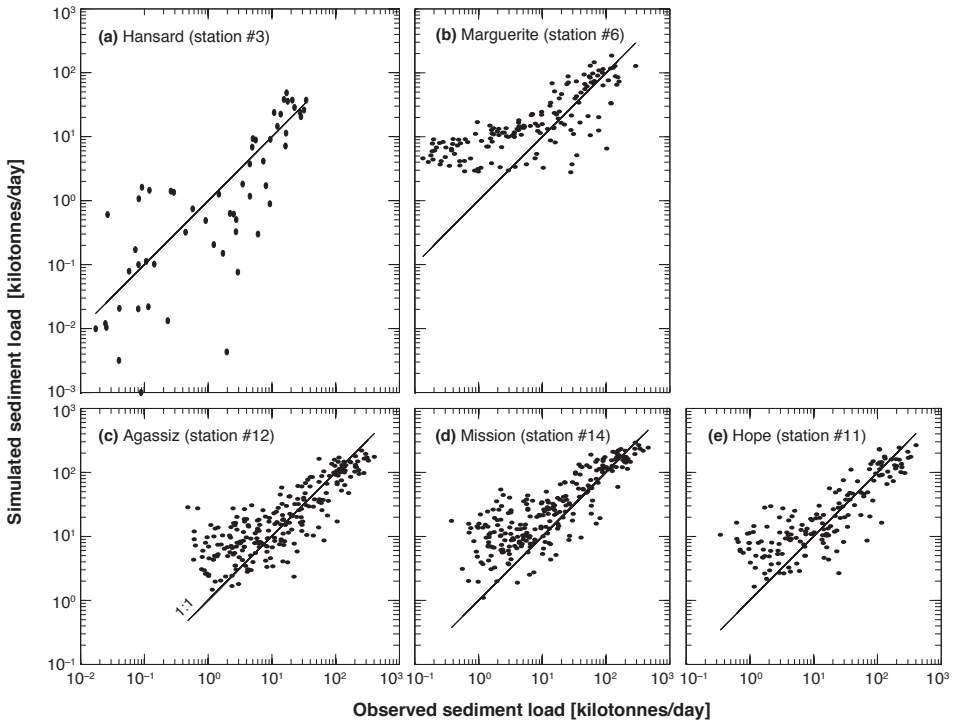

Figure 3.4: Plots of observed versus simulated monthly sediment load (kilotonnes/day) during the historical comparison period (1965-1986) at each station. Graphs are in log-log scale for visual purposes. Corresponding R^2, Nash-Sutcliffe efficiency, and percent bias metrics are presented in Table 3.6.

the main stem of the Fraser River at their confluence just downstream of the Harrison gauging station. We regard Lillooet and Kamloops to be important lakes for characterizing sediment transport because they are upstream of large portions of the coastal and Rocky mountains, respectively and act to disconnect these significant sediment sources from the main stem of the Fraser River. Our model simulates suspended sediment deposition at Lillooet and Kamloops at a rate of 0.9 Mt/a and 1.6 Mt/a, respectively and transport through the Harrison gauging station downstream of Lillooet to be 0.28 Mt/a. While a comparison of simulated suspended sediment deposition rates and previously reported sedimentation rates suggests our model may not precisely predict lake deposition, the two types of estimations are within an order of magnitude and we regard the model's performance in lakes as sufficient for our purposes since sediment transport through lakes

is expected to be small relative to river transport.

3.4.2 Simulated Historical Sediment Dynamics (1965-2004)

In our simulation of the FRB from 1965-2004, over 40% of mud eroded within the basin upstream of Mission originated downstream of Hope. This region is directly connected to the coastal mountains, an area expected to transport relatively large amounts of sediment (Figure 3.5). The interior mountains were also an important mud source, accounting for more than 10% of the total mud eroded. The Thompson sub-basin generated 20% of the total eroded mud within the basin, but Thompson Lake, just downstream of the Thompson station, acts as a sink in the model and prevents nearly any mud from entering the main channel upstream of Hope. This is consistent with common observations of the difference in water quality between the Thompson and Fraser rivers at their confluence (*Reynoldson et al.* [2005]).

Simulated sand load across the basin highlights the expected high values downstream along the primary branch of the Fraser (Figure 3.6). The majority of sand ($\sim$ 90%) was generated along the main stem between Marguerite and Hope where peak flows increase from roughly 4,000 m^3/s to 7,500 m^3/s and the simulated river bed continues to fine. Neither the coastal nor interior mountain regions were significant sand sources, combined they accounted for only 3% of total sand eroded within the river system. One can also see the somewhat localized behavior of sand load consistent with significant deposition rates. This stands in contrast to the connected, propagating behavior of simulated mud, which tends to be supply controlled and have low deposition rates (Figure 3.7). In total, less than 1% of sand generated within the basin reached Mission compared to approximately 10% of all generated mud. Transport of both sand and mud was most widespread from Jul-Sep (Figures 3.5-3.7). In terms of magnitude, mud was generally dominant from August until May at which point simulated supply was exhausted and sand transport began to peak. Throughout this summer period, sand contribution was roughly 30-50%.

Since WSC ended its sediment monitoring program in the FRB in 1986, no long-term estimates of suspended sediment trends have been available for the region. Studies such as *Attard et al.* [2014] have compared sediment loads of individual years to the background levels determined by the 1965-1986 historical record, but have been unable to place their findings in the larger context of long-term trends. For the first time, our study offers some insight into the change in sediment load since the 1980s. In the first 20 years (1965-1984) of simulation, the mean and standard deviation of annual

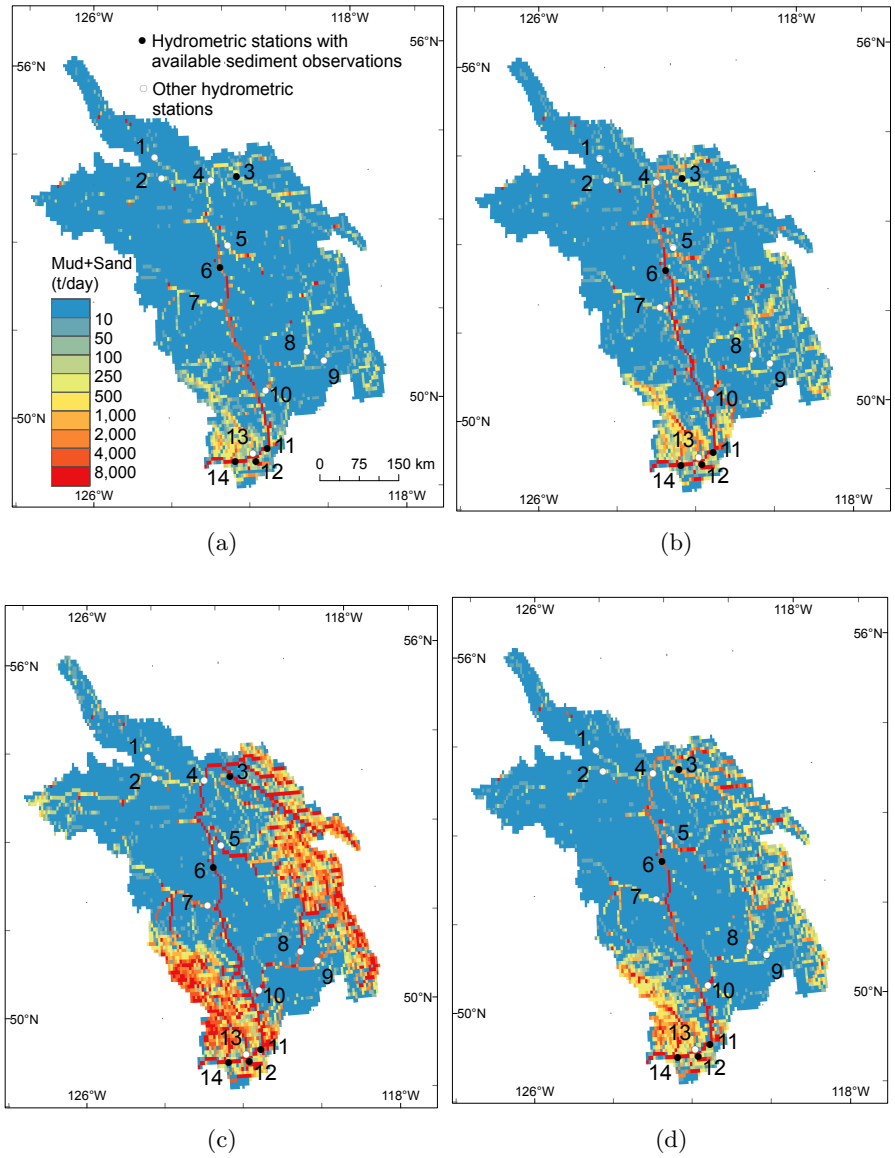

Figure 3.5: 1965-2004 average simulated total (mud+sand) load (tonnes/day) for a) Jan-Mar, b) Apr-Jun, c) Jul-Sep, and d) Oct-Dec.

loads at Mission were 18.2 Mt and 4.7 Mt, respectively. In the last 20 years (1985-2004), the mean and standard deviation were 18.3 Mt and 2.8 Mt. Annual loads at Mission for all but one year from the 1985-2004 period fell

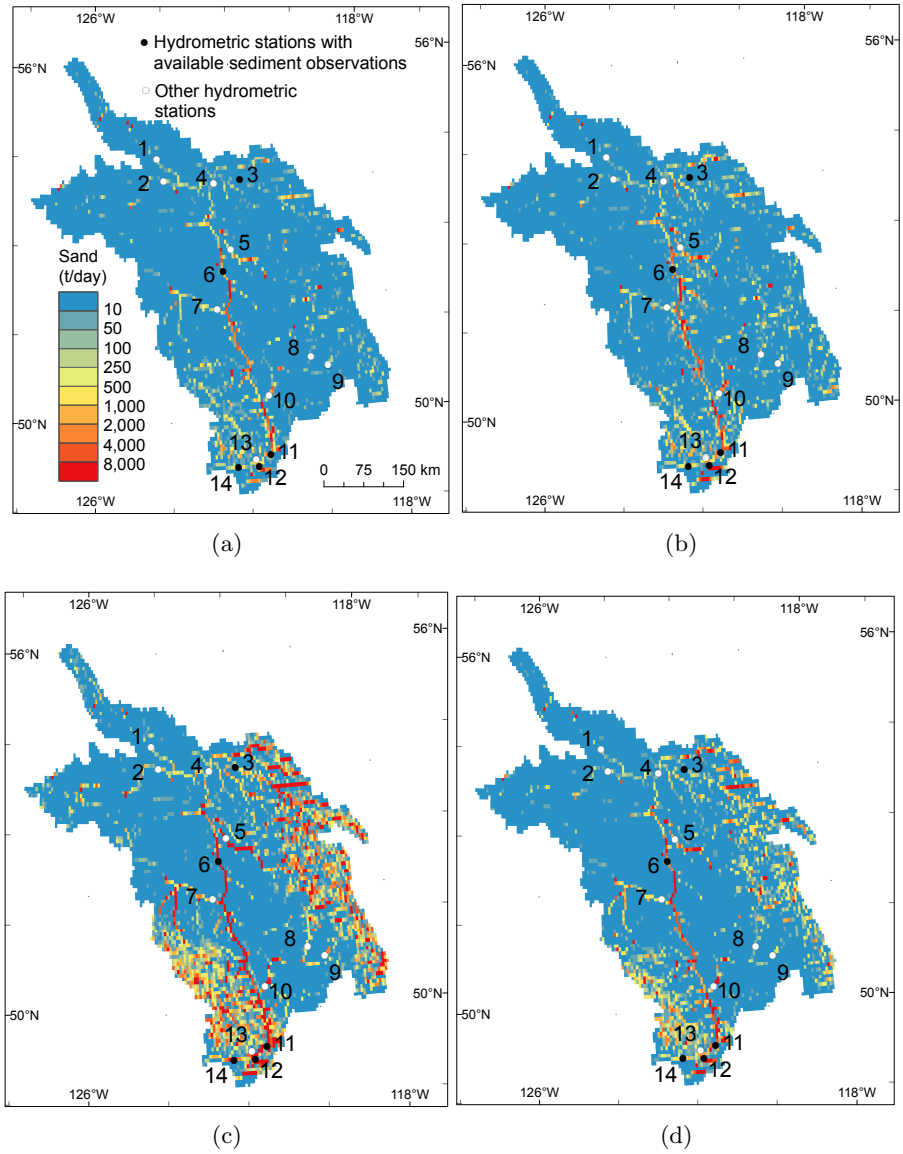

Figure 3.6: 1965-2004 average simulated total sand load (tonnes/day) for a) Jan-Mar, b) Apr-Jun, c) Jul-Sep, and d) Oct-Dec.

within a single 1965-1984 standard deviation of the 1965-1985 mean load. These results do not suggest any trend towards overall larger or smaller sediment transport rates, but do indicate some stabilization in sediment

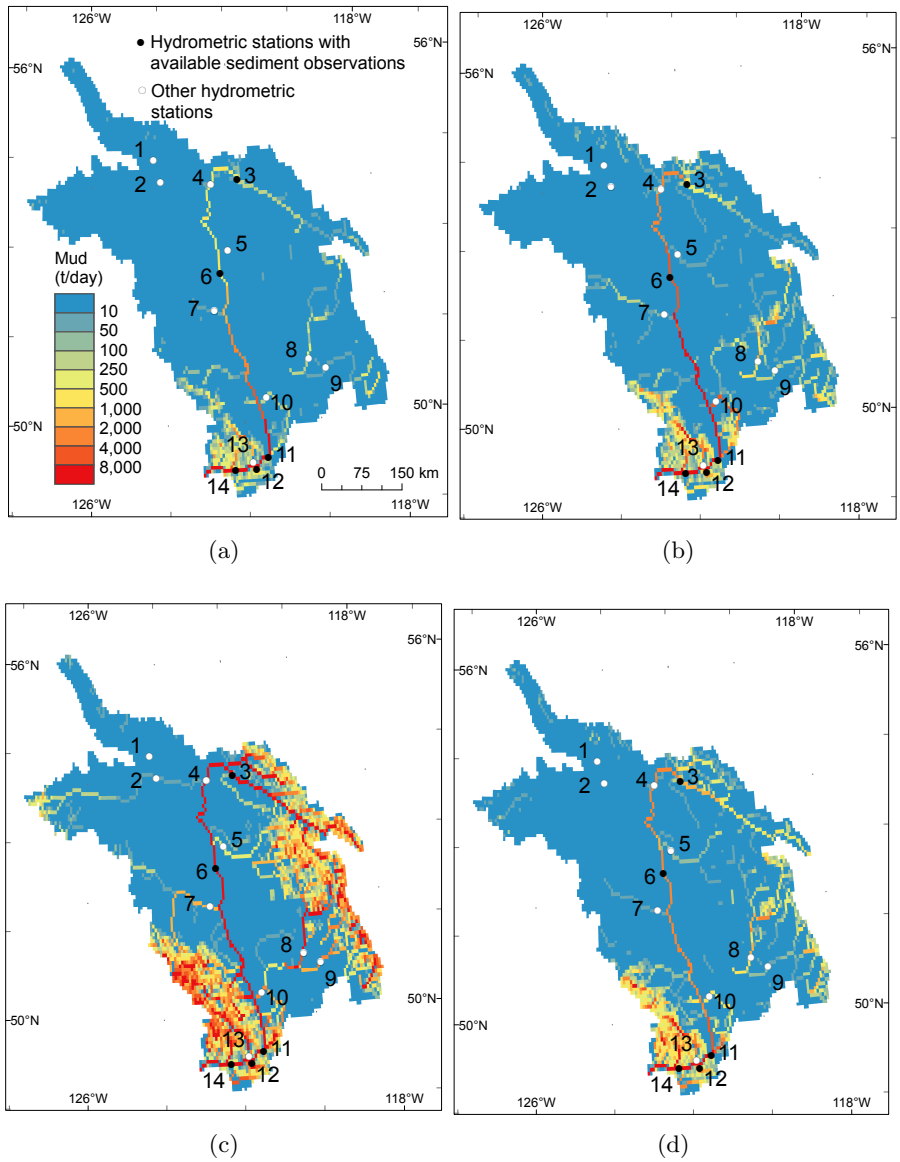

Figure 3.7: 1965-2004 average simulated mud load (tonnes/day) for a) Jan-Mar, b) Apr-Jun, c) Jul-Sep, and d) Oct-Dec.

loads regarding inter-annual variability (Figure 3.8).

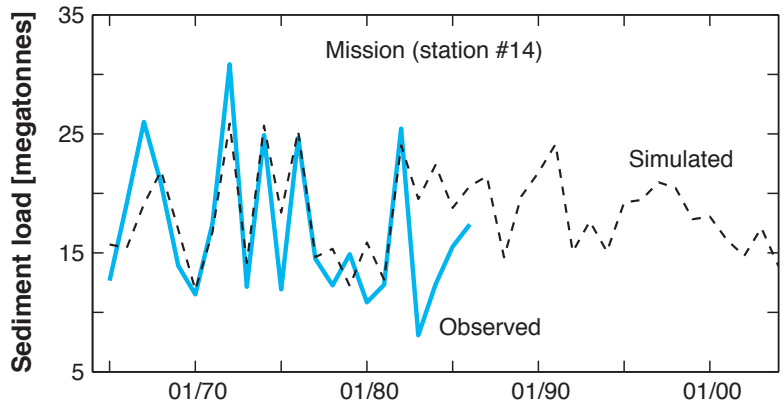

Figure 3.8: Average annual observed sediment load (blue) and simulated total load (black) at Mission in megatonnes.

3.4.3 Parameter Sensitivity

A sensitivity analysis of the calibrated parameters' impact on the fit metrics at each station was performed (Table 3.7). Each parameter was shifted $\pm 10\%$ from its calibrated value and the effects on R^2, NSE, and PBIAS were averaged across all stations. The effects of changes to the standard deviation of the sand-bed grain size distribution σ_{ϕ_s} were restricted to the sand-bed portion of the basin. Similarly, effects due to changes in the gravel-bed standard deviation $\sigma_{\phi g}$ were restricted to the gravel-bed portion of the basin. Correspondingly, sensitivity values of σ_ϕ presented in Table 3.7 represent the averaged effects of changes to σ_{ϕ_s} on simulated loads at Mission (located within the sand-bed portion) and changes to σ_{ϕ_g} on simulated loads at Agassiz, Hope, Marguerite, and Hansard (located within the gravel-bed portion).

The model is most sensitive to values of σ_ϕ. Its impact on the NSE is two orders of magnitude larger than the next most influential parameter and its impact on R^2 and PBIAS is one order of magnitude larger. Using one fixed value of σ_ϕ for all sand-bed cells and a second fixed value for all gravel-bed cells is therefore fairly restrictive. Ideally, σ_ϕ could vary in space and time to more accurately reflect the true distribution of the river bed, but historical records of bed distributions is limited and confined mostly to the delta region of the basin.

The model is least sensitive to critical hillslope shear stress τ_{hc} and κ_{τ_H}, the critical channel shear stress coefficient when Hy = 1. The critical channel

Table 3.7: Sensitivity analysis of parameters on fit metrics. The displayed changes in R^2, NSE, and PBIAS were averaged across all five sediment stations and correspond to a change of ±10% in the calibrated parameter.

Parameter	Value	ΔR^2	ΔNSE	ΔPBIAS(%)
σ_ϕ^a	$(0.6, 2.6)$	0.020	0.306	42.1
β_h	1.8×10^{-6}	0.002	0.009	4.7
β_t	10	0.004	0.004	4.7
β_f	0.4	0.004	0.004	3.6
β_r	2.4	0.007	0.005	4.4
$\kappa_{\tau L}$	0.031	0.006	0.008	4.5
$\kappa_{\tau H}$	0.13	0.003	0.003	0.3
τ_{hc}	0.1	<0.001	0.001	0.6

[a] $\sigma_\phi = (\sigma_{\phi s}, \sigma_{\phi g})$

shear stress coefficient when Hy = 0 κ_{τ_L}, hillslope erosion proportionality constant β_h, hysteresis threshold coefficients β_r and β_f, and characteristic settling time β_t have roughly the same order of magnitude influence over the three fit metrics.

3.5 Discussion

In this chapter, we successfully developed a distributed, mechanistic model capable of matching monthly historical observations throughout a large and diverse basin. Because sediment generation can occur over relatively small spatial scales, both *Smith et al.* [2011] and *Pelletier* [2012] argued that development of such a spatially distributed model was essential. Yet, there exists only one other size-selective, distributed model capable of simulating sediment load across large basins. This model, presented in *Pelletier* [2012], has the benefits of simplicity, low input requirements, and a small number of calibrated parameters, but is also empirical and does not reproduce sub-annual loads. In this sense, we have developed a unique tool in sediment modelling, capable of being used to study the effects of climate or hydrological changes on sub-annual sediment dynamics across a large basin.

Overall, the performance of our model matched historical data well when compared to both suggested metric ranges and other modelling attempts. PBIAS scores at all stations were either "very good" or "good" and only at Hansard, the station with the smallest basin in both area and sediment load, was the NSE metric "unsatisfactory" (Table 3.6). The annual simulation of

128 rivers performed in *Pelletier* [2012] had an $r = 0.79$ correlation score with corresponding historical observations. Though it requires more inputs and parameters, our model's monthly simulations had a correlation of $r = 0.88$ at the gauge nearest the basin's outlet (Mission).

The long-term simulation (1965-2004) of the FRB produced outcomes that are consistent with many of our conceptualizations of sediment dynamics within the basin. Sediment was mainly generated from the mountainous regions in the eastern and coastal portions of the basin (Figure 3.5). Sand transport was mostly confined to the main stem of the Fraser and had a somewhat localized behaviour (Figure 3.6). In comparison, mud load also showed high transport along the Fraser's main stem, but displayed more connectivity than sand load amongst cells (Figure 3.7). Simulation of loads from 1987-2004, a period where no observations are available, provided new insight into the long-term trends of sediment transport within the basin (Figure 3.8). Our analysis showed no trend in the magnitude of the average annual load at Mission, but did indicate its inter-annual variability had reduced since the mid 1980s.

A key limitation to simulating sediment load at large-scales is data on bed distribution. The composition of the river bed can vary highly in time and space. Our sensitivity analysis indicates the model would be highly sensitive to these variations (Table 3.7). However, at present the model only allows for a single value of bed distribution deviation for gravel beds and a single value for sand beds. Observed data could potentially help characterize a more accurate variation.

The lowest agreement between simulations and observations occurs at Hansard and may point to limits of using the model to represent sediment load at smaller scales without higher resolution input data and smaller grid cells. Simulation of peak flow and sediment load is more challenging in such small, upstream basins where model resolution is coarse relative to basin size, and model performance is thus sensitive to input data (e.g. elevation, climate) for individual grid cells. For example, THMB's simulated peak flow at Hansard is 19 days after the observed peak - a discrepancy 8 days larger than at any other station - and this affects the timing of sediment load. There is also a tendency for our model to overestimate loads between $10^{-1} - 10^{1}$ kilotonnes/day (Figure 3.4), a range most of Hansard's monthly sediment loads lie within. This tendency may relate to the timing of loads of this magnitude (fall and winter for Marguerite, Hope, Agassiz, and Mission), or be indicative of a limitation of the model regarding load magnitude at this resolution.

The model developed in this study is capable of producing distributed,

long-term sediment load estimates across a large, complex basin. It can reproduce historical sediment loads, but can also be used to forecast future loads under a given set of assumptions. For instance, the model can be run using hydrological inputs emanating from climate or land use scenarios to study the impact these scenarios may have on sediment loads. Importantly, these studies and other historical studies of sediment load are not restricted to the FRB. The model's governing equations are not specific to our study site, but rather are generic. Thus with proper calibration, our model can and has (*Motew et al.* [2017]) been used to study other North American basins.

Chapter 4

Sediment Simulations Under a Changing Climate

4.1 Introduction

Changes in the temporal and spatial patterns of sediment sources and transport regimes (amount and texture) within a large river basin can have important consequences to humans and biota both within the basin and worldwide. Agricultural soil loss and the global carbon cycle are both closely tied to the processes of sediment erosion, transport, and deposition within river systems (*Walling* [2009]). Locally, water quality, nutrient and contaminant transport, and fish habitat all depend on the movement of fine sediment, as does shoreline retreat/advance in coastal systems (*Syvitski et al.* [2005]). The relationships between sediment yield and the habitat and biota of a basin should be regarded as somewhat sensitive balances; habitat and biota are generally adapted to a range of sediment yield and both reductions and increases in yield outside of that range have the potential for negative repercussions. An attenuated sediment hydrograph corresponds to reduced transport of nutrients to lakes and deltas and shoreline retreat in coastal systems. Increased yield over baseline typically has a negative effect on aquatic biota (*Kerr* [1995]) and water quality (*Whitehead et al.* [2009]). Changes in the variability of peak loads or the timing of the sediment hydrograph, without any associated change in overall annual yield can also have important consequences. Higher variability may lead to an increase in years with peak loads beyond the thresholds of biota and acceptable water quality, and a seasonal amplification of sediment output when gravel-bed spawning fish lay their eggs may lead to river bed clogging and diminish the ability of the fish to reproduce (*Scheurer et al.* [2009]).

Because sediment is closely linked to land cover and hydrology, sediment transport is expected to be sensitive to changes in climate (*Walling* [2009]). Previously, researchers have considered the impacts of a changing climate on sediment yields, particularly in coastal regions; however, very few studies

have investigated the effects on the entire erosion, transportation, and depositional sequence (*Asselman et al.* [2003]), in part because scientists have been limited by a relatively small set of the physically-based, distributed models that are best suited for assessing the consequences of climate change (*Bathurst* [2010]). Further complicating these studies is the ambiguity in isolating observed changes in basin dynamics due to climate change from those caused by land management practices such as logging and dam construction which are typically more influential (*Walling* [2009]).

British Columbia, Canada's Fraser River Basin (FRB) is a research site that is uniquely equipped for sediment-related climate change studies and a location where some of the key issues raised by *Bathurst* [2010] and *Walling* [2009] can be resolved. The FRB is a 230,000 km^2 watershed that has over 20 years of daily observations of water discharge and suspended sediment load available from the Water Survey of Canada (WSC) at several locations across the basin, including near the basin's outlet in the coastal zone. It is also a relatively pristine watershed; there are only two small hydroelectric dams: the Nechako (25,000 km^2 drainage area) and the Bridge-Seton (4,700 km^2 drainage area), and agricultural and urban impacts are either small in scale or confined to downstream of the last gauging station. Because of the low anthropogenic influence within the FRB, it is easier to ascribe any changes in sediment dynamics to effects of climate and hydrological changes rather than land management/use decisions. The impacts of climate change on the hydrology of the FRB has also been extensively modelled by the Pacific Climate Impacts Consortium (PCIC) which has provided climatic and hydrological output from Variable Infiltration Capacity (VIC) simulations performed in *Shrestha et al.* [2012] for three Intergovernmental Panel on Climate Change (IPCC) future scenarios. These simulations make modelling sediment dynamics within the FRB tenable. Finally, we have already developed and calibrated a large-scale mechanistic, distributed sediment transport model on the FRB in Chapter 3. This model is compatible with the synthetic VIC outputs and can be used to simulate basin-wide suspended sediment erosion, deposition, and transportation.

In this chapter, we use the model developed in Chapter 3 to investigate the sensitivity of sediment dynamics within the FRB to potential changes in climate and hydrology using three future climate scenarios. For each scenario, the sediment model is driven by multiple sets of land-surface hydrology inputs provided by VIC simulations presented in *Shrestha et al.* [2012]. Each of these sets of inputs corresponds to a different VIC simulation driven by a specific general circulation model (GCM). We limit our study to impacts of climate changes that are manifested in changes in pre-

cipitation and hydrology as described by *Shrestha et al.* [2012] and do not directly consider changes in land use, vegetation, or the mechanisms controlling hillslope erosion. We analyze the resulting outputs for significant changes in the FRB's sediment yield and timing as well as changes in the spatial distribution of sediment dynamics.

4.2 Methods

4.2.1 Model Overview

The transport model developed in Chapter 3 simulates sediment dynamics by integrating a sediment routine into the Terrestrial Hydrology Model with Biochemistry (THMB) developed in *Coe* [2000]. For each 1/16° latitude × 1/16° longitude grid cell in the FRB, THMB makes hourly calculations of hydraulic geometry and water flux through the river and floodplain reservoirs. The sediment routine then uses these variables as well as landscape data to calculate hillslope erosion of clay and silt class sediment (<0.0625 mm) and channel erosion, deposition, and transportation for mud and three classes of sand grains. THMB requires as inputs groundwater, overland flow, and precipitation. In our study, these inputs come from climate scenario-driven VIC simulations performed in *Shrestha et al.* [2012] (Figure 4.1). Below, we briefly describe the main components of the modelling sequence; details of the model are covered in Chapter 3.

4.2.2 Water and Sediment Routing Model

To simulate water and sediment dynamics through the basin, we use the calibrated model developed in Chapter 3. The transport model integrates an adapted large-scale version of the sediment routine presented in *Patil et al.* [2012] into THMB. THMB conceptualizes each grid cell as having both a river and floodplain reservoir. The river reservoir is characterized as a dynamic, rectangular box whose length is a function of the distance between the grid cell and its downstream neighbor and whose width and depth are related by power functions to the reservoir's water flux. Details on the THMB model are presented in *Coe* [2000] and *Coe et al.* [2008].

The sediment routine uses the calculated water flux and reservoir dimensions in conjunction with landscape characteristics to compute hillslope and river shear stresses and corresponding sediment dynamics through the basin (Figure 3.2). The details of these calculations are provided in Chapter 3 and *Patil et al.* [2012]. Below, we briefly describe the governing equations.

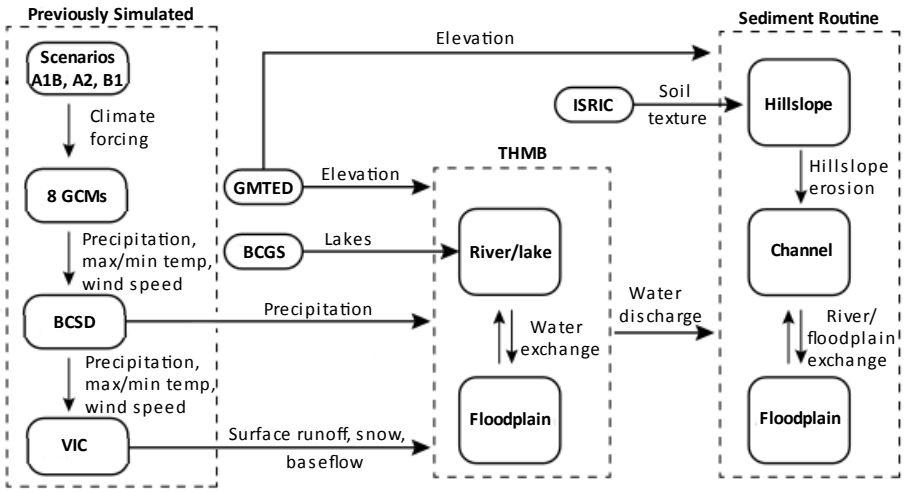

Figure 4.1: Modelling framework. "BCGS" is the British Columbia Geological Survey and "ISRIC" is the International Soil and Reference Centre. All other acronyms have been defined in the text.

Sand Transportation

At each time step and grid cell, we transport three classes of sand grains, 0.0625-0.125 mm, 0.125-0.25 mm, and 0.25-0.5 mm with the classes represented by their geometric means. For each class i, the entrainment at 5% of river depth $E_{5,i}$ is computed as in *Wright and Parker* [2004]:

$$E_{5,i} = \nu_i \cdot \frac{\beta_e (\lambda X_i)^5}{1 + \frac{\beta_e}{0.3}(\lambda X_i)^5} \cdot \rho_s A_r. \tag{4.1}$$

Here, X_i is the entrainment parameter defined in *Wright and Parker* [2004], ν_i is the settling velocity of D_i (the median grain size of class i), $\beta_e = 7.8 \times 10^{-7}$, $\rho_s = 2{,}650$ kg/m^3 is the density of sediment, and $\lambda = (1 - 0.28\sigma_\phi)$ where σ_ϕ is the standard deviation of the bed distribution on the sedimentological scale. The standard deviations of the bed distributions of grid cells in the FRB were calibrated in Chapter 3. From the entrainment rate, the erosion rate E_i follows as $E_i = F_i E_{5,i}$, where F_i is the fraction of bed composed of grains within the *ith* class.

Deposition of the ith class of sand L_i is computed as prescribed by *Abad*

et al. [2008]:

$$L_i = \frac{\overline{C_i}}{INT(Z_{Ri})} \nu_i \rho_s A_r. \tag{4.2}$$

Here $INT(Z_{Ri})$ is the approximation of the suspended sediment concentration presented in *Abad and García* [2006] and $\overline{C_i}$ is the depth-averaged concentration of the *ith* class. The transport rate G_i follows as $G_i = \max\{E_i + B_i - L_i, 0\}$, where B_i is the rate of suspended sand in class i entering the cell from upstream.

Mud Transportation

The model dictates that only mud originally eroded from the hillslope can be moved within the river system. It assumes overland flow is the mechanism for hillslope erosion and that the rate $E_{h,m}$ is a linear function of the fraction of soil within the clay or silt class F_m as well as the hillslope shear stress τ_h over a critical value τ_{hc}:

$$E_{h,m} = \max\{\beta_h F_m (\tau_h - \tau_{hc}) A, 0\}. \tag{4.3}$$

The proportionality constant β_h is calibrated in Chapter 3. Within the river reservoir, mud is eroded from the channel at a rate given by

$$E_m = \max\{e_0 \cdot (\frac{\tau_b}{\tau_c} - 1) A_r, 0\}. \tag{4.4}$$

Here, τ_b is the channel shear stress, τ_c is a critical channel shear stress computed as in *Mitchener and Torfs* [1996], and $e_0 = 2.0 \times 10^{-4}$ kg/m^2/s.

The model computes mud deposition as

$$L_m = \max\{(1 - \frac{\tau_b}{\tau_c}) \nu_m C_m A_r, 0\}, \tag{4.5}$$

where C_m is the mass concentration of mud (kg/m^3) and ν_m is its settling velocity. The transport rate G_m then follows as $G_m = \max\{E_m + B_m - L_m, 0\}$, where B_m is the rate (kg/s) of mud entering from upstream.

4.2.3 Analysis of Simulations

Simulations were performed at a 1/16° lat × 1/16° lon spatial scale and hourly timescale. Prior to simulating future water flux and sediment processes, we considered the ability of the transport model and synthetic VIC inputs to match the seasonality of historical records for the period 1965-1994

using NSE and PBIAS metrics. The NSE measures a model's ability to predict observations relative to the predictive ability of the mean observation. It is defined as

$$\text{NSE} = 1 - \frac{\sum_{t=1}^{n}(sim(t) - obs(t))^2}{\sum_{t=1}^{n}(\overline{obs} - obs(t))^2}, \tag{4.6}$$

where $sim(t)$ and $obs(t)$ are the simulated and observed values at time step t, respectively, and $\overline{obs}$ is the mean of the n observations. The PBIAS statistic measures the relative tendency for the model to overestimate or underestimate observed values, it is defined as

$$\text{PBIAS} = \frac{\sum_{t=1}^{n}(sim(t) - obs(t))}{\sum_{i=1}^{n} obs(t)}. \tag{4.7}$$

A positive PBIAS value indicates a tendency to over-predict while a negative value indicates a tendency to under-predict. The degree of this tendency is given by the magnitude of the PBIAS. These metrics were given qualitative ranges for water flux and sediment load in *Moriasi et al.* [2007] (Table 3.4).

These metrics were calculated for the monthly ensemble averages of the synthetic, GCM-driven sediment values for 1965-1986 and the synthetic water flux values for 1965-1994. These periods were chosen based on availability of observational data. Additionally, we checked for any biases in the model ensembles by computing for each model in a given ensemble discharge and sediment seasonal hydrographs, averaged over 1965-1994, and 1965-1986, respectively. The resulting set of seasonal hydrographs for each scenario was then compared to observations using a t-test to check for any significant differences.

After checking historical results against observations, we then compared the results of the simulation from 1965-1994 to those of 2065-2094 to assess potential changes in sediment dynamics due to changes in climate/hydrological regime. The baseline period was chosen to include all sediment observations and be within the historical period of the GCM models used; the future period was chosen to be 100 years after the baseline. We investigated changes in sediment generation, storage, timing and yield across the basin.

To investigate changes in sediment generation within the FRB, we computed for each scenario and season the ensemble mean and range of the difference in mud generation between the future (2065-2094) and baseline (1965-1994) periods. Because the model assumes sand is not supply limited, the hillslope generation mechanism only produces mud, hence, we limit our discussion to mud. We analyzed the changes in mud generation within the

two major sources of the FRB's mud: the Rocky and coastal mountains. All changes from baseline values were then tested for significance using a two-sample t-test and $\alpha = 0.05$ with sample sets consisting of results from each model in the ensemble. Unless explicitly stated, all changes in mud generation presented in Section 4.4 are significant.

For storage analysis, the ensemble mean of the FRB's mud supply at the end of 2094 was compared to the mud generated from 1965-2094 to identify the locations of any long term sinks for each scenario. Additionally, as with hillslope generation, for each scenario and season the ensemble average of the difference in mud supply between the future (2065-2094) and baseline (1965-1994) periods was computed to analyze seasonal changes in mud storage within the basin.

Sediment timing and yield was analyzed at all stations using 4 properties: total yield, and spring, centroid, and persistence timings, which are defined as the day at which 10%, 50%, and 95% of the annual sediment load has been transported, respectively. Changes in all of these properties were tested for significance using a two-sample t-test and $\alpha = 0.05$ with sample sets consisting of results from each model in the ensemble. Significant changes were compared to their analogous water flux properties using Kendall's τ and R^2 to investigate the role of changes in water flux in changes in sediment load and the ability of changes in water flux properties to predict changes in sediment load. Kendall's tau is a rank coefficient ranging from -1 (complete negative correlation) to 1 (complete positive correlation) that evaluates correlation between two random variables without using any assumptions on the underlying structure between them. It is defined for a set of n joint observations (x_i, y_i) of random variables X and Y using the number of concordant and discordant pairs (n_c and n_d, respectively) as

$$\mathrm{K}\tau = \frac{n_c - n_d}{n(n-1)/2}, \tag{4.8}$$

where a pair (x_i, y_i) and (x_j, y_j) (with $i \neq j$) are concordant if $(x_i - x_j)(y_i - y_j) > 0$ and discordant if $(x_i - x_j)(y_i - y_j) < 0$. Both K$\tau$ and R^2 were tested for significance. Unless explicitly stated, changes in annual yield, spring timing, centroid timing, and persistence timing and Kτ and R^2 values mentioned in the results are significant. In addition to this analysis, we checked for changes in the variability in year to year monthly peak sediment loads using the coefficient of variation (CV).

4.3 Study Site and Input Data

4.3.1 Study Site

The Fraser River runs 1,400 km from headwaters in the Rocky Mountains to its outlet into the Pacific Ocean at Vancouver. At 230,000 km^2 in drainage area, the FRB is the largest watershed in British Columbia, Canada (B.C.). It is both recreationally and economically important to the province of B.C. The river system provides habitat for over 100 species of fish including all five species of pacific salmon. Over 75% of the basin is forested (*Schnorbus et al.* [2010]) and accounts for a large percentage of the trees used in B.C.'s harvesting industry. Overall, 80% of the provincial gross domestic product and 10% of the federal GDP comes from within the FRB (*Canadian Heritage Rivers Systems* [2015]). Roughly 60% B.C.'s population resides in the delta region of the FRB near the river's outlet. Importantly, this region is downstream of Mission, the gauging station farthest downstream in our study. Because we stop our analysis at Mission, we do not model the confounding tidal effects nor anthropogenic influences seen in the Fraser's delta.

Hydro-climatically, the basin is often divided into three regions: i) an eastern mountain portion (Rocky Mountains), ii) an interior plateau, and iii) a coastal mountain portion. The mountainous eastern portion has the highest elevations and is characterized by steep valleys shaped by glaciers. Peaks in both water and sediment flux are snowmelt driven and tend to occur in late spring or early summer with sediment peaks occurring first and showing some hysteresis relative to water flux.

The FRB was chosen to test our adapted model for three main reasons. First, historical sediment load and river discharge data are available from the WSC for several stations across the basin (Table 2.1). Second, the diverse landscape, ecology, and climate represent the heterogeneity common in large basins. Third, the basin experiences relatively low anthropogenic disturbance upstream of Mission, with agricultural and urban influences either limited in scale or confined to the basin's delta, $< 5\%$ of B.C's population upstream of Mission, and only two small hydroelectric dams in the Nechako (25,000 km^2 drainage area) and Bridge-Seton (4,700 km^2 drainage area) sub-basins. The impact of the Nechako reservoir on annual discharge at the Fraser River outlet has been calculated to range from 1 to 6 percent (*Moore* [1991]). Furthermore, it is located in the interior plateau where sediment generation is already expected to be at a minimum.

4.3.2 Input Data

To validate river discharge, we use observations made available by the Water Survey of Canada (WSC) at 14 stations from 1965-1994 (Figure 2.1). Because the Nechako reservoir affects the discharge hydrograph of the Nechako basin, validation is performed against naturalized flow (provided by PCIC) at Nechako, Hope, and Mission. Naturalized flows at the other downstream stations, Marguerite and Agassiz, were not available from PCIC; however, the impact of the reservoir at these locations is expected to be small as the average annual reduction in water flux out of Nechako due to the reservoir is approximately 6.5% and 3.5% of the annual discharge at Marguerite and Agassiz, respectively.

Landscape data in this study, including river reservoir height and width relations, lake locations, and soil texture, are taken from Chapter 3. River elevation, river direction, hillslope gradient, and river gradient at $1/16^\circ \times 1/16^\circ$ come from upscaling the USGS's 15 arc-second Global Multi-resolution Terrain Elevation Data map (*Danielson and Gesch* [2011]) following the methods described in Chapter 2.

Readily available for use as hydrological inputs to our model are outputs from climate scenario-driven VIC model simulations performed on the FRB in *Shrestha et al.* [2012] (https://pacificclimate.org/data). The scenarios come from the Coupled Model Intercomparison Project phase 3 (CMIP3) developed in 2007 (*Meehl et al.* [2007]). Since then, there has been an update from the Special Report on Emission Scenarios (SRES) used in CMIP3 to new Representative Concentration Pathways (RCP) scenarios. However, because of the availability of the validated VIC runs, done with downscaled output from CMIP3 models, we perform our modelling starting from SRES scenarios A1B, B1, and A2 rather than the new RCP scenarios. Roughly, the radiative forcings in SRES A1B and B1 are similar to those of RCP6.0 and RCP4.5, respectively and A2's radiative forcing is somewhere between the radiative forcing of RCP6.0 and that of RCP8.5 (*IPCC* [2014]). Below, we provide a brief overview of the models and methods used by *Shrestha et al.* [2012].

SRES scenarios, GCMs, BCSD, VIC

In *Shrestha et al.* [2012], the authors considered three SRES climate scenarios: A1B, B1, and A2. Details on each scenario are provided in *IPCC* [2007]; roughly, all three scenarios represent futures where greenhouse gas emissions and global surface temperatures rise above present day values, but increases

are more pronounced in scenarios A1B and A2 than in B1. These scenarios were used to drive the GCMs which in turn created climatic drivers for VIC

The GCM outputs used by *Shrestha et al.* [2012] come from the CMIP3 multi-model dataset (*Meehl et al.* [2007]). The CMIP3 project gives results from a total of 24 GCMs. In studies such as *Kay et al.* [2009], *Prudhomme and Davies* [2009a], *Prudhomme and Davies* [2009b], and *Najafi et al.* [2011], researchers found that the structure of the GCM was the largest source of uncertainty in assessing hydrological impacts. To account for this uncertainty, outputs from 8 CMIP3 GCM simulations were used as inputs to VIC. The 8 GCMs were selected from the larger set based on robustness and their ability to simulate historical data globally, in the Northern Hemisphere, in North America, and on the western coast of North America. The GCM simulations used in this study are listed in Table 4.1. Details on the GCM selection process and individual model performance are provided in *Werner* [2011]. With the exception of UKMO-HadGEM1, which does not simulate emission scenario B1, outputs of each GCM under scenarios A2, A1B, and B1 were used as inputs to VIC for a total of 23 simulations. Each simulation produced monthly precipitation and temperature outputs.

Table 4.1: GCMs used in study

GCM	**Atmospheric Resolution**	**Reference**
CCSM3	T85 L26	*Collins et al.* [2006]
CGCM3.1(T47)	T47 L31	*Scinocca et al.* [2008]
CSIRO-Mk3.0	T63 L26	*Rotstayn et al.* [2010]
MPI-OM ECHAM5	T63 L18	*Roeckner et al.* [2006]
GFDL CM2.1	N45 L24	*Delworth et al.* [2006]
MIROC3.2 (medres)	T42 L20	*K-1 Model Developers* [2004]
UKMO-HadCM3	T42 L19	*Collins et al.* [2001]
UKMO-HadGEM1*	N96 L38	*Martin et al.* [2006]

* Does not simulate scenario B1.

Prior to being used as inputs to VIC, the climatological variables produced by the GCMs were downscaled both spatially and temporally using The Bias Corrected Spatial Disaggregation (BCSD) method. Roughly, the method downscales in three steps: 1) bias correction, 2) spatial disaggregation, and 3) temporal disaggregation. For more details, the reader is referred to *Wood et al.* [2004].

Once the climatological variables had been disaggregated, they were used as inputs to the land surface hydrological model VIC developed in *Liang et al.* [1994] and *Liang et al.* [1996]. Details of the calibration and validation of VIC on the FRB are provided in *Schnorbus et al.* [2011] and *Shrestha et al.* [2012]. Roughly, model parameters were calibrated using the Multi-Objective Complex Evolution Method (see *Yapo et al.* [1998]) with three objective functions: the Nash-Sutcliffe coefficient of efficiency (NSE), the Nash-Sutcliffe coefficient of efficiency of the log-transformed discharge (LNSE), and the water balance error (WBE). Validation was performed for a 5-year period on 11 sub-basins. Generally, peak discharge was well-matched with NSE and LNSE values being greater than 0.70 for 9 of 11 sub-basins delineated in the study.

The results of the simulations performed in *Shrestha et al.* [2012] show an overall increase in future mean annual temperature across the basin with low variability between GCMs and increases in scenario A1B and B1 being the largest and smallest, respectively. Precipitation was also found to increase across the basin, though there was high spatial and inter-GCM variability. Generally, increases in the northern portion of the basin were highest, with precipitation increases in the eastern mountains being more pronounced than in the coastal mountains. Between scenarios, B1 had the highest increase in precipitation. Seasonally, all scenarios showed a general increase in precipitation between October and June and decreases between July and August, though in the coastal mountains the increase was primarily from October to January after which point levels returned to baseline until June. Snow storage generally decreased in all scenarios which led to a transition from a snow-dominant regime to a hybrid regime in the coastal and eastern mountains and a transition from a hybrid regime to rain-dominant regime in the interior plateau.

Hydrologically, there was an overall increase in winter and spring runoff and a decrease in summer and autumn runoff. These changes were likely due to the changes in seasonal precipitation, transitions from snow-dominated to hybrid regimes and from hybrid to rain-dominated regimes, and warmer temperatures causing an earlier snowmelt. The three scenarios all demonstrated an increase in annual discharge, with scenario B1 showing the greatest change due to its relatively large increase in precipitation and milder temperature increase.

Stationary Inputs

By running the model of Chapter 3 as calibrated for the 1965-1986 period over the 1965-2094 time period, we implicitly assume several variables and relationships remain stationary throughout the time of simulation. These include the hydrometric relationships that determine river reservoir width and height, the hysteresis parameters that dictate critical channel shear stress, and bank-full height. We also assume that the mechanism for hill-slope erosion and sediment will continue to be overland flow. While it is possible that a combination of changes to land use, vegetation, dominate hillslope detachment mechanisms, and potential mass wasting events such as a large-scale fire or earthquake may violate these assumptions, we view these possibilities as outside of the scope of our study. There has been a historical lack of earthquakes affecting the FRB, anthropogenic influence is minimal upstream of Mission, and using data from *Canadian Forest Service* [2016], we estimate that an average of only 23,000 ha of the FRB (0.1% of the basin's total area) is affected by wildfire. Though forest wildfires are expected to increase in likelihood in some regions due to climate change (*Gonzalez et al.* [2010]), we consider accounting for this change outside the scope of this work.

4.4 Results

4.4.1 Historical Dynamics: 1965-1994

Overall, the seasonality of water flux and sediment load across the basin were well-simulated by the ensemble mean which showed very little variance amongst scenarios (Table 4.2). Following the standards outlined by *Moriasi et al.* [2007] (Table 3.4), NSE values of water flux were "very good" at 12 of the 14 stations and only "unsatisfactory" at Nechako, the downstream station nearest the Nechako reservoir. PBIAS values for water flux were "very good" or "good" at 12 stations and "unsatisfactory" only at Nechako. NSE values for sediment flux, for which observations were only available from 1965-1986 and at five stations, were "very good" at four of the five stations and "good" at the remaining station, Marguerite. All five PBIAS values of sediment load were either "very good" or "good."

However, because our simulations had relatively little variance in historic water flux and sediment load amongst GCMs there was a general tendency for all GCM models within an ensemble to under-predict water flux from the fall through the spring and over-predict water flux in the summer (Figure

Table 4.2: NSE and PBIAS results for seasonally averaged ensemble means of water flux and sediment load during 1965-1994 (water flux) and 1965-1986 (sediment load). Reported values are averages of ensemble results from scenarios A1B, A2, and B1.

	Water Flux		Sediment Load	
Station	NSE	PBIAS (%)	NSE	PBIAS (%)
Agassiz	0.90^{**}	-11^{*}	0.83^{**}	-16^{*}
Hansard	0.89^{**}	-8^{**}	0.78^{**}	-1^{**}
Hope	0.89^{**}	-8^{**}	0.77^{**}	-16^{*}
Marguerite	0.89^{**}	-3^{**}	0.69^{*}	4^{**}
Mission	0.89^{**}	-7^{**}	0.91^{**}	20^{*}
Chilcotin	0.81^{**}	$-22^{\S}$		
Harrison	0.81^{**}	-7^{**}		
Nechako	$0.63^{\S}$	$-28\dagger$		
North Thompson	0.82^{**}	$-16^{\S}$		
Quesnel	0.91^{**}	-13^{*}		
Shelley	0.86^{**}	-7^{**}		
South Thompson	0.95^{**}	$< -1^{**}$		
Stuart	$0.48^{\dagger}$	-14^{*}		
Thompson	0.89^{**}	-11^{*}		

§, *, **, and † indicate satisfactory, good, very good, and unsatisfactory metric values, respectively (as dictated by *Moriasi et al.* [2007]).

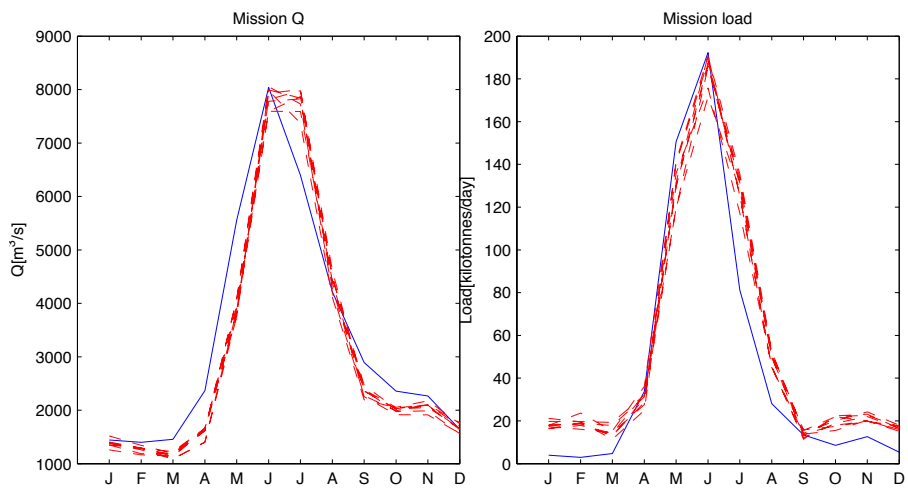

Figure 4.2: Observed and GCM ensemble seasonal a) water flux and b) sediment load at Mission for scenario A1B from 1965 to 1994. Observed values are in blue, simulated values of all GCMs in the ensemble are in red. Scenarios A2 and B1 show similar results.

4.2(a)). The GCMs under-predicted sediment load in the spring and over-predicted load from the summer through the winter (Figure 4.2(b)). These tendencies were small enough that the simulations still gave relatively high NSE values and low PBIAS values, but due to their presence we choose to frame the results of simulations of the future dynamics as relative (rather than absolute) changes to the 1965-1994 baseline.

4.4.2 Simulations of Future Dynamics (1965-1994 vs. 2065-2094)

We assess the impacts of future potential changes in climate and hydrology to sediment dynamics by comparing simulation results from a baseline period (1965-1994) to the results of a future period (2065-2094). We consider changes to dynamic properties such as the timing and yield of sediment load, the seasonal distribution of hillslope erosion, and sediment sinks/sources

throughout the basin. To control for GCM biases, all changes in sediment dynamics are presented as relative to the baseline period.

Hillslope generation

All models for every scenario project increased annual mud production within the basin in the future period (Table 4.3). For each scenario, models within the ensemble project this increase to range from ∼20-75 Mt or an increase of roughly 15-60% above baseline production. Ensemble averages for each scenario give a smaller range of 46 Mt (B1) to 59 Mt (A2), or 35-45% of baseline levels. In most simulations, over 50% of this increase is produced within the Rocky Mountains which represents less than 40% of the FRB's area and at baseline produced under 30% of the FRB's mud (Table 4.3). Variability in both coastal and Rocky mountain mud generation was higher between models than between scenarios (Appendix A). The spatial and temporal patterns in changes to hillslope generation are similar across all three scenarios. Generally, scenario B1 shows the smallest relative changes and scenario A2 shows the largest.

Seasonally, the FRB in the future period shows an increase in mud generation in the coastal mountains of 2-10 Mt and more moderate increase of 0.4-3 Mt in the northern Rocky Mountains from January to March (Figure 4.3a, Table 4.3). However, the amount of mud generated within the Rocky Mountains relative to the entire basin's mud generation during this time is projected to increase from baseline levels while the contribution of the coastal mountains shows a decrease (Table 4.3). Overall, simulations show the basin's mud generation during the Jan-Mar period increasing from 4% of the FRB's yearly production at baseline to 5-10% in the future period. This increase is likely a reflection of the increasing temperature across the FRB and earlier snowmelt in mountainous regions.

During the Apr-Jun period, increase in generation within the Rocky Mountains is expected to be more widespread with ensemble averages projecting the region to produce 14 Mt (B1) to 21 Mt (A2) more mud and increasing its relative contribution from 29% to 31-44% of the seasonal production (Figure 4.3b and Table 4.3). The coastal mountains are expected to decrease in mud generation at lower altitudes where snowmelt has already occurred and reduce their relative contribution, but still have an overall increase in production with ensemble averages ranging from 12 Mt (B1) to 15 Mt (A1B). All ensemble averages project the Apr-Jun percentage of yearly mud production to increase from its baseline. As with annual increases, model variability within a scenario is larger than ensemble average vari-

Table 4.3: Ensemble averages and ranges (given in parenthesis) of changes in the fraction of annual mud generation produced in each season (Seas/Yr) and seasonal hillslope mud generation within the Rocky (RM) and coastal (CM) mountains from baseline (1965-1994) to future (2065-2094) periods for scenarios A1B, B1, and A2. Red values represent decreases from baseline. Baseline basin wide seasonal generation is ∼(5, 55, 60, 10) Mt for (Jan-Mar, Apr-Jun, Jul-Sep, Oct-Dec).

Scenario	Δ RM (Mt)	Δ CM (Mt)	RM/FRB (%)	CM/FRB (%)	Seas/Yr (%)
			Jan-Mar		
A1B	2 (1-3)	5 (2-8)	14(11-20)	66 (61-70)	8 (5-10)
A2	2 (1-3)	6 (4-10)	16 (12-22)	65 (63-71)	8 (7-11)
B1	1 (<1-2)	5 (3-8)	14 (8-21)	66 (61-70)	8 (6-9)
base	-	-	7	70	4
			Apr-Jun		
A1B	20 (5-38)	15 (6-28)	40 (32-44)	53 (50-61)	50 (38-64)
A2	21 (10-41)	15 (3-32)	41 (37-44)	52 (49-56)	49 (39-63)
B1	14 (3-31)	12 (4-26)	37 (31-41)	55 (52-60)	47 (37-59)
base	-	-	29	60	43
			Jul-Sep		
A1B	3† (6-13)	8 (23-3)	39 (34-47)	55 (48-59)	29 (13-39)
A2	3† (7-12)	7 (23-2)	39 (37-41)	55 (53-57)	29 (14-37)
B1	4† (6-13)	3 (16-4)	37 (33-42)	58 (53-60)	35 (18-46)
base	-	-	30	64	46
			Oct-Dec		
A1B	3 (2-5)	10 (7-13)	17 (15-20)	68† (64-72)	13 (12-16)
A2	3 (2-6)	10 (6-16)	18 (16-21)	67 (64-70)	14 (11-15)
B1	2 (1-3)	7 (4-11)	16 (14-17)	69† (68-71)	11 (10-13)
base	-	-	14	70	7
			Annual		
A1B	27 (9-42)	21 (13-38)	35 (30-39)	57 (54-62)	
A2	29 (16-50)	24 (7-47)	35 (34-37)	56 (55-58)	
B1	21 (10-32)	20 (6-30)	33 (31-35)	58 (57-61)	
base	-	-	28	62	

† indicates values that are **not** statistically significant ($\alpha = 0.05$).

ability amongst scenarios during this period with projected increases in the Rocky and coastal mountain mud generation ranging over roughly an order of magnitude amongst models within the same scenario ensemble.

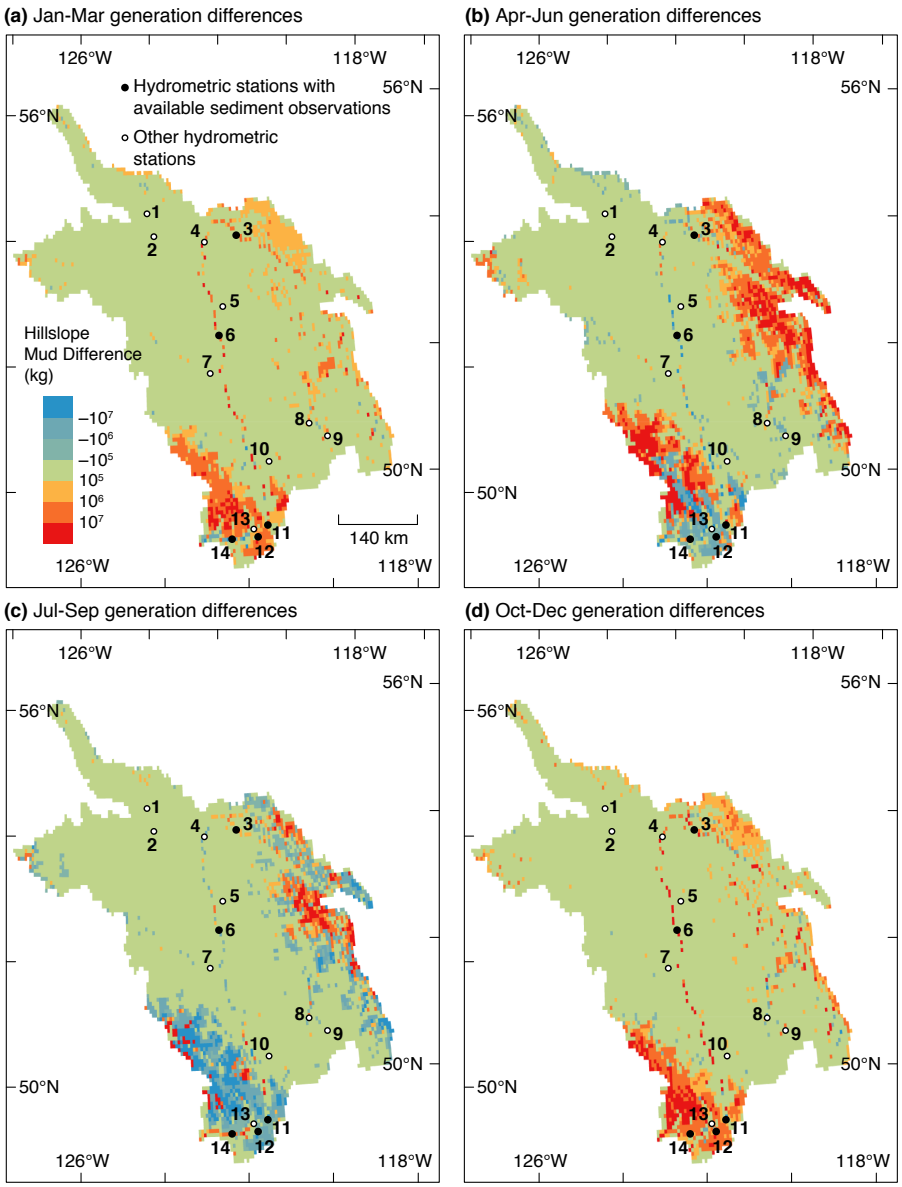

Figure 4.3: Ensemble mean difference in hillslope mud generation between future (2065-2094) and baseline (1965-1994) periods for A1B scenario for Jan-Mar (a), Apr-Jun (b), Jul-Sep (c), and Oct-Dec (d). Positive values indicate future values are larger than baseline values. Scenarios A2 and B1 show similar results (see Appendix A).

The Jul-Sep period is marked by a widespread decrease in mud generation within the coastal mountain range and, as in the coastal mountains during the Apr-Jun period, a decrease in generation in the lower topographical portions of the Rocky Mountains where snow storage has already been exhausted (Figure 4.3c). The coastal mountains are projected to experience a decrease in mud production during Jul-Sep in the future period, while the Rocky Mountains show no statistically significant change in any of the three scenarios (Table 4.3). Again, there is more variability between models than between scenarios. For example, model projections of the change in the coastal mountains within A1B range from a decrease of 23 Mt to an increase of 3 Mt while ensemble averages all predict a decrease ranging from 3-8 Mt. Every model in all three scenarios project the relative contribution of the coastal mountains to decrease and the contribution of the Rocky Mountains to increase. Overall, simulations project the future Jul-Sep period to decrease in its percentage of yearly mud production.

The Oct-Dec period shows results similar to the Jan-Mar period with moderate increases in mud generation in the Rocky Mountains and larger increases in the coastal mountains (Figure 4.3d, Table 4.3). There is a slight increase in the relative contribution of the coastal mountains while scenarios A1B and B1 show no statistically significant change in the contribution of the Rocky Mountains and scenario A2 shows a small decrease. The percentage of yearly mud produced in the Oct-Dec period increased slightly from 7% at baseline to 10-16% in the future period.

Storage

Generally, there was more variance amongst ensembles than amongst scenarios in terms of storage (Appendix B), though all scenarios and models produced relatively similar results regarding the spatial distribution and seasonal changes of storage within the FRB (Figure 4.4). Overall, the basin retained roughly 90% of the mud generated between 1965 and 2094. Two significant long-term sinks within the basin were identified: the Harrison sub-basin (outlet at Gauge 13) and the Thompson sub-basin (outlet at Gauge 10) (Figure 4.4). These watersheds are part of the coastal and Rocky mountains, respectively, and produce 30-40% and 15-25% of the basin's mud. The Harrison sub-basin retains over 99% of its generated mud while the Thompson sub-watershed retains over 95%. The Nechako watershed, though its mud contribution and supply is relatively small, displays similar behavior, retaining over 99% of its generated mud. All three of these sub-basins are characterized by lakes near their outlet. Seasonal supply within the Rocky

and coastal mountain ranges is generally synchronous with mud generation (Figure 4.3). The coastal mountains see an increase in storage during Jan-Jun (Figures 4.4a and 4.4b), a decrease during Jul-Sep (Figure 4.4c) and an increase during Oct-Dec (Figure 4.4d). Seasonal changes in the Rocky Mountain mud storage was mostly restricted to an increase during Apr-Jun.

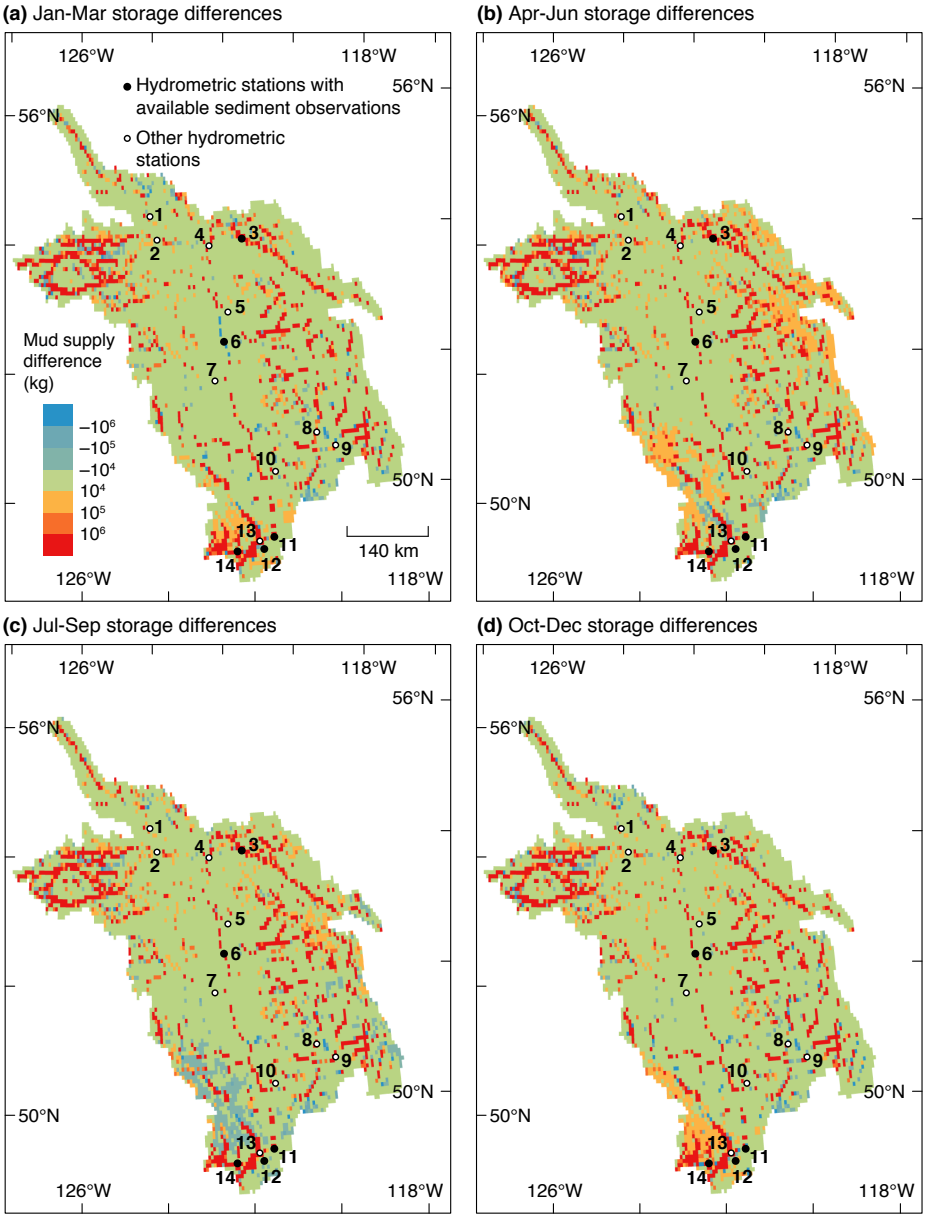

Figure 4.4: Ensemble mean difference in storage between future (2065-2094) and baseline (1965-1994) periods for A1B scenario for Jan-Mar (a), Apr-Jun (b), Jul-Sep (c), and Oct-Dec (d). Positive values indicate future values are larger than baseline values. Scenarios A2 and B1 show generally similar spatial dynamics (see Appendix B).

Sediment timing and yield

A shift towards earlier spring timing is projected in all scenarios at all stations and a shift towards earlier centroid timing is projected at every station for all scenarios with the exception of A2 at Agassiz. No scenario projects a change in persistence timing at North Thompson or Stuart, while the remainder of the stations are generally expected to show a delay in persistence timing. Scenario B1 simulates the most widespread change in annual sediment yield, projecting increases at all stations except for South Thompson and Thompson. Scenario A1B simulated the least widespread change, projecting no significant changes in South Thompson, Harrison, Chilcotin, Thompson, and Hope. Persistence timing showed the least widespread correlation to its analogous Q property, while changes in annual sediment yield were generally found to be correlated to changes in annual water flux. Sediment centroid timing is typically correlated to the centroid timing of Q outside of small, northern sub-basins (Hansard, Nechako, and Shelley) and the spring timing of sediment yield is generally correlated to the spring timing of Q away from mountainous sub-basins. In each scenario, the CV of year to year peak monthly sediment load is generally projected to decrease or show no change in the small northern basins (Hansard, Shelley, Nechako, and Stuart) and increase across the remainder of the basin.

In the following sub-sections, we restrict our analysis to the results at four sub-basins in four distinct regions within the FRB: 1) the western interior plateau 2) the Rocky Mountains, 3) the coastal mountains, and 4) the outlet. Results from the remaining sub-basins can be found in Appendix C.

FRB Outlet: Mission (Gauge 14) Simulation results produce significant differences at Mission in future and baseline yield and all three timing variables for all climate scenarios (Table 4.4). Annual sediment yield at Mission is projected to increase 2-3 Mt with the sediment hydrograph reaching its spring and centroid yield earlier and persisting longer (Figure 4.5). With the exception of CCSM3 in scenario B1, all simulations of A2 and B1 simulate an increase in the CV of year to year peak monthly sediment loads with the average increase in both scenarios being roughly 30%. While scenario A1B also showed an average increase in the CV of peak monthly sediment loads (35%), three of eight GCMs (CCSM3, CSIRO35, and HadCM) project slight decreases. In all three scenarios, an increase in fall and winter sediment loads were responsible for the overall increase in annual sediment yield, with transport during peak months actually showing a reduction in the future period not seen in the discharge hydrograph (Figure 4.5), indicating

that it is potentially due to supply limitations rather than a reduction in stream power.

Results at Mission are generally congruous with the results of *Shrestha et al.* [2012], the seasonal hillslope supply (Figure 4.3), and the conceptualization that warmer temperatures will lead to earlier snowmelt and spring water flux, which result in earlier sediment loads in watersheds where overland flow is the dominate sediment supply generator. With the exception of sediment persistence timing, which shows no significant correlation with the persistence of Q in any scenario, sediment properties at Mission are generally correlated to water flux properties (Table 4.4).

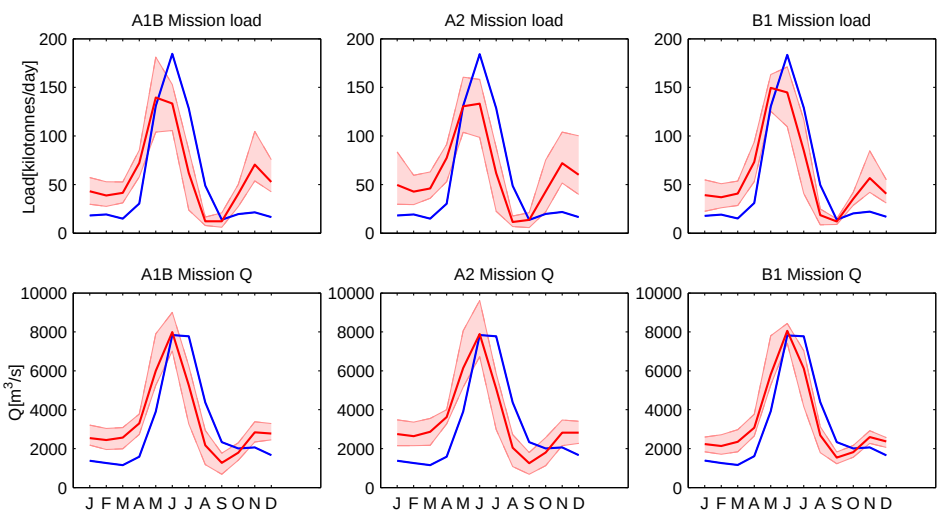

Figure 4.5: Seasonal Q and suspended sediment load at Mission for scenarios A1B, A2, and B1 for baseline (blue line) and future ensemble mean (red line) and future ensemble range (red region).

Rocky Mountains: Hansard (Gauge 3) At Hansard, simulations project an increase in annual yield, earlier spring and centroid timings, and later persistence timings in all scenarios (Table 4.5) while the CV of year to year peak monthly sediment load is roughly unchanged. The changes in spring and centroid timing appear to be products of a shift in the sediment hydrograph towards an earlier rising limb while the change in persistence timing is likely caused by the increased sediment load between September and Decem-

Table 4.4: Comparison of baseline and future projected values at Mission of average sediment spring, persistence, and centroid timing, and yield. "Δ" is computed as average future value minus average baseline value. Annual baseline yield at Mission was ∼20 Mt.

Mission						
	Spring Timing			Persistence Timing		
Scenario	Δ(days)	Kτ	R^2	Δ(days)	Kτ	R^2
A1B	-36	0.86	0.90	59	$0.43^{\dagger}$	$0.30^{\dagger}$
A2	-42	0.79	0.72	55	$0.14^{\dagger}$	$0.11^{\dagger}$
B1	-33	$0.24^{\dagger}$	0.79	37	$0.14^{\dagger}$	$0.06^{\dagger}$
	Centroid Timing			Yield		
	Δ(days)	Kτ	R^2	Δ(Mt)	Kτ	R^2
A1B	-8	0.64	0.62	2.1	0.71	0.62
A2	-9	0.64	0.67	2.8	0.93	0.93
B1	-12	0.81	0.68	2.5	0.90	0.91

† indicates values that are **not** statistically significant ($\alpha = 0.05$).

ber (Figure 4.6). The increase in sediment yield appears primarily between April and July and secondarily between September and December. These results are consistent with earlier snowmelt in the region and our projections of increased hillslope supply in the northern Rocky Mountains, particularly from April-March (Figure 4.3). However, with the exception of the change in annual yield in scenario A2, the changes in sediment were not significantly correlated with changes in Q. This may suggest that shifts in the sediment output at Hansard are driven by alterations in supply rather than fluvial changes.

Coastal Mountains: Harrison (Gauge 13) Though the Harrison basin is situated directly in the coastal mountains, its outlet is also directly upstream of Lillooet Lake and Harrison Lake, hence, results from Harrison must be viewed with this caveat in mind. Simulations only showed a significant change in annual sediment yield in scenario B1 where it is expected to increase in the future period (Table 4.6). However, all simulations in all scenarios projected an increase in the CV of year to year peak monthly sediment with average increases ranging from 60% (B1) to 100% (A2). All timing variables show a significant change with spring and centroid tim-

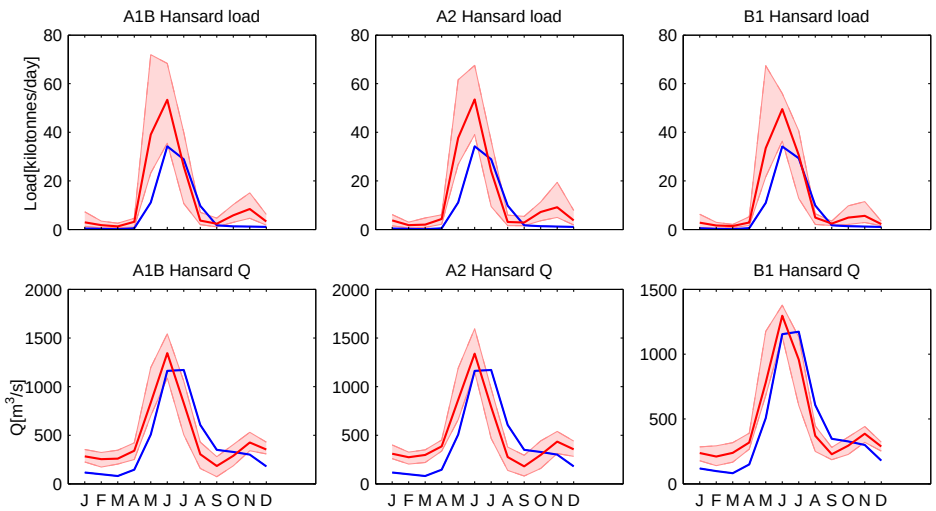

Figure 4.6: Seasonal Q and suspended sediment load at Hansard for scenarios A1B, A2, and B1 for baseline (blue line) and future ensemble mean (red line) and future ensemble range (red region).

ing decreasing and persistence timing increasing in each scenario. The lack of change in annual sediment yield at Harrison in scenarios A1B and A2 is likely due to trapping in Lillooet and Harrison Lakes, since the coastal mountains are projected to significantly increase sediment production in the future period in both of these scenarios (Table 4.3). Changes in sediment centroid and persistence timings are correlated to changes in their analogous Q properties in all scenarios except for A1B where no significant Kendall's τ correlation was found between the persistence timings. The changes in peak and winter sediment yield timing generally aligned with the changes in Q caused by earlier snowmelt (Figure 4.7). The projected relationship between changes in the spring timing of sediment and that of Q was mixed with scenario B1 showing a relatively high correlation (Kτ, $R^2 > 0.70$), A2 showing no significant correlation, and A1B only showing a significant correlation in Kτ. This is in contrast to Hansard, another mountainous sub-basin, where generally sediment changes were not correlated to changes in Q. Again, it is likely that this difference in results is due to the effect of upstream lakes.

Table 4.5: Comparison of baseline and future projected values at Hansard of average sediment spring, persistence, and centroid timing, and yield. "Δ" is computed as average future value minus average baseline value. Annual baseline yield at Hansard was ∼3 Mt.

Hansard

	Spring Timing			Persistence Timing		
Scenario	Δ(days)	Kτ	R^2	Δ(days)	Kτ	R^2
A1B	-23	0.36†	0.22†	33	0.07†	0.01†
A2	-27	0.07†	0.13†	43	0.07†	0.07†
B1	-18	0.62†	0.50†	20	0.52†	0.24†
	Centroid Timing			Yield		
	Δ(days)	Kτ	R^2	Δ(Mt)	Kτ	R^2
A1B	-16	0.33†	0.40†	1.8	0.43†	0.41†
A2	-17	0.36†	0.46†	1.9	0.57†	0.56
B1	-15	0.33†	0.66	1.6	0.52†	0.49†

† indicates values are **not** statistically significant ($\alpha = 0.05$).

Table 4.6: Comparison of baseline and future projected values at Harrison of average sediment spring, persistence, and centroid timing, and yield. "Δ" is computed as average future value minus average baseline value. Annual baseline yield at Harrison was ∼0.3 Mt.

Harrison

	Spring Timing			Persistence Timing		
Scenario	Δ(days)	Kτ	R^2	Δ(days)	Kτ	R^2
A1B	-38	0.64	0.43†	55	0.57†	0.50
A2	-39	0.50†	0.34†	62	0.69	0.81
B1	-35	0.71	0.77	35	0.81	0.75
	Centroid Timing			Yield		
	Δ(days)	Kτ	R^2	Δ(Kt)	Kτ	R^2
A1B	-15	0.86	0.89	6†	-	-
A2	-10	0.79	0.59	1†	-	-
B1	-11	1.00	0.95	14	0.43†	0.25†

† indicates values are **not** statistically significant ($\alpha = 0.05$).

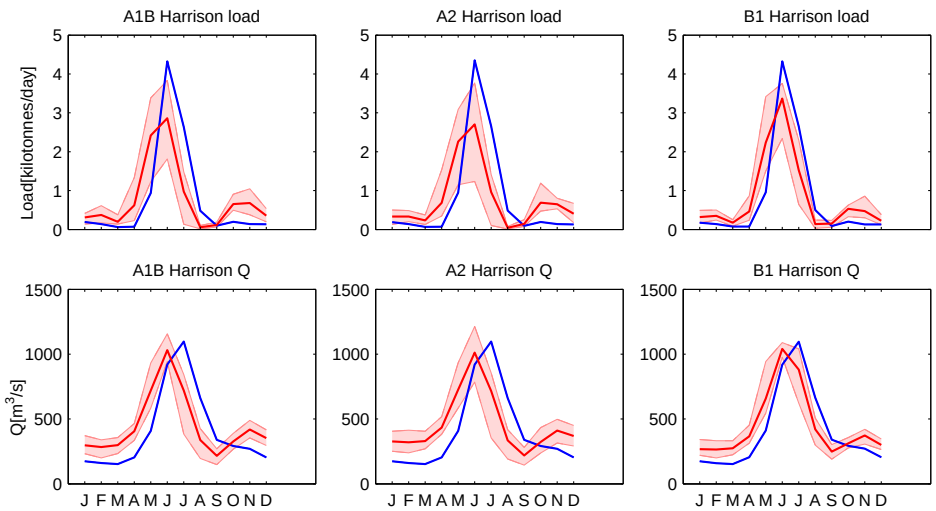

Figure 4.7: Seasonal Q and suspended sediment load at Harrison for scenarios A1B, A2, and B1 for baseline (blue line) and future ensemble mean (red line) and future ensemble range (red region).

Western Interior Plateau: Chilcotin (Gauge 7) Though some headwaters of the Chilcotin basin are connected to the coastal mountains, for our purposes, we characterize the watershed as mainly within the interior plateau since we expect much of the coastal sediment to be trapped by Chilko Lake in the south-western portion of the watershed. With the exception of CSIRO35 in scenarios A1B and B1, all simulations of Chilcotin project an increase in the CV of year to year peak monthly sediment load with average increases ranging from 20% (A1B) to 35% (B1). Only scenario B1 displays a significant increase in annual sediment yield while spring and centroid timings are projected to decrease in all scenarios (Table 4.7). Unlike the other sub-basins discussed, persistence timing is expected to decrease in scenarios A1B and B1. *Shrestha et al.* [2012] noted while the mountainous regions of the FRB were projected to have larger autumn runoff than winter runoff, parts of the interior plateau began to show the opposite relationship as the region transitioned from a hybrid to rain-dominated regime. In Chilcotin, the relationship shifts from autumn runoff being larger at baseline, to autumn and winter runoff being roughly the same in the future period (Figure 4.8). This effect may help explain the decrease in persistence timing in the

Table 4.7: Comparison of baseline and future projected values at Chilcotin of average sediment spring, persistence, and centroid timing, and yield. "Δ" is computed as average future value minus average baseline value. Annual baseline yield at Chilcotin was ∼1 Mt.

Chilcotin						
	Spring Timing			Persistence Timing		
Scenario	Δ(days)	Kτ	R^2	Δ(days)	Kτ	R^2
A1B	-34	0.86	0.91	-4	0.29†	0.56
A2	-40	0.93	0.91	-4†	-	-
B1	-26	0.62†	0.75	-8	0.81	0.86
	Centroid Timing			Yield		
	Δ(days)	Kτ	R^2	Δ(Kt)	Kτ	R^2
A1B	-23	0.69	0.92	72†	-	-
A2	-23	0.86	0.91	69†	-	-
B1	-18	1.00	>0.99	105	1.00	0.99

† indicates values are **not** statistically significant ($\alpha = 0.05$).

future period as changes in sediment persistence timing were significantly correlated to changes in the persistence timing of Q in both scenarios where significant changes were found. Generally, projections of Chilcotin display some of the strongest correlations between sediment and water flux, suggesting that in areas were mud supply is limited, changes in sediment are better predicted by changes in Q.

4.5 Discussion and Conclusions

To the authors' knowledge, this study is the first to use a distributed, physically-based model to simulate sediment dynamics within a large-scale river system under changing climate scenarios. The simulations in this study project a number of substantive changes to sediment dynamics related to future changes in climate and hydrology. These include a significant increase in annual yield, an increase in hillslope erosion, changes in the distribution of sediment generation within the basin, and alterations in the timing of sediment load and distribution of hillslope-supplied mud. Though the hydrological response of mountainous basins to changing climate depends on many site-specific characteristics, our projections are consistent with ob-

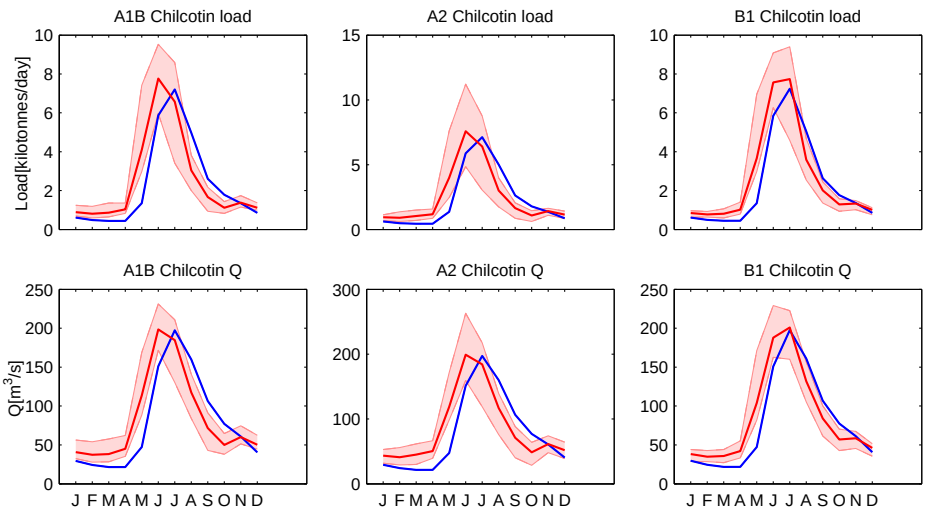

Figure 4.8: Seasonal Q and suspended sediment load at Chilcotin for scenarios A1B, A2, and B1 for baseline (blue line) and future ensemble mean (red line) and future ensemble range (red region).

served shifts towards earlier spring and centroid streamflow in western North America (*Stewart* [2009]).

In all scenarios, the basin is expected to generate and yield more sediment. Scenario A2 produced the largest ensemble average increase of 2.8 Mt/a (14% over baseline) while A1B's ensemble average projected 2.1 Mt/a (10% over baseline) and B1's projected 2.5 Mt/a (13% over baseline). Though upstream of the coastal mountains, B1's projected yield is typically smallest, it likely simulates more sediment transport from the basin than A1B because of its yield during Jul-Sep when it produces more coastal mountain sediment than A1B or A2 (Table 4.3). Scenario B1 projected the overall mildest increase in generated sediment (46 Mt, 35% over baseline) while scenario A2 projects the largest increase (59 Mt, 45% over baseline). Roughly 90% of this intensification in production occurs within the Rocky and coastal mountains. All future simulations project the role of the coastal mountains in sediment generation to diminish in every season of the year, while the Rocky Mountains are expected to contribute a larger percentage of basin-wide generated sediment in each season.

Sub-basins connected to the coastal or Rocky mountains with a down-

stream lake act as sinks within the basin. At the end of 2094, the Harrison and Thompson sub-basins had retained 38% and 20% of the mud generated within the basin since 1965. The Nechako sub-basin, which is dammed at its outlet, does not contribute or store significant amounts of the FRB's sediment, but it does retain over 99% of the sediment it generates.

In the future period, the timing of FRB's sediment generation and yield is generally expected to shift to earlier in the year and be distributed relatively more evenly throughout the year with ensemble averages projecting the standard deviation of the seasonal fractions of annual sediment production to reduce from 22.5% at baseline to between 18.3% (A1) and 18.9% (A1B and B1) in the future period. In all scenarios, spring and centroid yield occur significantly earlier in the year while persistence of yield is longer.

The overall increase in sediment yield and generation, particularly from August to April, may have significant effects on the FRB's aquatic biota. Sockeye salmon, an important industrial and cultural fish in British Columbia, spawn in the Fraser River between August to January depending on the stock (*Pauley et al.* [1989]) and emerge as free swimming fry in April or May depending on water temperature (*Reiser and Bjornn* [1979]). These salmonids can be negatively affected by suspended and deposited fine sediment due to reduced oxygen, reduced feeding, and clogging of fish gills (*Huang and García* [2000]; *Pauley et al.* [1989]). In the past, the period of the year between sockeye spawning and becoming fry had relatively little sediment production and yield in the FRB; however, future scenarios project increases in production and yield during this period when the salmon are most affected.

While coastal retreat and relative sea level rise are important issues in the delta region of the FRB where 60% of the B.C. population resides, proper simulation of these effects requires more detail than our model provides. Our simulations, which stop at Mission, upstream of the delta, are coarse in scale and meant to provide sediment load estimates where tidal influences and anthropogenic effects are minimal. The delta region of the FRB is influenced by tides, has productive farmland and industry, contains some of the largest cities in the province, including Vancouver, and has a population of over 2.8 million people; it has seen considerable urbanization and land use change. Additionally, *Amos et al.* [1997] found that properties such as wet bulk density, which we roughly estimate for the basin, are important in the fine-grain stability of the delta. Still, we estimate that the projected increase in sediment yield at Mission (Table 4.4) is unlikely to significantly counteract the effects of sea-level rise. Even if all of the additional sediment transported through Mission were retained in the delta, the net accretion

would be < 0.1 mm/a, while *Mazzotti et al.* [2009] reports subsidence rates of 3-8 mm/a in some areas of the delta where anthropogenic effects are large and *IPCC* [2014] projects global sea-level rise rates of 8-16 mm/a by the end of the century.

Several caveats regarding the conclusions of this work must be discussed. Though urban and agricultural land make up only a small portion of the simulated basin and are not expected to grow significantly in the future, our model does not explicitly account for these land types. We have assumed several variables such as the reservoir dimensions and hysteresis parameter have maintained the same relationships with water flux throughout the simulation period. We have assumed that soil type and topography have remained stationary, and that the only significant source of hillslope generated sediment is from overland flow. While in reality many of these relationships and variables may change over time, we consider accounting for these temporal changes outside of the scope of our work. We have used results from CMIP3 GCMs rather than from CMIP5 which use the updated RCP scenarios. A study comparing CMIP3 simulations to those of CMIP5 in the Pacific Northwest showed generally warmer temperatures in RCP4.5 and RCP8.5 relative to B1 and A2, respectively (most of which can be explained by increased forcing in the newer scenarios) and no discernible differences in precipitation between the newer and older scenarios (*CIRC* [2013]). Warmer simulated temperatures may amplify the earlier snowmelt seen in the basin and lead to earlier spring and centroid yields than those projected by our simulation. However, because in most of our analysis model variability was higher than the variability amongst scenarios, it is likely that our range of projections would cover the majority of projections produced using the CMIP5 models with the RCP scenarios. CMIP5-based projections expected to be outside our CMIP3-based range come from RCP8.5 which has larger forcing than any of the SRES scenarios modelled in our study.

Because we use the results of the modelling performed in *Shrestha et al.* [2012], we also carry their assumptions, as well as those of the GCMs into our own results; in particular, we assume that vegetation and land surface remain unchanged throughout the simulation period. In reality, a range of changes to vegetation are possible. *Carroll et al.* [2006] found that the area within the FRB where mountain pine beetles (MPB) can survive is likely to expand, particularly in the interior plateau, due to climate change. The MPB has a history of infesting and killing trees within the FRB and may influence sediment dynamics directly by generating more hillslope erosion through detachment by rainfall or indirectly be changing the flow regime within the basin. *Schnorbus et al.* [2010] concluded that flow regimes in

alpine and sub-alpine regions, where most of the sediment within the FRB is generated, have low sensitivity to these forest disturbances. Therefore flow regime changes caused by the MPB are only likely to influence sediment dynamics in infested regions disconnected from the coastal and Rocky mountains such as Stuart and Nechako.

Direct influences of the MPB on sediment processes are expected to be mitigated within the interior plateau by the understorey left after an infestation. This growth is still likely to act as a rainfall intercept (*Schmid et al.* [1991]), reducing the possibility that an infestation would cause rainfall detachment within the interior plateau to become significant relative to generation by overland flow in the mountainous regions. There is a possibility that MPB infestation may lead to clear-cutting as a means of salvage harvesting or that an increase in the FRB's already active logging industry results in widespread future clear-cutting irrespective of any MPB infestation. In either case, harvesting would result in the removal of any understorey and affected interior plateau regions where sediment is not controlled by alpine or sub-alpine sediment (such as Stuart and Nechako) may see sediment yield and hillslope generation larger than our projections. To affect other regions of the FRB, the clear-cutting would need to be widespread enough that sediment generation within the interior plateau is on the order of generation within the mountainous regions of the basin.

Another possible change in vegetation is the migration of vegetation towards higher elevations due to warmer temperatures (*Malcolm et al.* [2002]). Vegetation can delay snowmelt by acting as a solar-radiation shield (*Boon* [2009]) and resist hillslope erosion and increase slope stability (*Sidle* [1980]). In the event of vegetation migration in the Rocky and coastal mountains, we expect the sediment yield, hillslope generation, and the change in the spring timing of sediment to be reduced relative to our model projections.

In river systems such as Asia's Huang He (Yellow), Mekong, and Yangtze, the impacts of climate change on sediment dynamics have been studied alongside significant anthropogenic influences such as dam construction and vegetative restoration (*Wang et al.* [2007]; *Yang et al.* [2015]; *Manh et al.* [2015]). In these systems, sediment erosion, deposition, and transport play a key role in agriculture and aquaculture as well as in the recession/advance of vital wetlands and delta regions. While *Manh et al.* [2015] found anthropogenic influences to significantly outweigh changes in climate within the Mekong system, *Wang et al.* [2007] and *Yang et al.* [2015] found both anthropogenic influences and decreases in precipitation play an important role in the changes of sediment yield in the Huang He and Yangtze systems. Most of the studies in these regions rely on observations or regression

analysis for estimates of sediment yields. *Manh et al.* [2015] noted that despite the importance of upstream sediment estimates in evaluating Mekong delta dynamics, no catchment model simulating sediment dynamics in the Mekong basin exists. Distributed, mechanistic models like the one used in this study, hold the potential to be adapted for such a purpose. While the basin in our study did not see significant anthropogenic effects, it is possible to make alterations to the model's hillslope generation and trapping mechanisms in order to adapt it to these sites. With such an adapted model, one could make valuable predictions of spatial and temporal changes in sediment dynamics under varying climate and land use scenarios in these and other regions.

Chapter 5

Conclusions

5.1 Overview

In this study, the model presented in *Patil et al.* [2012] was upscaled for application to large basins by adapting several of the model's governing equations and making use of sub-grid data to characterize hillslope, river direction and slope, and soil texture. The resulting distributed, mechanistic sediment transport model is capable of simulating large-scale sediment dynamics and is a unique tool in the study of basin-wide sediment processes. The transport model was applied to the FRB using historical inputs from VIC simulations provided by PCIC and produced simulated loads that matched available observations with relatively high R^2, NSE, and PBIAS values (Table 3.6). When given VIC outputs derived from climate scenarios (performed in *Shrestha et al.* [2012], provided by PCIC) as inputs, the sediment model projected a number of substantive changes to the erosion, deposition, and transport dynamics of the FRB.

When compared to the historical baseline (1965-1994), the future period (2065-2094) is generally expected to produce sediment hydrographs with earlier spring and centroid timing, later persistence timing, increased annual yield, and increased inter-annual variability in peak monthly sediment loads. These projections are consistent with the earlier snowmelt and corresponding stream flow expected in the mountainous regions of western North America under climate scenarios (*Stewart* [2009]). In sub-basins with relatively little influence from the coastal or Rocky mountains, significant changes in sediment timing properties and yield are usually predictable by changes in analogous water flux properties (for example Chilcotin, Table 4.7). In these basins, sediment transport appears to be fluvially controlled. On the other hand, sub-basins heavily influenced by the Rocky Mountains have changes in sediment timing and yield properties that are not significantly correlated to those of water flux (for example Hansard, Table 4.5). In these basins, changes in sediment transport is likely to be supply controlled.

Annual hillslope generation of fine sediment within the basin is projected to increase in the future period with the largest increases occurring in the

coastal and Rocky mountains. Seasonally, hillslope generation in the coastal and Rocky mountains is expected to increase during Oct-Jun and decrease in the coastal mountains Jul-Sep. The Rocky Mountains showed no significant change in hillslope generation during Jul-Sep. The relative role of the Rocky Mountains in the FRB's hillslope generation is expected to grow while the role of the coastal mountains is projected to diminish. Both the coastal and Rocky mountains contain sub-basins that act as significant sediment sinks for the FRB. The Harrison and Thompson sub-basins (part of the coastal and Rocky mountains, respectively) produce 30-40% and 15-25% of the FRB's annual hillslope mud, respectively and each retains over 95% of the hillslope mud generated within them due to the presence of a large lake upstream of their outlet.

5.2 Implications

Changes in the sediment dynamics of the FRB associated with climate change may have a number of important consequences for the habitat, biota, and humans within the basin. While sediment yield into the FRB's delta is projected to increase, this increase is expected to be minimal (<0.1 mm/a) relative to rates of local subsidence due to anthropogenic effects (3-8 mm/a, *Mazzotti et al.* [2009]), observed rates of 20th century sea-level rise (1.7-1.8 mm/a, *Mazzotti et al.* [2009]), and projected rates of 21st century global sea-level rise (8-16 mm/a by the end of the century, *IPCC* [2014]). Thus, shoreline retreat under the modelled scenarios is expected to continue through the end of the century in the FRB's delta, an area with a population of 2.8 million people and active farmland and industry.

The increase in year to year variability of peak monthly loads and the changes in the timing and shape of the sediment hydrograph are also of concern to biota in the river system. Increased variability in the peak monthly loads may lead to a higher frequency of sediment loads beyond the tolerable thresholds of biota (*Kerr* [1995]). For the sockeye salmon, which is already expected to be vulnerable to the warmer river temperatures in the FRB associated with climate change (*McDaniels et al.* [2010]), increased sediment loads from August through April correspond with the timing of spawning (*Pauley et al.* [1989]) and emergence as free-swimming fry (*Reiser and Bjornn* [1979]). Increase in fine suspended and deposited sediment during this time in a salmon's life cycle can have negative effects on the salmonid due to de-oxygenation, gill clogging, and reduced feeding (*Huang and García* [2000], *Pauley et al.* [1989]). Negative impacts on sockeye salmon popula-

tions in the FRB propagate to impacts on B.C.'s fishing industry for which the sockeye salmon is the most economically valuable fish (*Williams* [2007]), as well as aboriginal communities for whom the sockeye salmon is valuable both as food and for cultural purposes (*Jones et al.* [2004]).

5.3 Strengths and Limitations

To the author's knowledge, this is the first study to use a physically-based transport model to project the distributed sediment dynamics of a large basin under climate change scenarios. Studies such as *Smith et al.* [2011] and *Pelletier* [2012] have argued that, because of the localized nature of sediment sinks and sources, spatially distributed models are essential to properly capture basin-wide sediment dynamics. The model in this study does indeed identify a number of local sinks (such as the lakes near the Harrison and Thompson outlets) and sources (regions of the coastal and Rocky mountains) that are significant for basin-wide sediment yields. Physically-based, distributed models are also best suited to study the impacts of climate change on erosion, deposition, and transport of sediment (*Bathurst* [2010]). Empirical models and linear regression techniques for sediment estimates are generally limited in their ability to forecast sediment dynamics far into the future because they rely on the temporal stationarity of the relationship between sediment yield and flux. In our study, changes in sediment timing and yield properties at several sub-basins were not found to be significantly correlated to changes in water flux. At these stations, empirical models would not predict such changes. Because the model in this study is governed by physical force and mass-balance equations its fundamental relationships are not expected to change over time.

The mechanistic nature of the adapted transport model not only allows for simulation of sediment dynamics in future scenarios, but also in land use scenarios and other study sites. In principle, any change in FRB land use that can be entirely expressed for sediment purposes as changes in hydrology (i.e. dominant mechanisms for sediment erosion, deposition, and transport remain unchanged) can be studied with the model used in this study. For example, in *Schnorbus et al.* [2010], the authors performed VIC simulations of the FRB under a number of land use scenarios involving the MPB infestation. Provided these scenarios do not change the fundamental mechanisms of sediment dynamics in the FRB, the transport model can be directly applied to study any effects of changes to the flow regime on sediment processes, thereby confirming or refuting this study's claims that such effects are likely

minimal outside of regions within the interior plateau. Other large-scale sites can be simulated with the adapted transport model by making site-specific adaptations, such as changes to hillslope erosion computations in basins where detachment by rainfall is significant. In *Motew et al.* [2017], the authors used a version of the model from this thesis to study phosphorus transport through parts of the Mississippi watershed. The sediment model's mechanistic nature makes it flexible and allows it to be used for a variety of studies in a number of different regions.

In addition to the strengths in the sediment model, my methodology also makes use of an ensemble of GCMs and statistical tests to check the significance of projected changes in sediment properties. Studies such as *Kay et al.* [2009], *Prudhomme and Davies* [2009a], *Prudhomme and Davies* [2009b], and *Najafi et al.* [2011] found that GCM structure was the largest source of uncertainty in assessing hydrological impacts. Because *Shrestha et al.* [2012] used an ensemble of GCMs to create their VIC outputs, this study had a corresponding ensemble of inputs available for the sediment model that created a range of possible sediment dynamics for each climate scenario. Making use of the ensemble range allowed me to control for outlying behavior in individual model results and check the significance of changes in dynamics between the baseline and future periods relative to the variability amongst models.

While my methodology had a number of strengths, several limitations must be discussed. At the heart of many of these limitations are the questions of what is expected to remain stationary throughout the simulation period, what is expected to change, and how do these changes affect the projected results. As previously discussed, by simulating future dynamics with a model that was developed using historical data, I have implicitly assumed that all relationships and properties that are not modelled as a function of time will remain unchanged throughout the simulation period. These include hydrometric relationships with water flux, hysteresis parameters, gravel-bed sediment distributions, soil texture, and topography. I also assume that the dominant mechanism for hillslope mud generation will continue to be shear stress from overland flow. Additionally, this study carries all the assumptions of the models used as inputs to the sediment model; specifically the assumptions of *Shrestha et al.* [2012] that vegetation and land use are unchanged. While the likelihood/significance of some of these assumptions (such as vegetation and hillslope sediment sources) have been addressed in previous chapters, much of the discussion around them remains speculative. If one or a number of these properties change significantly in the future, my projections may prove skewed in unexpected ways. Results

from this study should be interpreted with these limitations in mind. In other study sites, such as those that have been heavily dammed or urbanized, some of these assumptions are likely to be false. In these locations, appropriate adaptations to the model are feasible (for instance, THMB has a built-in ability to model dams), but must be implemented prior to any simulations.

Chapter 4 employed output from older CMIP3 GCMs run with the SRES scenario suite rather than the more recent CMIP5 models and RCP scenarios described in the Fifth IPCC Assessment. This was necessary due to the availability VIC outputs under SRES scenarios and not the updated RCPs. Comparison of the CMIP3 and CMIP5 outputs within the FRB shows an agreement between the two ensembles regarding streamflow estimates and the qualitative responses of stream flow to snowmelt within the basin (*Schnorbus and Cannon* [2014]). Additionally, because inter-model variability was generally found to be higher than the variability of ensemble means amongst scenarios, simulations of this study likely model most of the range of possible outcomes of the new RCP scenarios; however, there are still likely gaps, particularly regarding the high end emission scenarios such as RCP8.5 which has larger forcings than the highest SRES scenario simulated in this study (A2).

5.4 Future Work

In future studies, the sediment model can be expanded by adding a bedload component. Combining a bedload routine with the suspended sediment transport model would allow the paired model to simulate changes in the bed distribution. With reasonable initial conditions, this would allow for the removal of the assumptions on bed distribution to which the model was found to be highly sensitive (Table 3.7). It also allows the model to directly calculate median grain size rather than relying on a bank-full shear stress equation (Equation (3.6)). Furthermore, simulating the bed distribution would allow us to express critical channel shear stress in terms of sand and mud content rather than using calibrated parameters.

There is also an opportunity to generalize the model to make it applicable to other study sites, particularly those with significant anthropogenic influences. Asian river systems such as the Yangtze, Huang He (Yellow), and Mekong have been subjected to large-scale damming. In these systems where agriculture, aquaculture, and coastal zones are vitally important, studies have found damming to significantly affect sediment yield (*Wang*

et al. [2007]; *Yang et al.* [2015]; *Manh et al.* [2015]). In *Wang et al.* [2007] and *Yang et al.* [2015], climate change was also found to influence sediment transport in the Huang He and Yangtze basins, respectively. While sediment dynamics in these basins play an important role in downstream deltas, agriculture, and aquaculture, to date, studies have mostly relied on observations and linear regression to make sediment yield analysis. As *Manh et al.* [2015] noted, no catchment-scale sediment model is available for use in the Mekong system. Evolving the adapted sediment transport model for use on these sites would not only make the model more generalized, it may also contribute key insights into the possible effects of damming and climate change on these systems. To adapt the sediment model for these river systems, the role of vegetation, the mechanism of hillslope sediment generation, and the conceptualization of sediment transport through lakes and dams all may need to be modified. However, the large number of spatially distributed observations in these systems make them well-suited for such work.

In addition to evolving the model for use at other sites, there are opportunities for continued study within the FRB. As stated previously, the availability of VIC output under various land use scenarios involving the MPB make studying the effects on sediment dynamics related to changes in flow regime caused by infestation and salvage harvesting straightforward. PCIC is also currently working on modelling the hydrology of the FRB using CMIP5 models under the updated RCP climate scenarios. When these results are made available, it is possible to update the sediment projections given in this thesis.

Bibliography

Abad, J. D., and M. H. García (2006), Discussion of efficient algorithm for computing Einstein integrals, *Journal of Hydraulic Engineering*, *132*(3), 332–334, doi:10.1061/(ASCE)0733-9429(2006)132:3(332).

Abad, J. D., G. C. Buscaglia, and M. H. García (2008), 2D stream hydrodynamic, sediment transport and bed morphology model for engineering applications, *Hydrological Processes*, *22*(10), 1443–1459, doi: 10.1002/hyp.6697.

Amos, C., T. Feeney, T. Sutherland, and J. Luternauer (1997), The stability of fine-grained sediments from the Fraser River Delta, *Estuarine, Coastal and Shelf Science*, *45*(4), 507–524, doi:https://doi.org/10.1006/ecss.1996.0193.

Arnold, J. G., and N. Fohrer (2005), SWAT2000: Current capabilities and research opportunities in applied watershed modelling, *Hydrological Processes*, *19*(3), 563–572, doi:10.1002/hyp.5611.

Arnold, J. G., R. Srinivasan, R. S. Muttiah, and J. R. Williams (1998), Large area hydrologic modeling and assessment Part I: Model development, *Journal of the American Water Resources Association*, *34*(1), 73–89, doi:10.1111/j.1752-1688.1998.tb05961.x.

Arora, V. K., and G. J. Boer (1999), A variable velocity flow routing algorithm for GCMs, *Journal of Geophysical Research: Atmospheres*, *104*(D24), 30,965–30,979, doi:10.1029/1999JD900905.

Asselman, N. E. M., H. Middelkoop, and P. M. van Dijk (2003), The impact of changes in climate and land use on soil erosion, transport and deposition of suspended sediment in the River Rhine, *Hydrological Processes*, *17*(16), 3225–3244, doi:10.1002/hyp.1384.

Attard, M. E., J. G. Venditti, and M. Church (2014), Suspended sediment transport in Fraser River at Mission, British Columbia: New observations and comparison to historical records, *Canadian Water Resources*

Journal / Revue canadienne des ressources hydriques, *39*(3), 356–371, doi:10.1080/07011784.2014.942105.

Bathurst, J. C. (2010), Predicting impacts of land use and climate change on erosion and sediment yield in river basins using SHETRAN, in *Handbook of Erosion Modelling*, edited by R. P. C. Morgan and M. A. Nearing, pp. 263–288, John Wiley & Sons, Ltd, doi:10.1002/9781444328455.ch14.

Beasley, D., L. F. Huggins, and E. J. Monke (1980), ANSWERS: A model for watershed planning., *Transactions of the ASAE*, *23*(4), 938–944.

Bennett, E. M., and M. E. Schipanski (2013), The phosphorus cycle, in *Fundamentals of Ecosystem Science*, edited by K. C. Weathers, D. L. Strayer, and G. E. Likens, pp. 159–178, Academic Press, Waltham, MA, doi:10.1016/B978-0-08-091680-4.00008-1.

Beven, K. (2006), A manifesto for the equifinality thesis, *Journal of Hydrology*, *320*, 18–36.

Boon, S. (2009), Snow ablation energy balance in a dead forest stand, *Hydrological Processes*, *23*(18), 2600–2610, doi:10.1002/hyp.7246.

Boyer, D., D. Curtis, D. Fisher, P. Jordan, D. Gillespie, R. Mohrmann, and N. Peters (2013), *Review of landslide management in British Columbia*, Ministry of Forests, Lands and Natural Resource Operations, Province of British Columbia.

Buffington, J. M., and D. R. Montgomery (1999a), Effects of hydraulic roughness on surface textures of gravel-bed rivers, *Water Resources Research*, *35*(11), 3507–3521, doi:10.1029/1999WR900138.

Buffington, J. M., and D. R. Montgomery (1999b), Effects of sediment supply on surface textures of gravel-bed rivers, *Water Resources Research*, *35*(11), 3523–3530, doi:10.1029/1999WR900232.

Canadian Forest Service (2016), Canadian national fire database – agency fire data, Natural Resources of Canada, Canadian Forest Service, Northern Forestry Centre, Edmonton, Alberta.

Canadian Heritage Rivers Systems. (2015). Website: http://www.chrs.ca/Rivers/Fraser/Fraser-F_e.php, Accessed 30 July 2015.

Carroll, A. L., J. Régnière, J. A. Logan, S. W. Taylor, B. Bentz, and J. A. Powell (2006), Impacts of climate change on range expansion by the mountain pine beetle initiative, *Working Paper 2006-14*, Canadian Forest Service, Victoria, B.C., 20 pp.

Church, M. (1990), Fraser River in central British Columbia, in *Surface Water Hydrology: The Geology of North America*, vol. O–1, edited by M. G. Wolman and H. C. Riggs, pp. 282–287, Geological Society of America, Boulder, Colorado, doi:10.1130/DNAG-GNA-O1.

Church, M., and O. Slaymaker (1989), Disequilibrium of Holocene sediment yield in glaciated British Columbia, *Nature*, *337*, 452–454, doi:10.1038/337452a0.

Church, M., R. Kellerhals, and T. J. Day (1989), Regional clastic sediment yield in British Columbia, *Canadian Journal of Earth Sciences*, *26*(1), 31–45, doi:10.1139/e89-004.

Climate Impacts Research Consortium (CIRC). (2013). Comparing CMIP5 and CMIP3 for the Pacific Northwest. U.S. Department of the Interior, U.S. Geological Survey.

Coe, M. T. (2000), Modeling terrestrial hydrological systems at the continental scale: Testing the accuracy of an atmospheric GCM, *Journal of Climate*, *13*(4), 686–704, doi:10.1175/1520-0442(2000)013⟨0686:MTHSAT⟩2.0.CO;2.

Coe, M. T., M. H. Costa, and E. A. Howard (2008), Simulating the surface waters of the Amazon River basin: impacts of new river geomorphic and flow parameterizations, *Hydrological Processes*, *22*(14), 2542–2553, doi:10.1002/hyp.6850.

Collins, A. L., and D. E. Walling (2004), Documenting catchment suspended sediment sources: Problems, approaches and prospects, *Progress in Physical Geography*, *28*(2), 159–196, doi:10.1191/0309133304pp409ra.

Collins, M., S. F. B. Tett, and C. Cooper (2001), The internal climate variability of HadCM3, a version of the Hadley Centre coupled model without flux adjustments, *Climate Dynamics*, *17*(1), 61–81, doi:10.1007/s003820000094.

Collins, W. D., C. M. Bitz, M. L. Blackmon, G. B. Bonan, C. S. Bretherton, J. A. Carton, P. Chang, S. C. Doney, J. J. Hack, T. B. Henderson, J. T.

Kiehl, W. G. Large, D. S. McKenna, B. D. Santer, and R. D. Smith (2006), The Community Climate System Model version 3 (CCSM3), *Journal of Climate*, *19*(11), 2122–2143, doi:10.1175/JCLI3761.1.

Daly, C., R. P. Neilson, and D. L. Phillips (1994), A statistical-topographic model for mapping climatological precipitation over mountainous terrain, *Journal of Applied Meteorology*, *33*(2), 140–158, doi:10.1175/1520-0450(1994)033⟨0140:ASTMFM⟩2.0.CO;2.

Danielson, J. J., and D. B. Gesch (2011), Global multi-resolution terrain elevation data 2010 (GMTED2010), *Open-File Report 2011–1073*, US Geological Survey, Reston, Virginia.

Delworth, T. L., A. J. Broccoli, A. Rosati, R. J. Stouffer, V. Balaji, J. A. Beesley, W. F. Cooke, K. W. Dixon, J. Dunne, K. A. Dunne, J. W. Durachta, K. L. Findell, P. Ginoux, A. Gnanadesikan, C. T. Gordon, S. M. Griffies, R. Gudgel, M. J. Harrison, I. M. Held, R. S. Hemler, L. W. Horowitz, S. A. Klein, T. R. Knutson, P. J. Kushner, A. R. Langenhorst, H.-C. Lee, S.-J. Lin, J. Lu, S. L. Malyshev, P. C. D. Milly, V. Ramaswamy, J. Russell, M. D. Schwarzkopf, E. Shevliakova, J. J. Sirutis, M. J. Spelman, W. F. Stern, M. Winton, A. T. Wittenberg, B. Wyman, F. Zeng, and R. Zhang (2006), GFDL's CM2 global coupled climate models. Part I: Formulation and simulation characteristics, *Journal of Climate*, *19*(5), 643–674, doi:10.1175/JCLI3629.1.

Döll, P., and B. Lehner (2002), Validation of a new global 30-min drainage direction map, *Journal of Hydrology*, *258*(1), 214–231, doi:https://doi.org/10.1016/S0022-1694(01)00565-0.

Einstein, H. A. (1950), The bed-load function for sediment transportation in open channel flows, *Technical Bulletins 1026*, United States Department of Agriculture, Economic Research Service.

Elliott, A. H., F. Oehler, J. Schmidt, and J. C. Ekanayake (2012), Sediment modelling with fine temporal and spatial resolution for a hilly catchment, *Hydrological Processes*, *26*(24), 3645–3660, doi:10.1002/hyp.8445.

Engelund, F., and E. Hansen (1967), A monograph on sediment transport in alluvial streams, *Technical University of Denmark 0stervoldgade 10, Copenhagen K.*

Foley, J. A., I. C. Prentice, N. Ramankutty, S. Levis, D. Pollard, S. Sitch, and A. Haxeltine (1996), An integrated biosphere model of land surface

processes, terrestrial carbon balance, and vegetation dynamics, *Global Biogeochemical Cycles*, *10*(4), 603–628, doi:10.1029/96GB02692.

Gallagher, L., R. W. Macdonald, and D. W. Paton (2004), The historical record of metals in sediments from six lakes in the Fraser River Basin, British Columbia, *Water, Air, and Soil Pollution*, *152*(1), 257–278, doi: 10.1023/B:WATE.0000015349.25371.af.

García, M., and G. Parker (1991), Entrainment of bed sediment into suspension, *Journal of Hydraulic Engineering*, *117*, 414–435.

Gassman, P., M. Reyes, C. Green, and J. Arnold (2007), The Soil and Water Assessment Tool: Historical development, applications, and future research directions, *Transactions of the ASABE*, *50*, 1211–1250.

GETECH (1995), *Global DTM5*, Geophysical Exploration Technology (GETECH), University of Leeds, Leeds, UK.

Gilbert, R. (1970), Observations of lacustrine sedimentation at Lillooet Lake, British Columbia, Ph.D. thesis, Department of Geography, University of British Columbia, Vancouver, 193 pp.

Global Soil Data Task (2000), *Global Soil Data Products CD-ROM (IGBP-DIS)*, International Geosphere-Biosphere Programme, Data and Information System, Postdam, Germany. Available from Oak Ridge National Laboratory Distributed Active Archive Center, Oak Ridge, TN. http://www.daac.ornl.govhttp://www.daac.ornl.gov.

Gonzalez, P., R. P. Neilson, J. M. Lenihan, and R. J. Drapek (2010), Global patterns in the vulnerability of ecosystems to vegetation shifts due to climate change, *Global Ecology and Biogeography*, *19*(6), 755–768, doi: 10.1111/j.1466-8238.2010.00558.x.

Harden, J. W., J. M. Sharpe, W. J. Parton, D. S. Ojima, T. L. Fries, T. G. Huntington, and S. M. Dabney (1999), Dynamic replacement and loss of soil carbon on eroding cropland, *Global Biogeochemical Cycles*, *13*(4), 885–901, doi:10.1029/1999GB900061.

Hooke, R. L. (2000), On the history of human as geomorphic agents, *Geology*, *28*, 843–846, doi:10.1130/0091-7613(2000)28⟨843:OTHOHA⟩2.0.CO;2.

Hovius, N. (1998), Controls on sediment supply by large rivers, in *Relative Role of Eustasy, Climate, and Tectonism in Continental Rocks*, *Special*

publication / Society for Sedimentary Geology, vol. 59, edited by K. W. Shanley and P. J. McCabe, pp. 3 – 16, SEPM, Tulsa, Oklahoma.

Huang, X., and M. H. García (2000), Pollution of gravel spawning grounds by deposition of suspended sediment, *Journal of Environmental Engineering*, *126*(10), 963–967, doi:10.1061/(ASCE)0733-9372(2000)126:10(963).

Hwang, K. N. (1989), Erodibility of fine sediment in wave dominated environments, Master's thesis, University of Florida, Gainesville, 166 pp.

IPCC (2007), Climate change 2007: Synthesis report. Contribution of Working Groups I, II and III to the Fourth Assessment Report of the Intergovernmental Panel on Climate Change [core Writing Team, R. K. Pachauri and A. Reisinger (eds.)]. IPCC, Geneva, Switzerland, 104 pp.

IPCC (2014), Climate change 2014: Synthesis report. Contribution of Working Groups I, II and III to the Fifth Assessment Report of the Intergovernmental Panel on Climate Change [core Writing Team, R. K. Pachauri and L. A. Meyer (eds.)]. IPCC, Geneva, Switzerland, 151 pp.

Jakob, M., D. Anderson, T. Fuller, O. Hungr, and D. Ayotte (2011), An unusually large debris flow at Hummingbird Creek, Mara Lake, British Columbia, *Canadian Geotechnical Journal*, *37*, 1109–1125, doi:10.1139/cgj-37-5-1109.

Jones, R., M. Shepert, and N. Sterritt (2004), *Our place at the table: First Nations in the B.C. fishery*, First Nation Panel on Fisheries, Vancouver, B.C.

Jordan, O., Peter ; Slaymaker (1991), Holocene sediment production in Lillooet River Basin, British Colombia: A sediment budget approach, *Géographie physique et Quaternaire*, *45*(1), 45–57.

K-1 Model Developers (2004), K-1 coupled GCM (MIROC) description, *K-1 Technical Report 1*, K-1 Center for Climate System Research, University of Tokyo; National Institute for Environmental Studies (NIES), Frontier Research Center for Global Change (FRCGC).

Kay, A. L., H. N. Davies, V. A. Bell, and R. G. Jones (2009), Comparison of uncertainty sources for climate change impacts: Flood frequency in England, *Climatic Change*, *92*(1), 41–63, doi:10.1007/s10584-008-9471-4.

Kerr, S. J. (1995), Silt, turbidity and suspended sediments in the aquatic environment: An annotated bibliography and literature review, *Southern Region Science & Technology Transfer Unit Technical Report TR-008*, Ontario Ministry of Natural Resources, Ontario.

Kumarasamy, K., and P. Belmont (2017), Multiple domain evaluation of watershed hydrology models, *Hydrology and Earth System Sciences Discussions*, pp. 1–32.

Legates, D. R., and G. J. McCabe (1999), Evaluating the use of "goodness-of-fit" measures in hydrologic and hydroclimatic model validation, *Water Resources Research*, *35*(1), 233–241, doi:10.1029/1998WR900018.

Leong, D. N. S., and S. D. Donner (2015), Climate change impacts on streamflow availability for the Athabasca oil sands, *Climatic Change*, *133*(4), 651–663, doi:10.1007/s10584-015-1479-y.

Liang, X., D. P. Lettenmaier, E. F. Wood, and S. J. Burges (1994), A simple hydrologically based model of land surface water and energy fluxes for general circulation models, *Journal of Geophysical Research: Atmospheres*, *99*(D7), 14,415–14,428, doi:10.1029/94JD00483.

Liang, X., E. F. Wood, and D. P. Lettenmaier (1996), Surface soil moisture parameterization of the VIC-2L model: Evaluation and modification, *Global and Planetary Change*, *13*(1), 195–206, doi:https://doi.org/10.1016/0921-8181(95)00046-1.

Malcolm, J. R., A. Markham, R. P. Neilson, and M. Garaci (2002), Estimated migration rates under scenarios of global climate change, *Journal of Biogeography*, *29*(7), 835–849, doi:10.1046/j.1365-2699.2002.00702.x.

Manh, N. V., N. V. Dung, N. N. Hung, M. Kummu, B. Merz, and H. Apel (2015), Future sediment dynamics in the Mekong Delta floodplains: Impacts of hydropower development, climate change and sea level rise, *Global and Planetary Change*, *127*(Supplement C), 22–33, doi:https://doi.org/10.1016/j.gloplacha.2015.01.001.

Martin, G. M., M. A. Ringer, V. D. Pope, A. Jones, C. Dearden, and T. J. Hinton (2006), The physical properties of the atmosphere in the New Hadley Centre Global Environmental Model (HadGEM1). Part I: Model description and global climatology, *Journal of Climate*, *19*(7), 1274–1301, doi:10.1175/JCLI3636.1.

Mazzotti, S., A. Lambert, M. Van der Kooij, and A. Mainville (2009), Impact of anthropogenic subsidence on relative sea-level rise in the Fraser River delta, *Geology*, *37*, 771–774, doi:10.1130/G25640A.1.

McDaniels, T., S. Wilmot, M. Healey, and S. Hinch (2010), Vulnerability of Fraser River sockeye salmon to climate change: A life cycle perspective using expert judgments, *Journal of Environmental Management*, *91*(12), 2771 – 2780, doi:https://doi.org/10.1016/j.jenvman.2010.08.004.

McLean, D. G. (1990), Channel instability on lower Fraser River, Ph.D. thesis, Interdisciplinary Hydrology Program, University of British Columbia, Vancouver, 290 pp.

McLean, D. G., M. Church, and B. Tassone (1999), Sediment transport along lower Fraser River: 1. Measurements and hydraulic computations, *Water Resources Research*, *35*(8), 2533–2548, doi:10.1029/1999WR900101.

Meehl, G. A., C. Covey, K. E. Taylor, T. Delworth, R. J. Stouffer, M. Latif, B. McAvaney, and J. F. B. Mitchell (2007), The WCRP CMIP3 multimodel dataset: A new era in climate change research, *Bulletin of the American Meteorological Society*, *88*(9), 1383–1394, doi: 10.1175/BAMS-88-9-1383.

Mitchener, H., and H. Torfs (1996), Erosion of mud/sand mixtures, *Coastal Engineering*, *29*(1), 1 – 25, doi:https://doi.org/10.1016/S0378-3839(96)00002-6.

Moore, R. D. (1991), Hydrology and water supply in the Fraser River Basin, in *Water in Sustainable Development: Exploring Our Common Future in the Fraser River Basin*, edited by A. H. J. Dorcey and J. R. Griggs, pp. 21–39, Westwater Research Centre, Vancouver, British Columbia.

Moriasi, D. N., J. G. Arnold, M. W. Van Liew, R. L. Bingner, R. D. Harmel, and T. L. Veith (2007), Model evaluation guidelines for systematic quantification of accuracy in watershed simulations, *Transactions of the ASABE*, *50*(3), 885–900, doi:10.13031/2013.23153.

Motew, M., X. Chen, E. G. Booth, S. R. Carpenter, P. Pinkas, S. C. Zipper, S. P. Loheide, S. D. Donner, K. Tsuruta, P. A. Vadas, and C. J. Kucharik (2017), The influence of legacy p on lake water quality in a midwestern agricultural watershed, *Ecosystems*, doi:10.1007/s10021-017-0125-0.

Najafi, M. R., H. Moradkhani, and I. W. Jung (2011), Assessing the uncertainties of hydrologic model selection in climate change impact studies, *Hydrological Processes*, *25*(18), 2814–2826, doi:10.1002/hyp.8043.

Nearing, M., G. Foster, L. Lane, and S. Finkner (1989), A process-based soil erosion model for USDA-Water Erosion Prediction Project technology, *Transactions of the ASAE*, *32*(5), 1587–1593, doi:10.13031/2013.31195.

Nistor, C. (1996), Temporal patterns in the normal-regime fine-sediment cascade in Russell Creek Basin, Vancouver Island, Ph.D. thesis, Department of Geography, University of British Columbia, Vancouver, 236 pp.

Nistor, C. J., and M. Church (2005), Suspended sediment transport regime in a debris-flow gully on Vancouver Island, British Columbia, *Hydrological Processes*, *19*(4), 861–885, doi:10.1002/hyp.5549.

Osterkamp, W. R., and T. J. Toy (1997), Geomorphic considerations for erosion prediction, *Environmental Geology*, *29*(3), 152–157, doi:10.1007/s002540050113.

Pacific Climate Impacts Consortium, University of Victoria. (2014). Gridded Hydrologic Model Output. Downloaded from http://tools.pacificclimate.org/dataportal/hydro_model_out/map/ on March 15, 2016.

Parker, G. (2008), Transport of gravel and sediment mixtures, in *Sedimentation Engineering*, edited by M. García, pp. 165–251, American Society of Civil Engineers, Reston, Virginia, doi:10.1061/9780784408148.ch03.

Parker, R. N., A. L. Densmore, N. J. Rosser, M. de Michele, Y. Li, R. Huang, S. Whadcoat, and D. N. Petley (2011), Mass wasting triggered by the 2008 Wenchuan earthquake is greater than orogenic growth, *Nature Geoscience*, *4*(7), 449–452, doi:10.1038/ngeo1154.

Patil, S., M. Sivapalan, M. A. Hassan, S. Ye, C. J. Harman, and X. Xu (2012), A network model for prediction and diagnosis of sediment dynamics at the watershed scale, *Journal of Geophysical Research: Earth Surface*, *117*(F4), n/a–n/a, doi:10.1029/2012JF002400, f00A04.

Pauley, G. B., R. Risher, and G. L. Thomas (1989), Species profiles: Life histories and environmental requirements of coastal fishes and invertebrates (Pacific Northwest)–sockeye salmon, *U.S. Fish and Wildlife Service Biological Report 82(11.116) TR EL-82-4*, U.S. Army Corps of Engineers, Seattle, WA.

Pearce, A. J., and A. J. Watson (1986), Effects of earthquake-induced landslides on sediment budget and transport over a 50-yr period, *Geology*, *14*(1), 52–55, doi:10.1130/0091-7613(1986)14\<52:EOELOS\>2.0.CO;2.

Pelletier, J. D. (2012), A spatially distributed model for the long-term suspended sediment discharge and delivery ratio of drainage basins, *Journal of Geophysical Research: Earth Surface*, *117*(F2), n/a–n/a, doi:10.1029/2011JF002129, f02028.

Praskievicz, S., and H. Chang (2011), Impacts of climate change and urban development on water resources in the Tualatin River Basin, Oregon, *Annals of the Association of American Geographers*, *101*(2), 249–271, doi:10.1080/00045608.2010.544934.

Prosser, I., I. Rutherfurd, J. Olley, W. Young, P. Wallbrink, and C. Moran (2001), Large-scale patterns of erosion and sediment transport in river networks, with examples from Australia, *Marine and Freshwater Research*, *52*, 81–99, doi:10.1071/MF00033_CO.

Prudhomme, C., and H. Davies (2009a), Assessing uncertainties in climate change impact analyses on the river flow regimes in the UK. Part 1: Baseline climate, *Climatic Change*, *93*(1), 177–195, doi:10.1007/s10584-008-9464-3.

Prudhomme, C., and H. Davies (2009b), Assessing uncertainties in climate change impact analyses on the river flow regimes in the UK. Part 2: Future climate, *Climatic Change*, *93*(1), 197–222, doi:10.1007/s10584-008-9461-6.

Reggiani, P., M. Sivapalan, S. M. Hassanizadeh, and W. G. Gray (2001), Coupled equations for mass and momentum balance in a stream network: Theoretical derivation and computational experiments, *Proceedings: Mathematical, Physical and Engineering Sciences*, *457*(2005), 157–189.

Reiser, D. W., and T. C. Bjornn (1979), Influence of forest and rangeland management on anadromous fish habitat in Western North America: habitat requirements of anadromous salmonids, *General Technical Report PNW-GTR-096*, U.S. Department of Agriculture, Forest Service, Pacific Northwest Reaserch Station, 1–54.

Reynoldson, T. B., J. Culp, R. Lowell, and J. S. Richardson (2005), Fraser River Basin, in *Rivers of North America*, edited by A. C. Benke and C. E. Cushing, pp. 696–732, Academic Press, Burlington, M. A., doi: https://doi.org/10.1016/B978-012088253-3/50018-3.

Roeckner, E., R. Brokopf, M. Esch, M. Giorgetta, S. Hagemann, L. Kornblueh, E. Manzini, U. Schlese, and U. Schulzweida (2006), Sensitivity of simulated climate to horizontal and vertical resolution in the ECHAM5 atmosphere model, *Journal of Climate*, *19*(16), 3771–3791, doi: 10.1175/JCLI3824.1.

Rotstayn, L. D., M. A. Collier, M. R. Dix, Y. Feng, H. B. Gordon, S. P. O'Farrell, I. N. Smith, and J. Syktus (2010), Improved simulation of Australian climate and ENSO-related rainfall variability in a global climate model with an interactive aerosol treatment, *International Journal of Climatology*, *30*(7), 1067–1088, doi:10.1002/joc.1952.

Scheurer, K., C. Alewell, D. Bänninger, and P. Burkhardt-Holm (2009), Climate and land-use changes affecting river sediment and brown trout in alpine countries—a review, *Environmental Science and Pollution Research*, *16*(2), 232–242, doi:10.1007/s11356-008-0075-3.

Schiefer, E. (1999), Natural patterns and land use impacts on lacustrine sedimentation patterns in northwestern British Columbia, Master's thesis, Department of Geography, University of British Columbia, Vancouver, 172 pp.

Schiefer, E., O. Slaymaker, and B. Klinkenberg (2001), Physiographically controlled allometry of specific sediment yield in the Canadian Cordillera: A lake sediment-based approach, *Geografiska Annaler: Series A, Physical Geography*, *83*(1-2), 55–65, doi:10.1111/j.0435-3676.2001.00144.x.

Schleiss, A. J., M. J. Franca, C. Juez, and G. D. Cesare (2016), Reservoir sedimentation, *Journal of Hydraulic Research*, *54*(6), 595–614, doi: 10.1080/00221686.2016.1225320.

Schmid, J. M., S. A. Mata, M. H. Martinez, and C. A. Troendle (1991), *Net precipitation within small group infestations of the mountain pine beetle*, vol. 508, USDA Forest Service, Rocky Mountain Forest and Range Experiment Station.

Schnorbus, M., K. Bennett, and A. Werner (2010), Quantifying the water resources impacts of the mountain pine beetle and associated salvage harvest operations across a range of watershed scales: Hydrologic modelling of the Fraser River Basin, *Information Report BC-X-423 MBP Project 7.29*, Natural Resources Canada, Canadian Forest Service, Pacific Forestry Centre, Victoria, B.C., 64 pp.

Schnorbus, M. A., and A. J. Cannon (2014), Statistical emulation of streamflow projections from a distributed hydrological model: Application to CMIP3 and CMIP5 climate projections for British Columbia, Canada, *Water Resources Research*, *50*(11), 8907–8926, doi:10.1002/2014WR015279.

Schnorbus, M. A., K. E. Bennett, A. T. Werner, and A. J. Berland (2011), *Hydrologic impacts of climate change in the Peace, Campbell and Columbia watersheds, British Columbia, Canada*, Pacific Climate Impacts Consortium, University of Victoria, Victoria, B.C.,157 pp.

Schumm, S. A. (1963), The disparity between present rates of denudation and orogeny, *U.S. Geological Survey Professional Paper*, *454-H*, 13 pp.

Scinocca, J. F., N. A. McFarlane, M. Lazare, J. Li, and D. Plummer (2008), Technical Note: The CCCma third generation AGCM and its extension into the middle atmosphere, *Atmospheric Chemistry and Physics*, *8*(23), 7055–7074, doi:10.5194/acp-8-7055-2008.

Shepard, D. S. (1984), Computer mapping: The SYMAP interpolation algorithm, in *Spatial Statistics and Models*, edited by G. L. Gaile and C. J. Willmott, pp. 133–145, Springer Netherlands, Dordrecht, doi:10.1007/978-94-017-3048-8_7.

Shrestha, R. R., M. A. Schnorbus, A. T. Werner, and A. J. Berland (2012), Modelling spatial and temporal variability of hydrologic impacts of climate change in the Fraser River basin, British Columbia, Canada, *Hydrological Processes*, *26*(12), 1840–1860, doi:10.1002/hyp.9283.

Sidle, R. C. (1980), Slope stability on forest land, *PNW 209*, Pacific Northwest Extension. United States Department of Agriculture, Forest Service.

Singh, V. P., and D. K. Frevert (2002), *Mathematical models of large watershed hydrology.*, Water Resources Publications, Colorado.

Slaymaker, O. (1977), Estimation of sediment yield in temperate alpine environments, *International Association of Hydrological Sciences*, (122), 109–117.

Slaymaker, O. (1993), The sediment budget of the Lillooet River Basin, British Columbia, *Physical Geography*, *14*(3), 304–320, doi:10.1080/02723646.1993.10642482.

Smith, R. E. (1981), A kinematic model for surface mine sediment yield, *Transactions of the ASAE*, *24*(6), 1508–1514, doi:10.13031/2013.34482.

Smith, S. M. C., P. Belmont, and P. R. Wilcock (2011), Closing the gap between watershed modeling, sediment budgeting, and stream restoration, in *Stream Restoration in Dynamic Fluvial Systems*, edited by S. J. Bennett and A. Simon, pp. 293–317, American Geophysical Union, doi:10.1029/2011GM001085.

Smith, V. H., S. B. Joye, and R. W. Howarth (2006), Eutrophication of freshwater and marine ecosystems, *Limnology and Oceanography*, *51*(1part2), 351–355, doi:10.4319/lo.2006.51.1_part_2.0351.

Srinivasan, R., and B. A. Engel (1994), A spatial decision support system for assessing agricultural nonpoint source pollution, *Journal of the American Water Resources Association*, *30*(3), 441–452, doi:10.1111/j.1752-1688.1994.tb03303.x.

Stallard, R. F. (1998), Terrestrial sedimentation and the carbon cycle: Coupling weathering and erosion to carbon burial, *Global Biogeochemical Cycles*, *12*(2), 231–257, doi:10.1029/98GB00741.

Sternecker, K., R. Wild, and J. Geist (2013), Effects of substratum restoration on salmonid habitat quality in a subalpine stream, *Environmental Biology of Fishes*, *96*(12), 1341–1351, doi:10.1007/s10641-013-0111-0.

Stewart, I. T. (2009), Changes in snowpack and snowmelt runoff for key mountain regions, *Hydrological Processes*, *23*(1), 78–94, doi:10.1002/hyp.7128.

Syvitski, J. P., S. D. Peckham, R. Hilberman, and T. Mulder (2003), Predicting the terrestrial flux of sediment to the global ocean: A planetary perspective, *Sedimentary Geology*, *162*(1), 5–24, doi:https://doi.org/10.1016/S0037-0738(03)00232-X.

Syvitski, J. P. M., and J. D. Milliman (2007), Geology, geography, and humans battle for dominance over the delivery of fluvial sediment to the coastal ocean, *Journal of Geology*, *115*, 1–19, doi:10.1086/509246.

Syvitski, J. P. M., C. J. Vörösmarty, A. J. Kettner, and P. Green (2005), Impact of humans on the flux of terrestrial sediment to the global coastal ocean, *Science*, *308*(5720), 376–380, doi:10.1126/science.1109454.

Tian, F. (2006), Study of Thermodynamic Watershed Hydrologic Model (THModel), Ph.D. thesis, Tsinghua University, Beijing, China, 168 pp.

Todini, E. (1996), The ARNO rainfall–runoff model, *Journal of Hydrology*, *175*(1), 339–382, doi:https://doi.org/10.1016/S0022-1694(96)80016-3.

Van Oost, K., T. Quine, G. Govers, S. De Gryze, J. Six, J. Harden, J. C Ritchie, G. W McCarty, G. Heckrath, C. Kosmas, J. Giraldez, J. Marques Da Silva, and R. Merckx (2007), The impact of agricultural soil erosion on the global carbon cycle, *Science*, *318*, 626–629, doi:10.1126/science.1145724.

Venditti, J. G., and M. Church (2014), Morphology and controls on the position of a gravel-sand transition: Fraser River, British Columbia, *Journal of Geophysical Research: Earth Surface*, *119*(9), 1959–1976, doi:10.1002/2014JF003147, 2014JF003147.

Walling, D. E. (2009), *The Impact of Global Change on Erosion and Sediment Transport by Rivers : Current Progress and Future Challenges*, Paris, France : Unesco.

Wang, H., Z. Yang, Y. Saito, J. P. Liu, X. Sun, and Y. Wang (2007), Stepwise decreases of the Huanghe (Yellow River) sediment load (1950–2005): Impacts of climate change and human activities, *Global and Planetary Change*, *57*(3), 331–354, doi:https://doi.org/10.1016/j.gloplacha.2007.01.003.

Wang, T., A. Hamann, D. L. Spittlehouse, and S. N. Aitken (2006), Development of scale-free climate data for Western Canada for use in resource management, *International Journal of Climatology*, *26*(3), 383–397, doi:10.1002/joc.1247.

Warrick, J., M. Madej, M. Goñi, and R. Wheatcroft (2013), Trends in the suspended-sediment yields of coastal rivers of northern California, 1955–2010, *Journal of Hydrology*, *489*(Supplement C), 108–123, doi:https://doi.org/10.1016/j.jhydrol.2013.02.041.

Warrick, J. A. (2014), Eel River margin source-to-sink sediment budgets: Revisited, *Marine Geology*, *351*(Supplement C), 25–37, doi:https://doi.org/10.1016/j.margeo.2014.03.008.

Warrick, J. A., and D. M. Rubin (2007), Suspended-sediment rating curve response to urbanization and wildfire, Santa Ana River, California, *Journal of Geophysical Research: Earth Surface*, *112*(F2), doi:10.1029/2006JF000662, f02018.

Warrick, J. A., J. A. Hatten, G. B. Pasternack, A. B. Gray, M. A. Goñi, and R. A. Wheatcroft (2012), The effects of wildfire on the sediment yield of a coastal California watershed, *Geological Society of America Bulletin*, *124*(7/8), 1130–1146, doi:10.1130/B30451.1.

Warrick, J. A., J. A. Bountry, A. E. East, C. S. Magirl, T. J. Randle, G. Gelfenbaum, A. C. Ritchie, G. R. Pess, V. Leung, and J. J. Duda (2015), Large-scale dam removal on the Elwha River, Washington, USA: Source-to-sink sediment budget and synthesis, *Geomorphology*, *246*, 729–750, doi:https://doi.org/10.1016/j.geomorph.2015.01.010.

Werner A. T. (2011), *BCSD downscaled transient climate projections for eight select GCMs over British Columbia, Canada*, Pacific Climate Impacts Consortium, University of Victoria, Victoria, B.C., 63 pp.

White, M., M. J, C. Santhi, N. Kannan, J. Arnold, D. Harmel, L. Norfleet, P. Allen, M. DiLuzio, X. Wang, J. Atwood, E. Haney, and M.-V. Johnson (2014), Nutrient delivery from the Mississippi River to the Gulf of Mexico and the effects of cropland conservation, *Journal of Soil and Water Conservation*, *69*, 26–40, doi:10.2489/jswc.69.1.26.

Whitehead, P. G., R. L. Wilby, R. W. Battarbee, M. Kernan, and A. J. Wade (2009), A review of the potential impacts of climate change on surface water quality, *Hydrological Sciences Journal*, *54*(1), 101–123, doi:10.1623/hysj.54.1.101.

Williams, A. (2007), The Pacific Salmon Treaty: A historical analysis and prescription for the future, *Journal of Environmental Law and Litigation*, *22*(1), 153–196.

Wood, A. W., L. R. Leung, V. Sridhar, and D. P. Lettenmaier (2004), Hydrologic implications of dynamical and statistical approaches to downscaling climate model outputs, *Climatic Change*, *62*(1), 189–216, doi:10.1023/B:CLIM.0000013685.99609.9e.

Wood, E. F., J. K. Roundy, T. J. Troy, L. P. H. van Beek, M. F. P. Bierkens, E. Blyth, A. de Roo, P. Döll, M. Ek, J. Famiglietti, D. Gochis, N. van de Giesen, P. Houser, P. R. Jaffé, S. Kollet, B. Lehner, D. P. Lettenmaier, C. Peters-Lidard, M. Sivapalan, J. Sheffield, A. Wade, and P. Whitehead (2011), Hyperresolution global land surface modeling: Meeting a grand challenge for monitoring Earth's terrestrial water, *Water Resources Research*, *47*(5), n/a–n/a, doi:10.1029/2010WR010090, w05301.

Wright, S., and G. Parker (2004), Flow resistance and suspended load in sand-bed rivers: Simplified stratification model, *Journal of Hydraulic Engineering*, *130*(8), 796–805, doi:10.1061/(ASCE)0733-9429(2004)130:8(796).

Wu, H., J. S. Kimball, N. Mantua, and J. Stanford (2011), Automated upscaling of river networks for macroscale hydrological modeling, *Water Resources Research*, *47*(3), n/a–n/a, doi:10.1029/2009WR008871, w03517.

Yang, S. L., K. H. Xu, J. D. Milliman, H. F. Yang, and C. S. Wu (2015), Decline of Yangtze River water and sediment discharge: Impact from natural and anthropogenic changes, *Scientific Reports*, *5*(12581), doi:10.1038/srep12581.

Yapo, P. O., H. V. Gupta, and S. Sorooshian (1998), Multi-objective global optimization for hydrologic models, *Journal of Hydrology*, *204*(1), 83–97, doi:https://doi.org/10.1016/S0022-1694(97)00107-8.

Young, A. (1969), Present rate of land erosion, *Nature*, *224*, 851–852, doi:10.1038/224851a0.

Appendix A

Hillslope Generation: Additional Maps

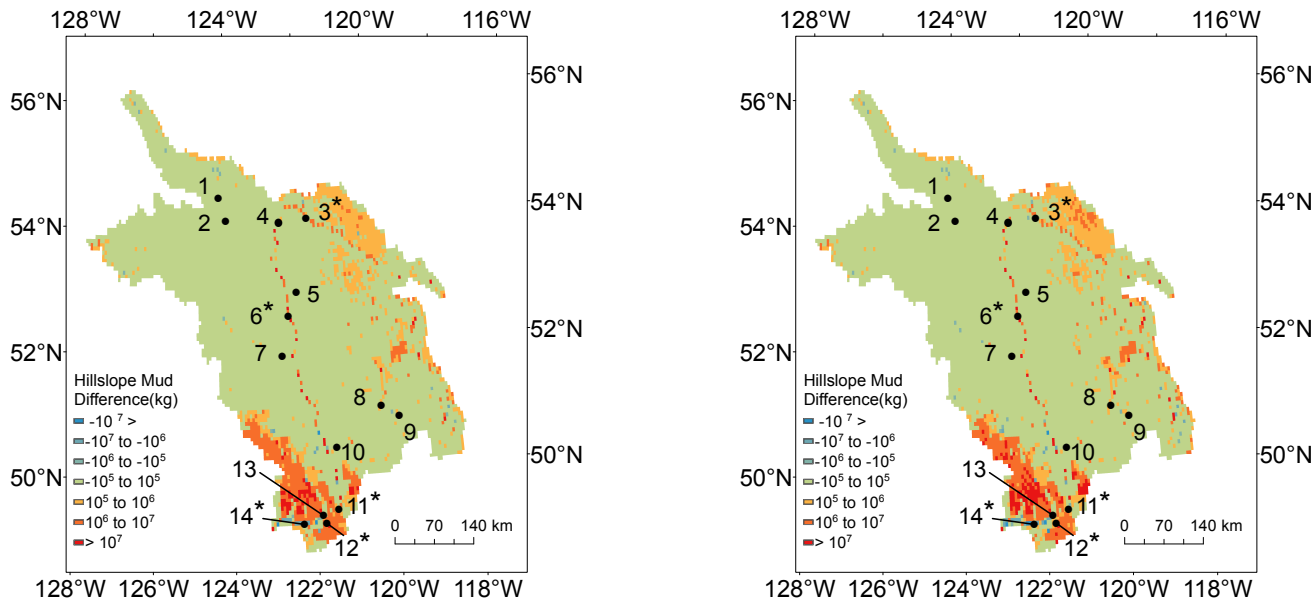

(a) B1 Jan-Mar generation differences

(b) A2 Jan-Mar generation differences

Figure A.1: Ensemble averaged difference in Jan-Mar hillslope mud generation between future and baseline periods for scenarios B1 (a) and A2 (b). Positive values indicate future values are larger than baseline values.

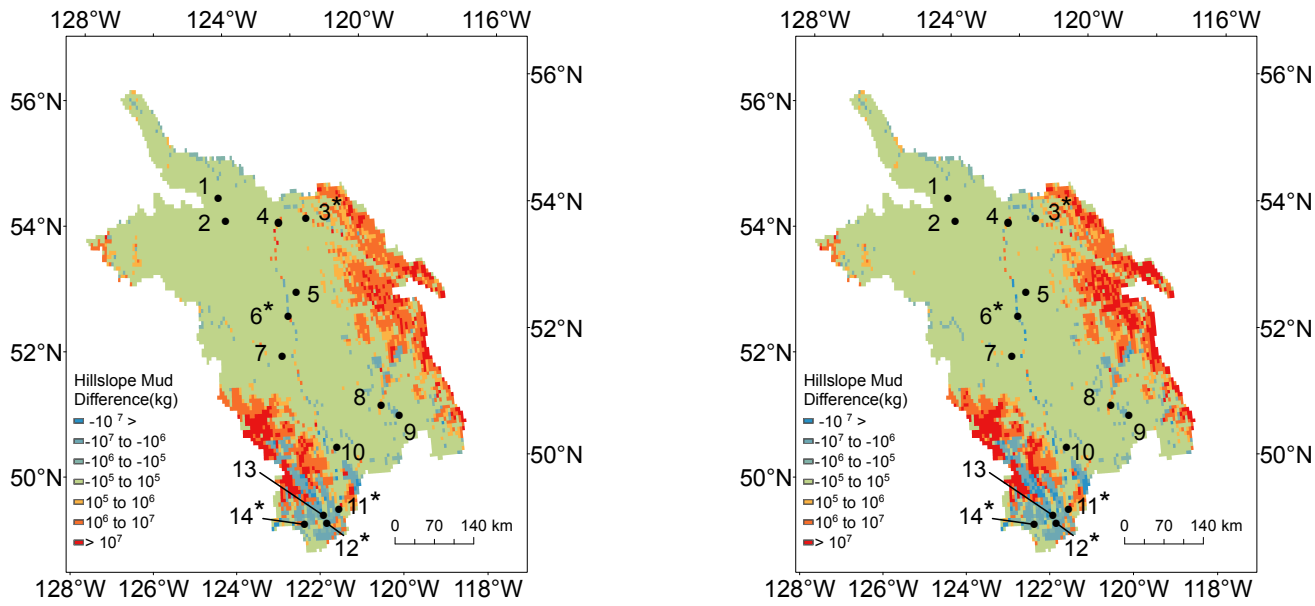

(a) B1 Apr-Jun generation differences

(b) A2 Apr-Jun generation differences

Figure A.2: Ensemble averaged difference in Apr-Jun hillslope mud generation between future and baseline periods for scenarios B1 (a) and A2 (b). Positive values indicate future values are larger than baseline values.

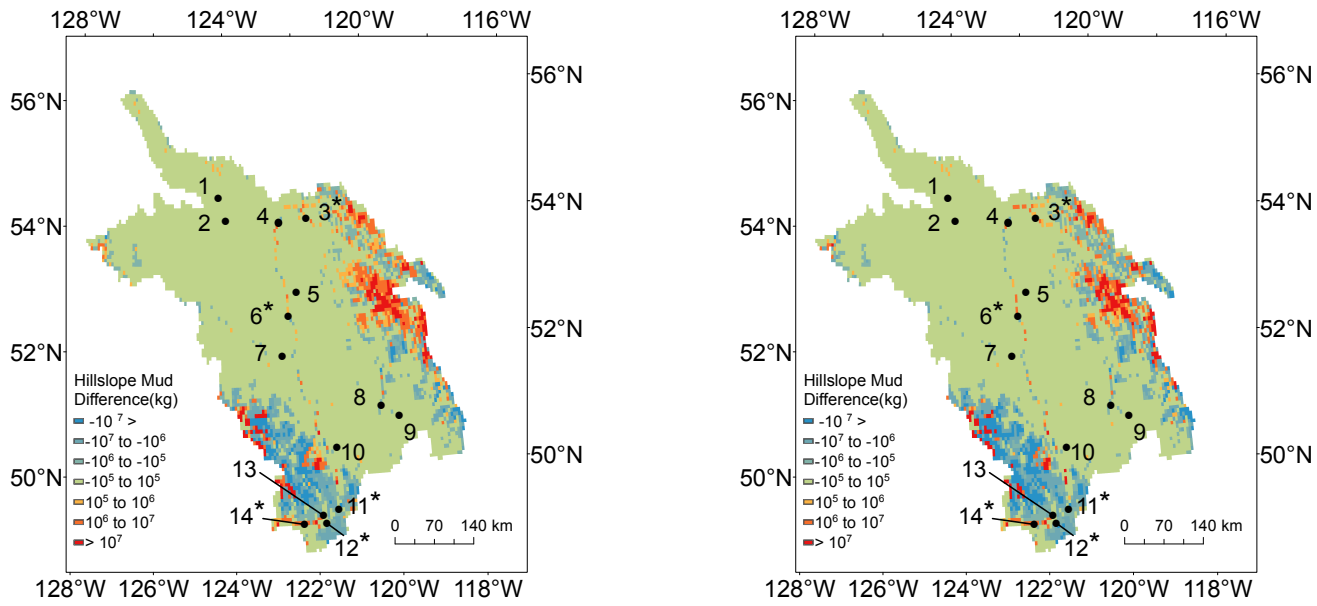

(a) B1 Jul-Sep generation differences

(b) A2 Jul-Sep generation differences

Figure A.3: Ensemble averaged difference in Jul-Sep hillslope mud generation between future and baseline periods for scenarios B1 (a) and A2 (b). Positive values indicate future values are larger than baseline values.

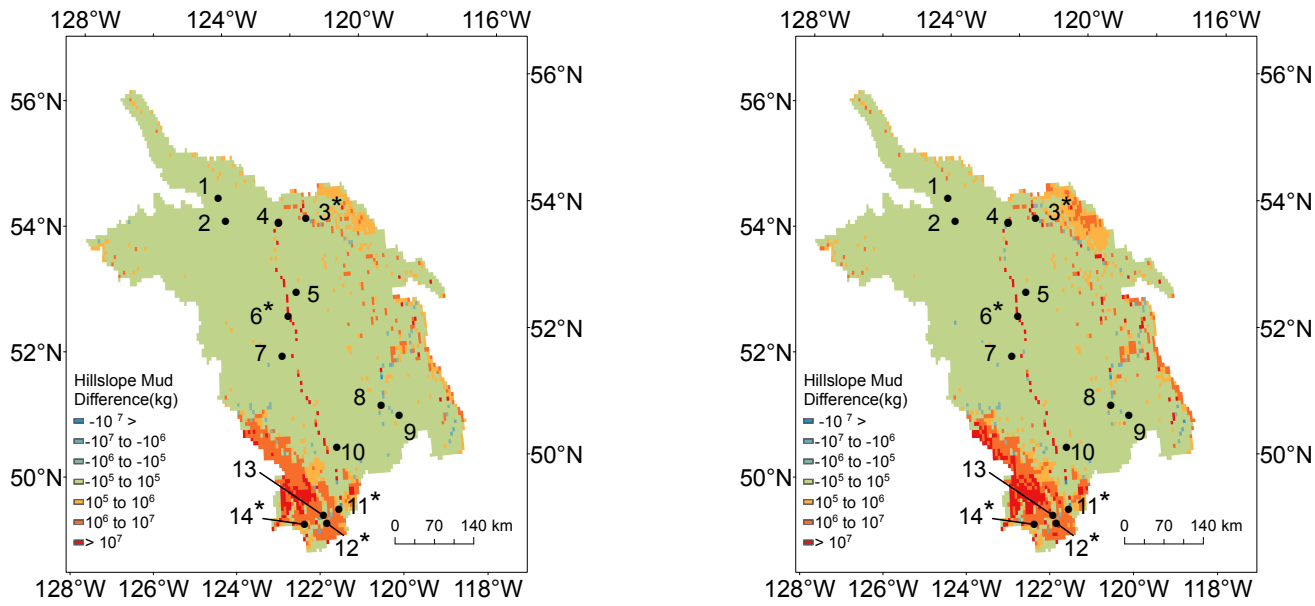

(a) B1 Oct-Dec generation differences

(b) A2 Oct-Dec generation differences

Figure A.4: Ensemble averaged difference in Oct-Dec hillslope mud generation between future and baseline periods for scenarios B1 (a) and A2 (b). Positive values indicate future values are larger than baseline values.

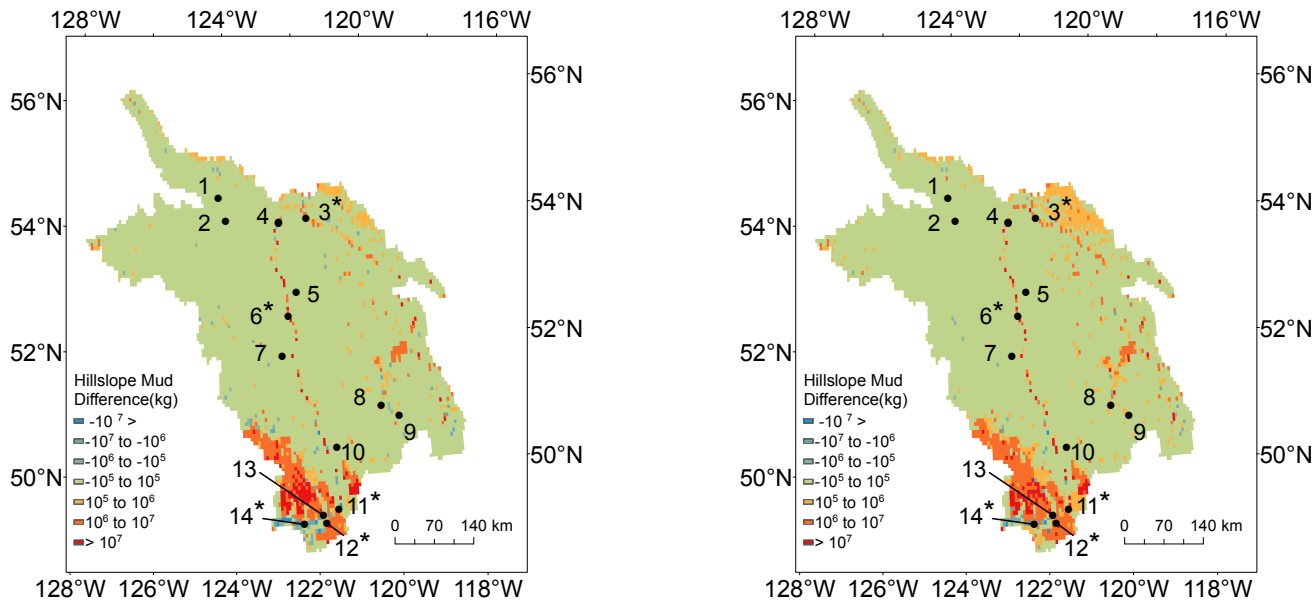

(a) GFDL2.1 Jan-Mar generation differences

(b) MIROC3.2 Jan-Mar generation differences

Figure A.5: Difference in Jan-Mar hillslope mud generation between future and baseline periods for A1B scenario for GCM models GFDL2.1 (a), and MIROC3.2 (b). Positive values indicate future values are larger than baseline values.

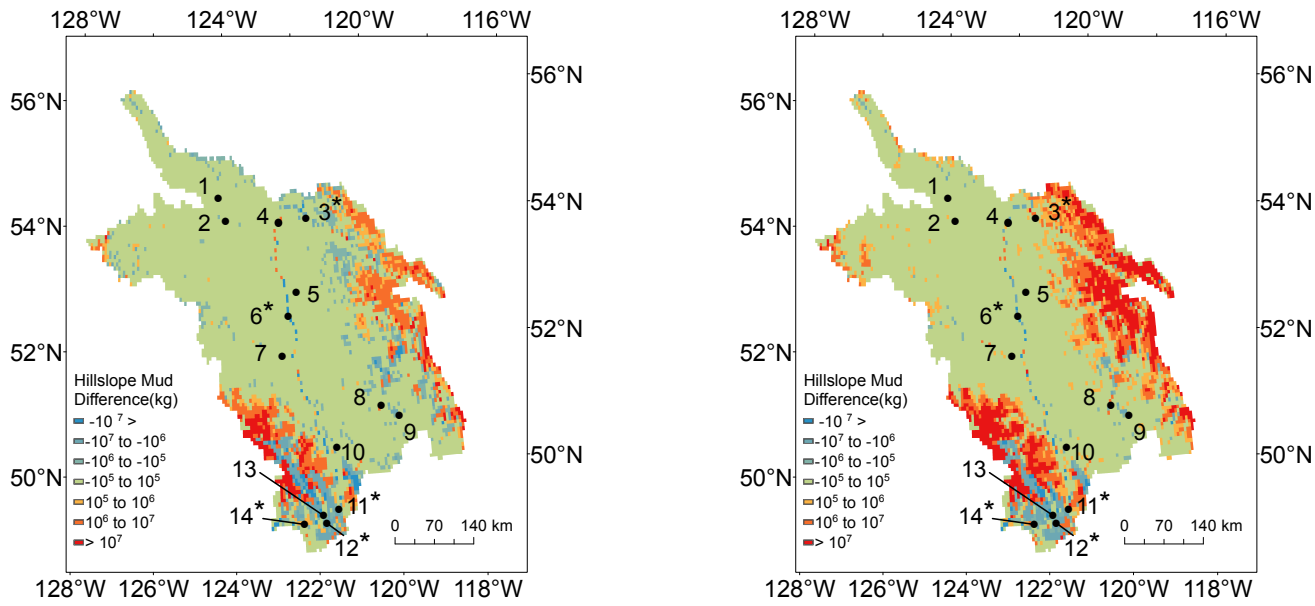

(a) GFDL2.1 Apr-Jun generation differences

(b) MIROC3.2 Apr-Jun generation differences

Figure A.6: Difference in Apr-Jun hillslope mud generation between future and baseline periods for A1B scenario for GCM models GFDL2.1 (a), and MIROC3.2 (b). Positive values indicate future values are larger than baseline values.

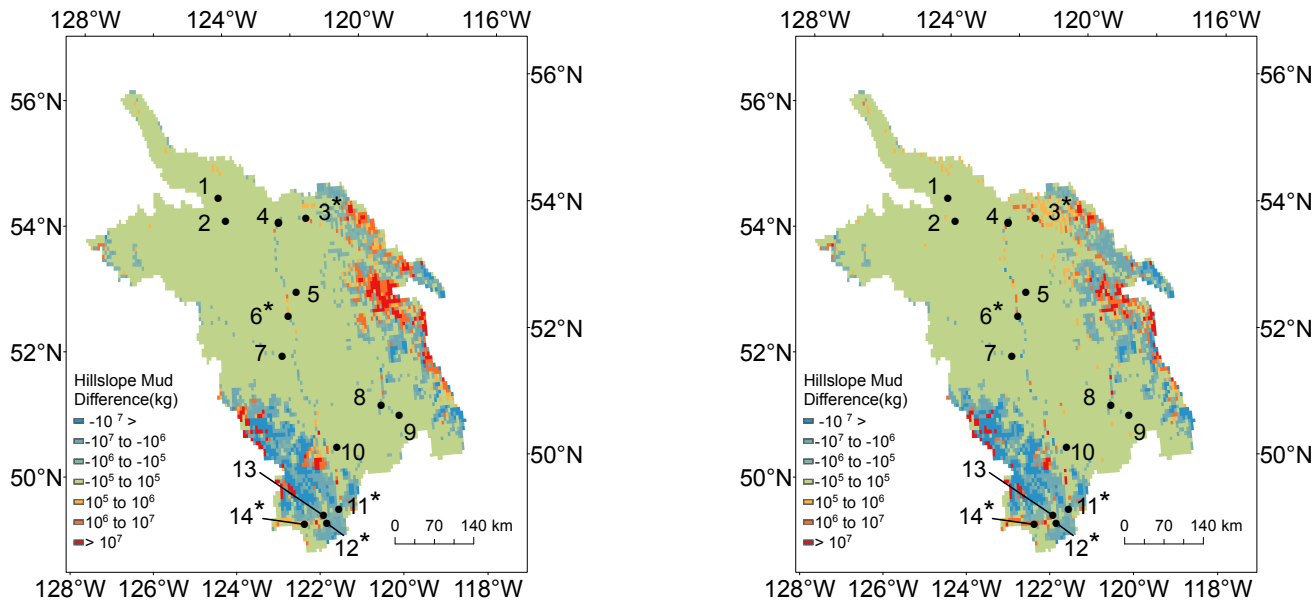

(a) GFDL2.1 Jul-Sep generation differences

(b) MIROC3.2 Jul-Sep generation differences

Figure A.7: Difference in Jul-Sep hillslope mud generation between future and baseline periods for A1B scenario for GCM models GFDL2.1 (a), and MIROC3.2 (b). Positive values indicate future values are larger than baseline values.

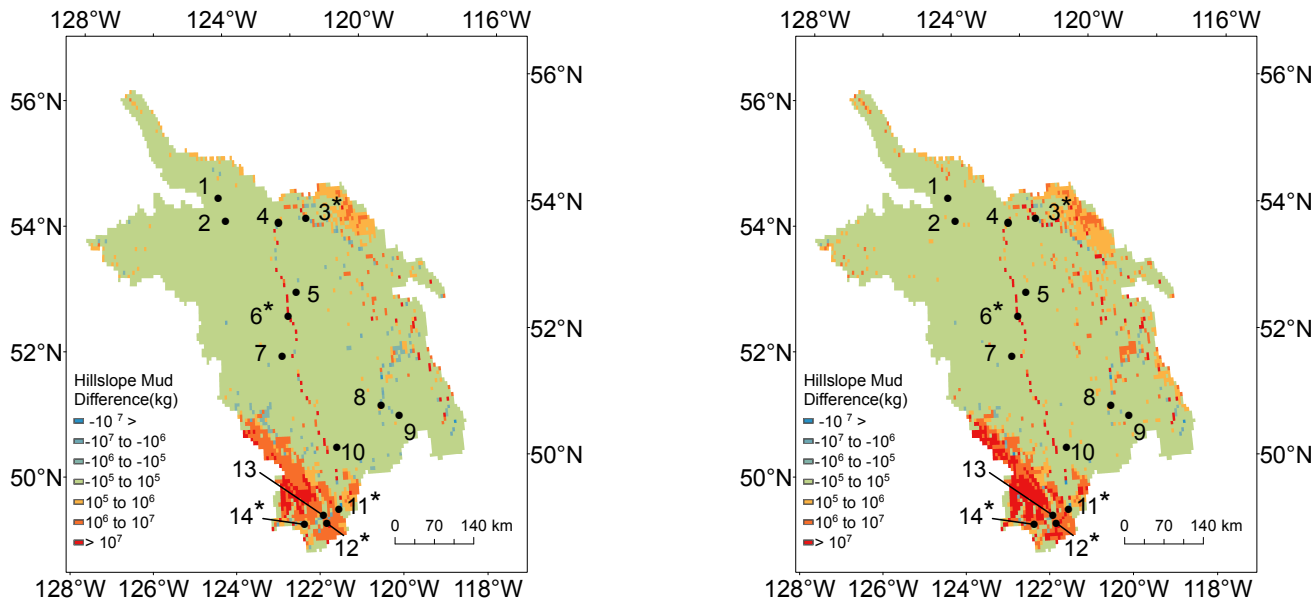

(a) GFDL2.1 Oct-Dec generation differences

(b) MIROC3.2 Oct-Dec generation differences

Figure A.8: Difference in Oct-Dec hillslope mud generation between future and baseline periods for A1B scenario for GCM models GFDL2.1 (a), and MIROC3.2 (b). Positive values indicate future values are larger than baseline values.

Appendix B

Storage: Additional Maps

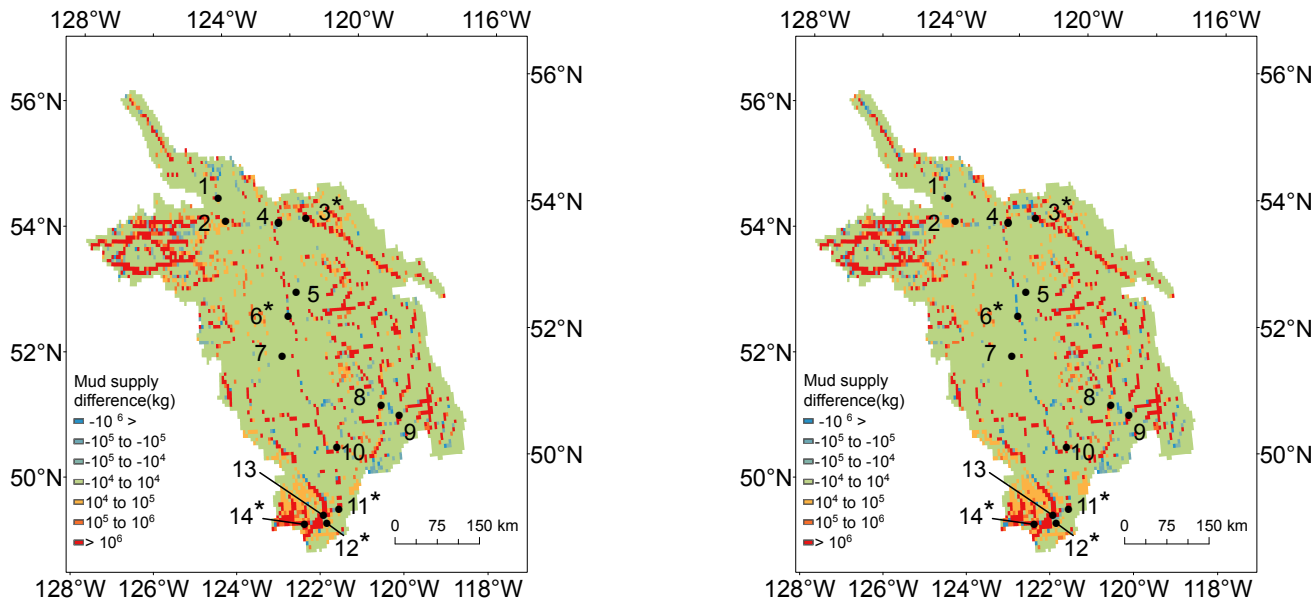

(a) B1 Jan-Mar storage differences

(b) A2 Jan-Mar storage differences

Figure B.1: Ensemble averaged difference in Jan-Mar sediment storage between future and baseline periods for scenarios B1 (a) and A2 (b). Positive values indicate future values are larger than baseline values.

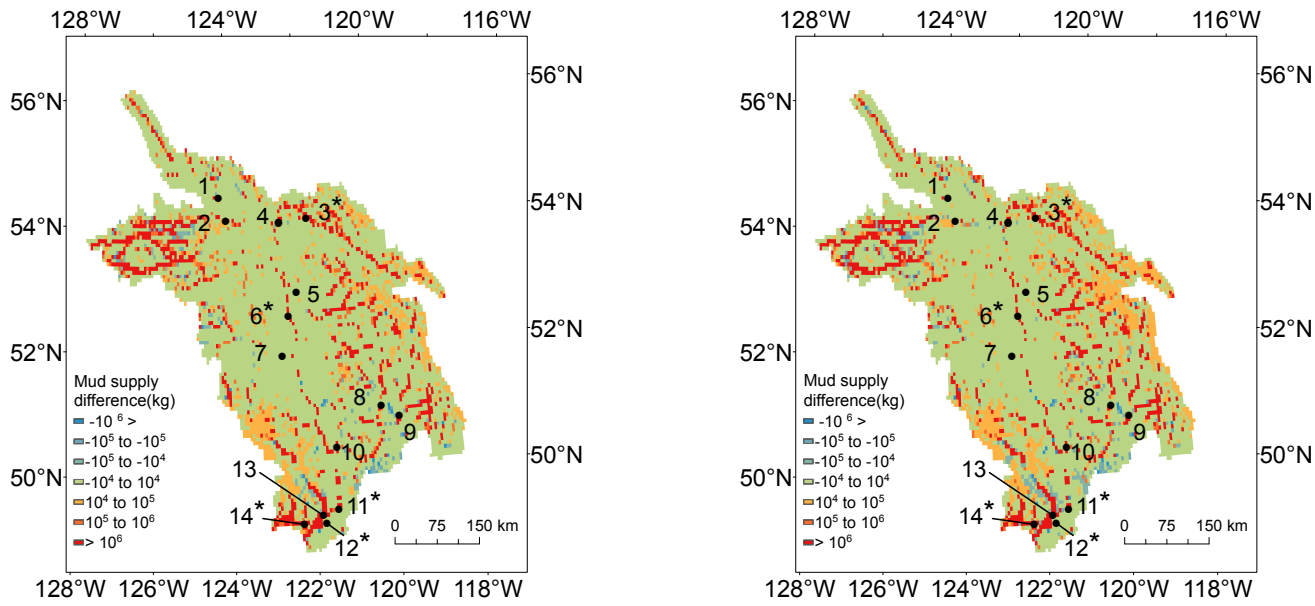

(a) B1 Apr-Jun storage differences

(b) A2 Apr-Jun storage differences

Figure B.2: Ensemble averaged difference in Apr-Jun sediment storage between future and baseline periods for scenarios B1 (a) and A2 (b). Positive values indicate future values are larger than baseline values.

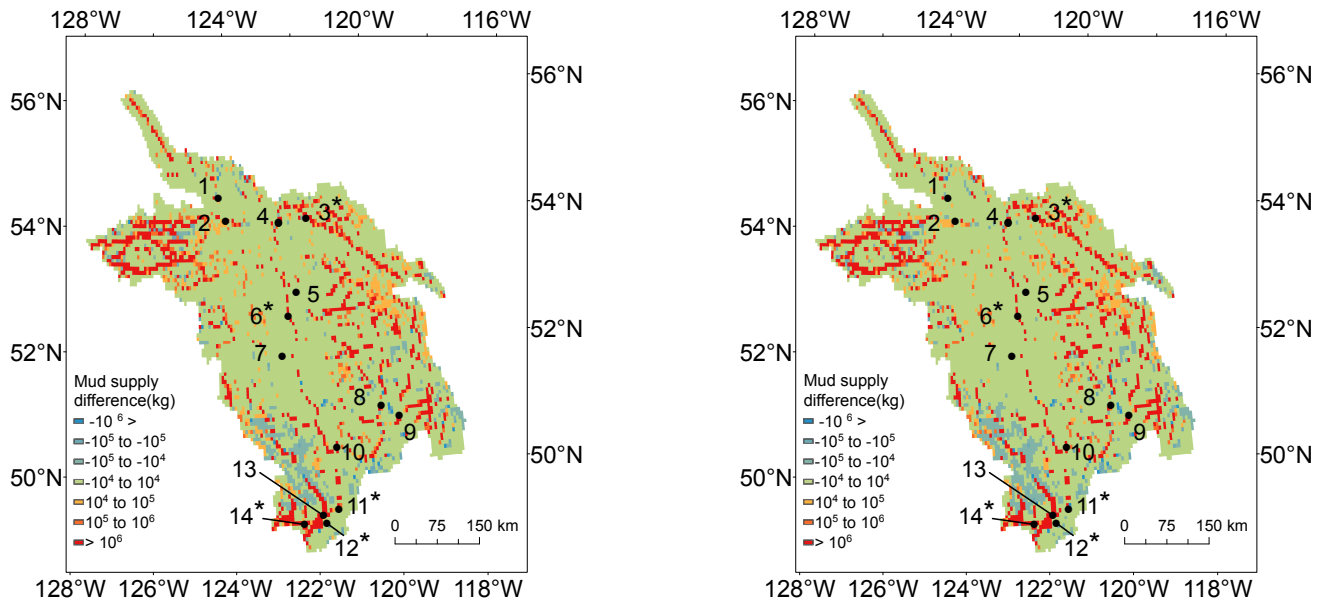

(a) B1 Jul-Sep storage differences

(b) A2 Jul-Sep storage differences

Figure B.3: Ensemble averaged difference in Jul-Sep sediment storage between future and baseline periods for scenarios B1 (a) and A2 (b). Positive values indicate future values are larger than baseline values.

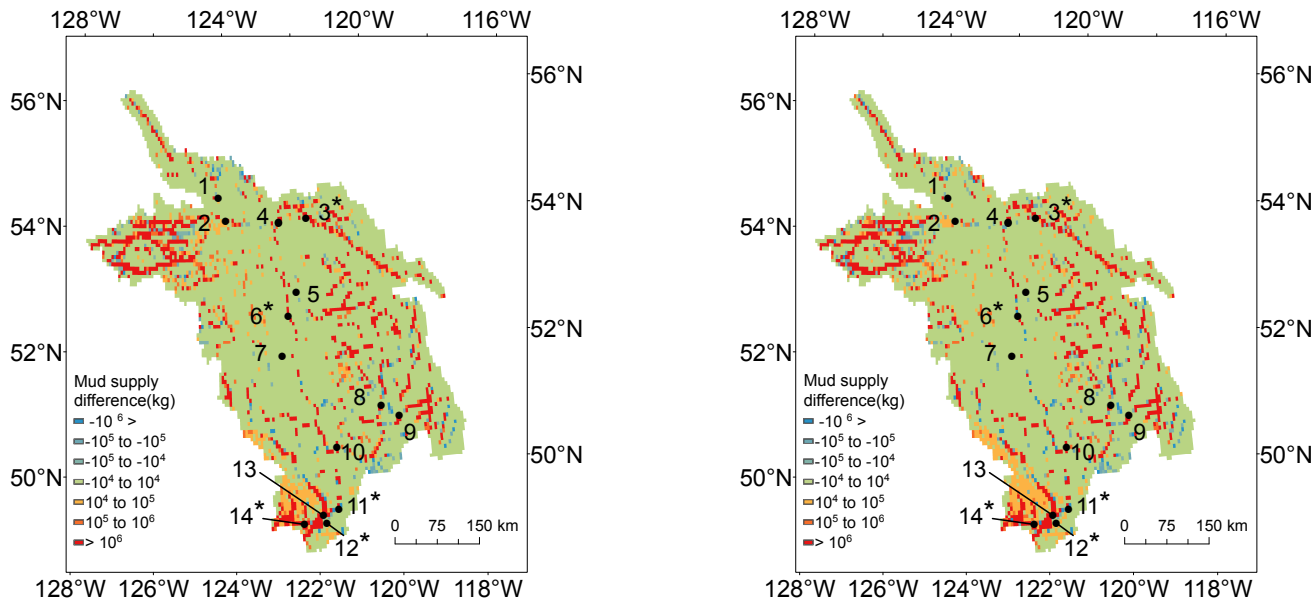

(a) B1 Oct-Dec storage differences

(b) A2 Oct-Dec storage differences

Figure B.4: Ensemble averaged difference in Oct-Dec sediment storage between future and baseline periods for scenarios B1 (a) and A2 (b). Positive values indicate future values are larger than baseline values.

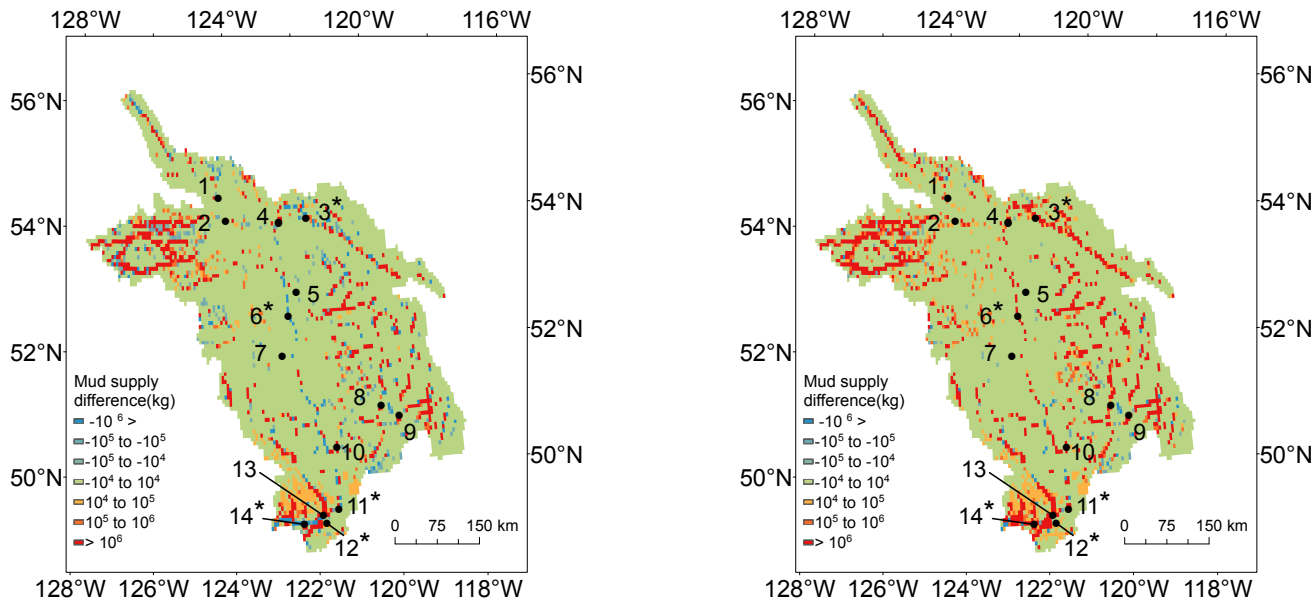

(a) GFDL2.1 Jan-Mar storage differences

(b) MIROC3.2 Jan-Mar storage differences

Figure B.5: Difference in Jan-Mar sediment storage between future and baseline periods for A1B scenario for GCM models GFDL2.1 (a), and MIROC3.2 (b). Positive values indicate future values are larger than baseline values.

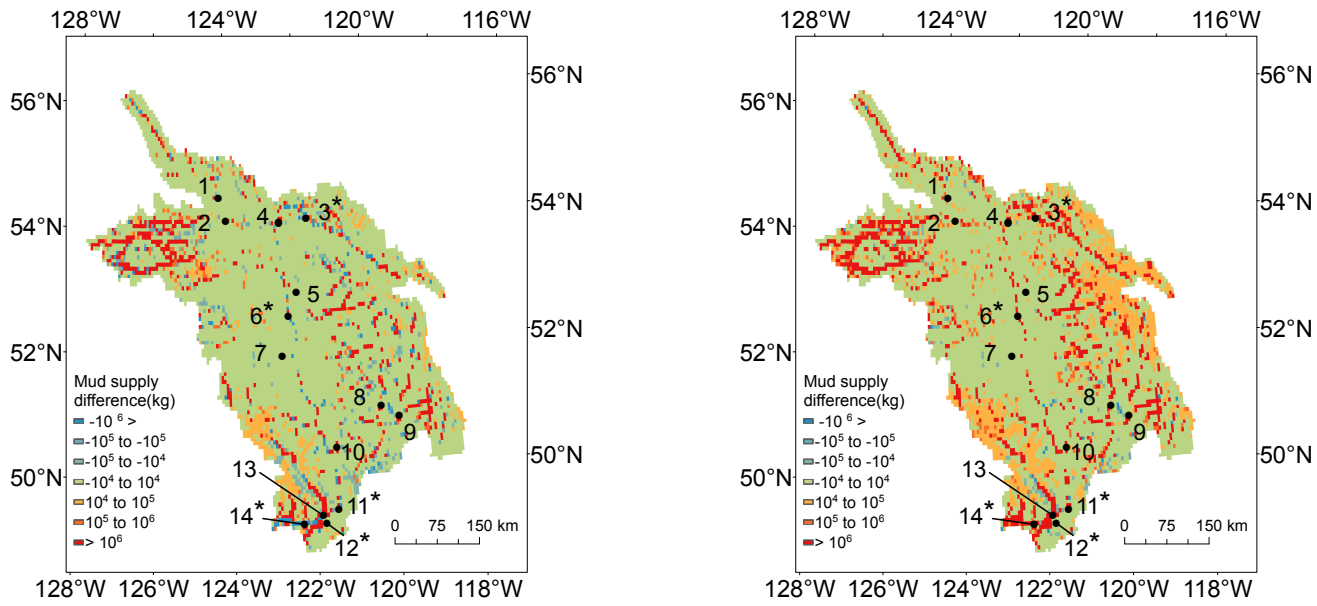

(a) GFDL2.1 Apr-Jun storage differences

(b) MIROC3.2 Apr-Jun storage differences

Figure B.6: Difference in Apr-Jun sediment storage between future and baseline periods for A1B scenario for GCM models GFDL2.1 (a), and MIROC3.2 (b). Positive values indicate future values are larger than baseline values.

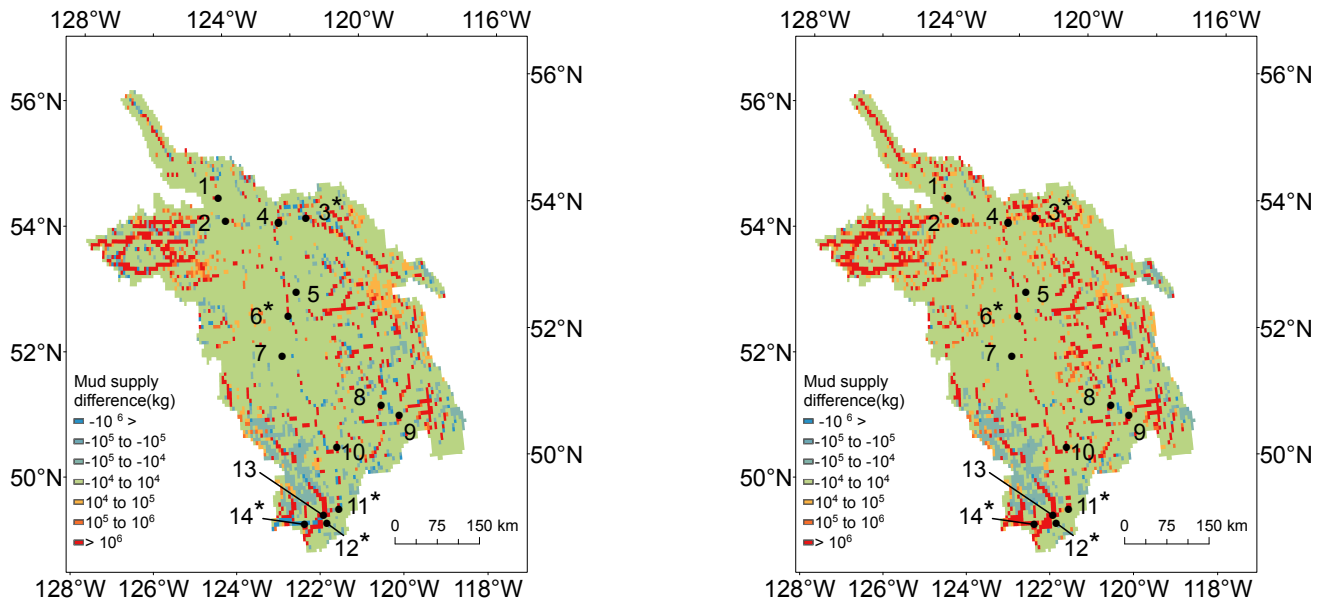

(a) GFDL2.1 Jul-Sep storage differences

(b) MIROC3.2 Jul-Sep storage differences

Figure B.7: Difference in Jul-Sep sediment storage between future and baseline periods for A1B scenario for GCM models GFDL2.1 (a), and MIROC3.2 (b). Positive values indicate future values are larger than baseline values.

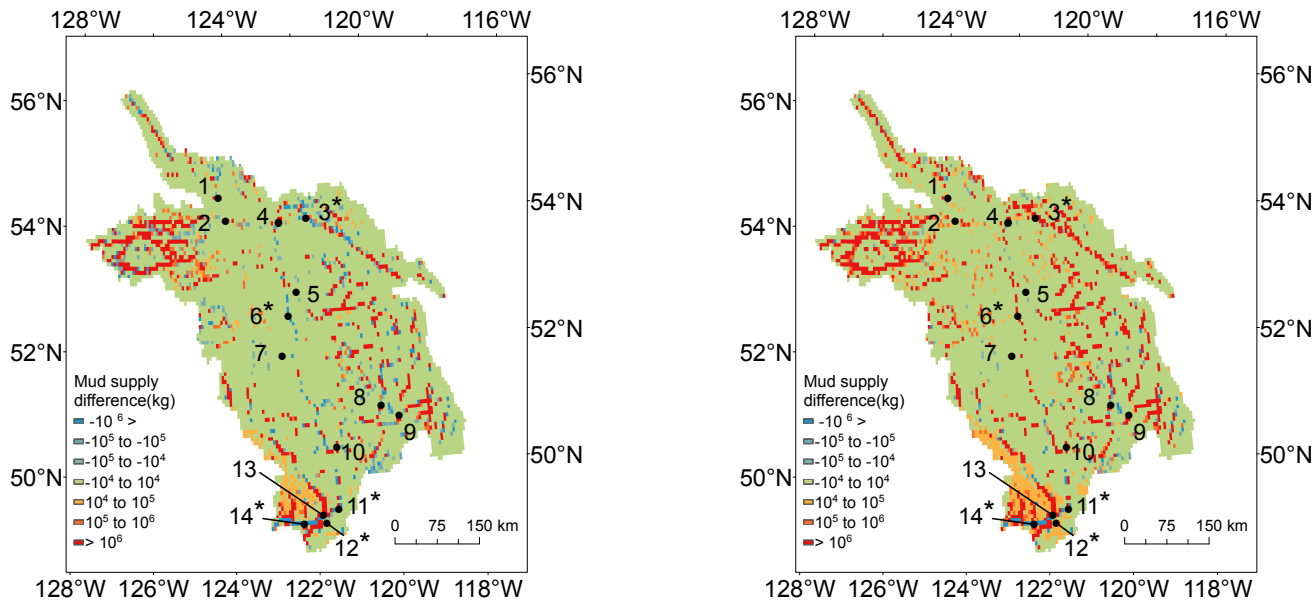

(a) GFDL2.1 Oct-Dec storage differences

(b) MIROC3.2 Oct-Dec storage differences

Figure B.8: Difference in Oct-Dec sediment storage between future and baseline periods for A1B scenario for GCM models GFDL2.1 (a), and MIROC3.2 (b). Positive values indicate future values are larger than baseline values.

Appendix C

Timing and Yield: Additional Tables and Graphs

Table C.1: Comparison of baseline and future projected values at Agassiz of average sediment spring, persistence, and centroid timing, and yield. "Δ" is computed as average future value minus average baseline value. Annual baseline yield at Agassiz was ∼15 Mt.

Agassiz

	Spring Timing			Persistence Timing		
Scenario	Δ(days)	Kτ	R^2	Δ(days)	Kτ	R^2
A1B	-39	0.79	0.84	54	0.07†	0.01†
A2	-43	0.64	0.69	51	-0.21†	0.01†
B1	-33	0.33†	0.80	32	0.04†	<0.01†
	Centroid Timing			Yield		
	Δ(days)	Kτ	R^2	Δ(Mt)	Kτ	R^2
A1B	-6	0.71	0.73	1.4	0.36†	0.23†
A2	-5†	-	-	2.0	0.86	0.84
B1	-10	0.62†	0.44†	1.9	0.71	0.79

† indicates values are **not** statistically significant ($\alpha = 0.05$).

Table C.2: Comparison of baseline and future projected values at Hope of average sediment spring, persistence, and centroid timing, and yield. "Δ" is computed as average future value minus average baseline value. Annual baseline yield at Hope was ∼15 Mt.

Hope

	Spring Timing			Persistence Timing		
Scenario	Δ(days)	Kτ	R^2	Δ(days)	Kτ	R^2
A1B	-41	0.79	0.85	53	0.14†	0.03†
A2	-45	0.71	0.74	50	0.00 †	<0.01†
B1	-33	0.43†	0.85	32	0.05†	<0.01†
	Centroid Timing			Yield		
	Δ(days)	Kτ	R^2	Δ(Mt)	Kτ	R^2
A1B	-10	0.57†	0.55	1.2†	-	-
A2	-10	0.57†	0.65	1.9	0.79	0.83
B1	-13	0.49†	0.51†	1.7	0.81	0.82

† indicates values are **not** statistically significant ($\alpha = 0.05$).

Table C.3: Comparison of baseline and future projected values at Marguerite of average sediment spring, persistence, and centroid timing, and yield. "Δ" is computed as average future value minus average baseline value. Annual baseline yield at Marguerite was ∼10 Mt.

Marguerite						
	Spring Timing			Persistence Timing		
Scenario	Δ(days)	Kτ	R^2	Δ(days)	Kτ	R^2
A1B	-42	0.79	0.79	29	0.57	0.86
A2	-46	1.00	0.93	30	0.57	0.54
B1	-32	0.90	0.98	20	0.43†	0.53†
	Centroid Timing			Yield		
	Δ(days)	Kτ	R^2	Δ(Mt)	Kτ	R^2
A1B	-15	0.86	0.95	2.2	0.50†	0.29†
A2	-17	0.86	0.88	2.8	0.71	0.88
B1	-15	0.52†	0.82	2.1	0.52†	0.65

† indicates values are **not** statistically significant ($\alpha = 0.05$).

Table C.4: Comparison of baseline and future projected values at Nechako of average sediment spring, persistence, and centroid timing, and yield. "Δ" is computed as average future value minus average baseline value. Annual baseline yield at Nechako was ∼15 Kt.

Nechako						
	Spring Timing			Persistence Timing		
Scenario	Δ(days)	Kτ	R^2	Δ(days)	Kτ	R^2
A1B	-75	-0.29†	0.07†	64	0.47†	0.17†
A2	-75	-0.21†	0.06†	63	-0.21†	0.06†
B1	-71	0.33†	0.01†	62	0.24†	0.29†
	Centroid Timing			Yield		
	Δ(days)	Kτ	R^2	Δ(Kt)	Kτ	R^2
A1B	-15	0.29†	0.25†	151	0.71	0.76
A2	-17	0.18†	0.06†	154	0.71	0.85
B1	-12	0.24†	0.30†	150	0.24†	0.58

† indicates values are **not** statistically significant ($\alpha = 0.05$).

Table C.5: Comparison of baseline and future projected values at North Thompson of average sediment spring, persistence, and centroid timing, and yield. "Δ" is computed as average future value minus average baseline value. Annual baseline yield at North Thompson was ∼2 Mt.

North Thompson

	Spring Timing			Persistence Timing		
Scenario	Δ(days)	Kτ	R^2	Δ(days)	Kτ	R^2
A1B	-33	0.64	0.43†	7†	-	-
A2	-40	0.57†	0.61	8†	-	-
B1	-26	0.62†	0.81	<1†	-	-
	Centroid Timing			Yield		
	Δ(days)	Kτ	R^2	Δ(Kt)	Kτ	R^2
A1B	-17	0.71	0.84	220	0.93	0.92
A2	-20	0.64	0.83	280	1.00	0.93
B1	-16	0.43†	0.70	200	0.90	0.91

† indicates values are **not** statistically significant ($\alpha = 0.05$).

Table C.6: Comparison of baseline and future projected values at Quesnel of average sediment spring, persistence, and centroid timing, and yield. "Δ" is computed as average future value minus average baseline value. Annual baseline yield at Quesnel was ∼0.5 Mt.

Quesnel

	Spring Timing			Persistence Timing		
Scenario	Δ(days)	Kτ	R^2	Δ(days)	Kτ	R^2
A1B	-45	0.43†	0.30†	27	0.64	0.52
A2	-52	0.50†	0.41†	27	0.57†	0.69
B1	-36	0.62†	0.41†	16	0.33†	0.30†
	Centroid Timing			Yield		
	Δ(days)	Kτ	R^2	Δ(Kt)	Kτ	R^2
A1B	-22	0.79	0.74	83	0.57†	0.60
A2	-24	0.79	0.91	92	0.79	0.73
B1	-19	0.71	0.88	68	0.71	0.78

† indicates values are **not** statistically significant ($\alpha = 0.05$).

Table C.7: Comparison of baseline and future projected values at Shelley of average sediment spring, persistence, and centroid timing, and yield. "Δ" is computed as average future value minus average baseline value. Annual baseline yield at Shelley was ∼3 Mt.

Shelley						
	Spring Timing			Persistence Timing		
Scenario	Δ(days)	Kτ	R^2	Δ(days)	Kτ	R^2
A1B	-23	0.18†	0.07†	41	0.07 †	<0.01†
A2	-29	0.43†	0.07†	54	0.00†	0.06†
B1	-21	0.43†	0.43†	27	0.62†	0.28†
	Centroid Timing			Yield		
	Δ(days)	Kτ	R^2	Δ(Mt)	Kτ	R^2
A1B	-13	0.21†	0.10†	1.8	0.57†	0.48†
A2	-14	0.64	0.48†	1.9	0.64	0.59
B1	-13	0.43†	0.52†	1.5	0.52†	0.61

† indicates values are **not** statistically significant ($\alpha = 0.05$).

Table C.8: Comparison of baseline and future projected values at South Thompson of average sediment spring, persistence, and centroid timing, and yield. "Δ" is computed as average future value minus average baseline value.

South Thompson						
	Spring Timing			Persistence Timing		
Scenario	Δ(days)	Kτ	R^2	Δ(days)	Kτ	R^2
A1B	-31	0.43†	0.38†	23	0.71	0.66
A2	-38	0.64	0.54	24	0.71	0.64
B1	-25	0.81	0.92	7†	-	-
	Centroid Timing			Yield		
	Δ(days)	Kτ	R^2	Δ(Kt)	Kτ	R^2
A1B	-20	0.64	0.82	10†	-	-
A2	-22	0.62	0.82	14†	-	-
B1	-17	0.71	0.92	4†	-	-

† indicates values are **not** statistically significant ($\alpha = 0.05$).

Table C.9: Comparison of baseline and future projected values at Stuart of average sediment spring, persistence, and centroid timing, and yield. "Δ" is computed as average future value minus average baseline value. Annual baseline yield at Stuart was ∼0.5 Kt.

Stuart

	Spring Timing			Persistence Timing		
Scenario	Δ(days)	Kτ	R^2	Δ(days)	Kτ	R^2
A1B	-28	0.50†	0.63	4†	-	-
A2	-30	0.84	0.57	1†	-	-
B1	-23	0.43†	0.80	2†	-	-
	Centroid Timing			Yield		
	Δ(days)	Kτ	R^2	Δ(t)	Kτ	R^2
A1B	-37	1.00	0.94	80	0.93	0.99
A2	-39	0.86	0.97	90	0.86	0.99
B1	-27	0.81	0.98	66	0.71	0.97

† indicates values are **not** statistically significant ($\alpha = 0.05$).

Table C.10: Comparison of baseline and future projected values at Thompson of average sediment spring, persistence, and centroid timing, and yield. "Δ" is computed as average future value minus average baseline value. Annual baseline yield at Thompson was ∼2 Mt

Thompson

	Spring Timing			Persistence Timing		
Scenario	Δ(days)	Kτ	R^2	Δ(days)	Kτ	R^2
A1B	-50	0.79	0.74	12	0.71	0.76
A2	-55	0.71	0.78	15	0.64	0.66
B1	-36	0.71	0.88	1†	-	-
	Centroid Timing			Yield		
	Δ(days)	Kτ	R^2	Δ(Kt)	Kτ	R^2
A1B	-25	0.71	0.74	-160†	-	-
A2	-28	0.93	0.97	-130†	-	-
B1	-20	0.24†	0.76	-50†	-	-

† indicates values are **not** statistically significant ($\alpha = 0.05$).

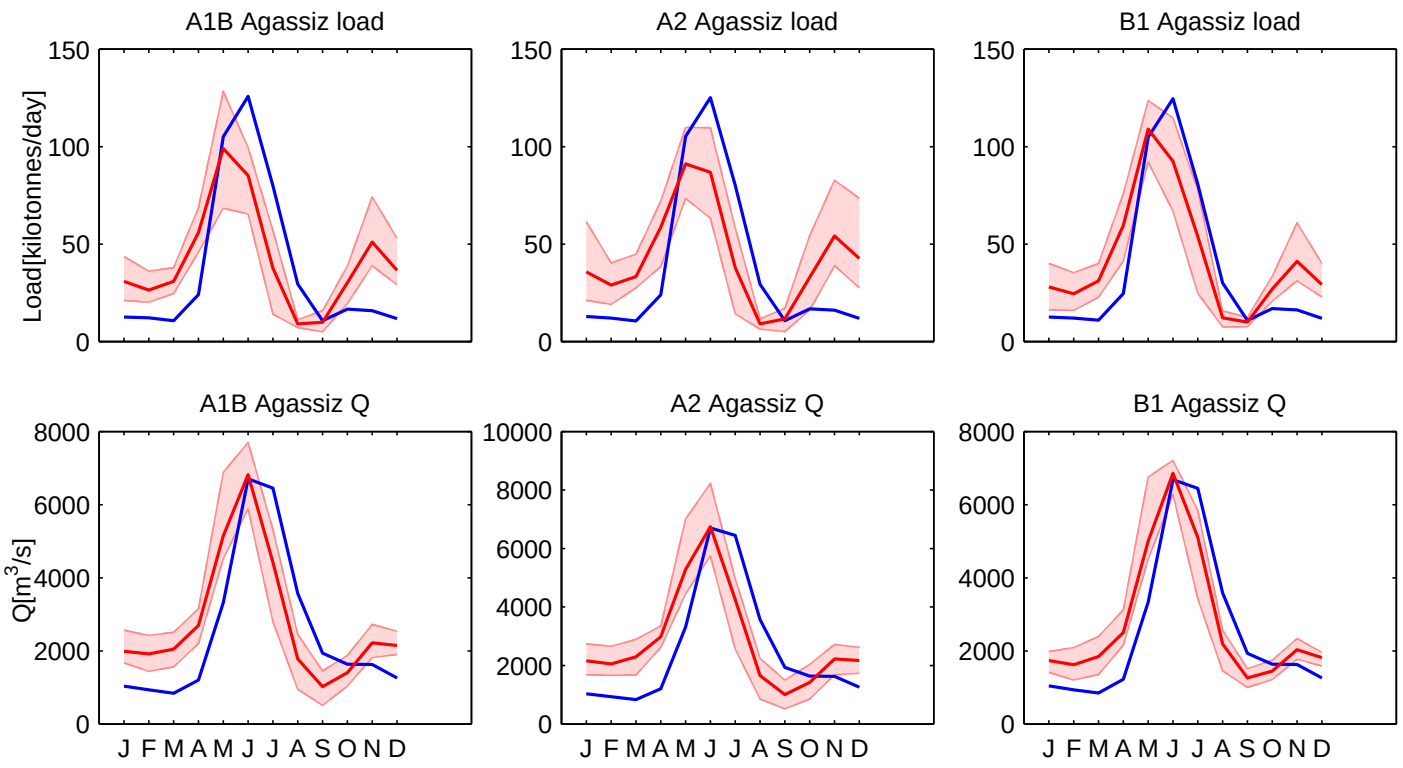

Figure C.1: Seasonal Q and suspended sediment load at Agassiz for scenarios A1B, A2, and B1 for baseline (blue line) and future ensemble mean (red line) and future ensemble range (red region).

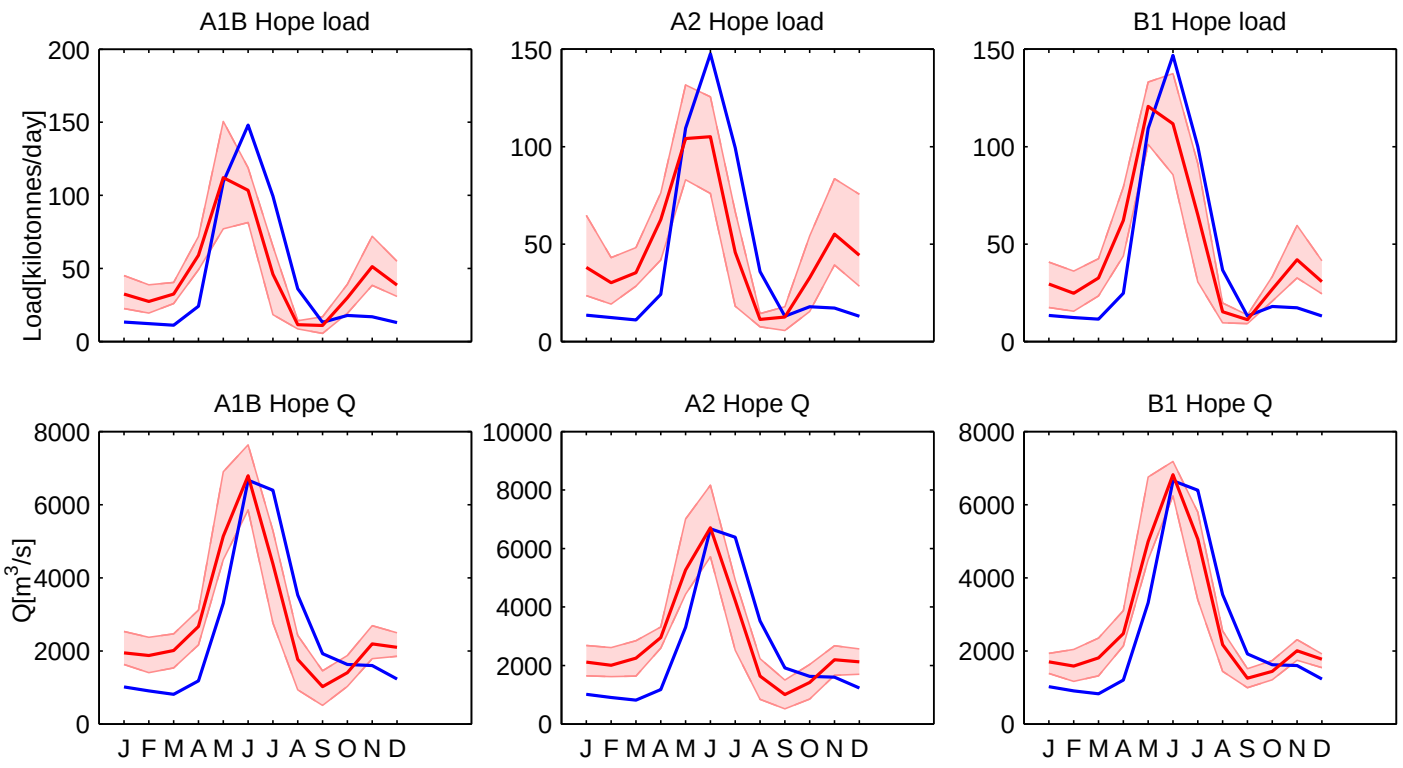

Figure C.2: Seasonal Q and suspended sediment load at Hope for scenarios A1B, A2, and B1 for baseline (blue line) and future ensemble mean (red line) and future ensemble range (red region).

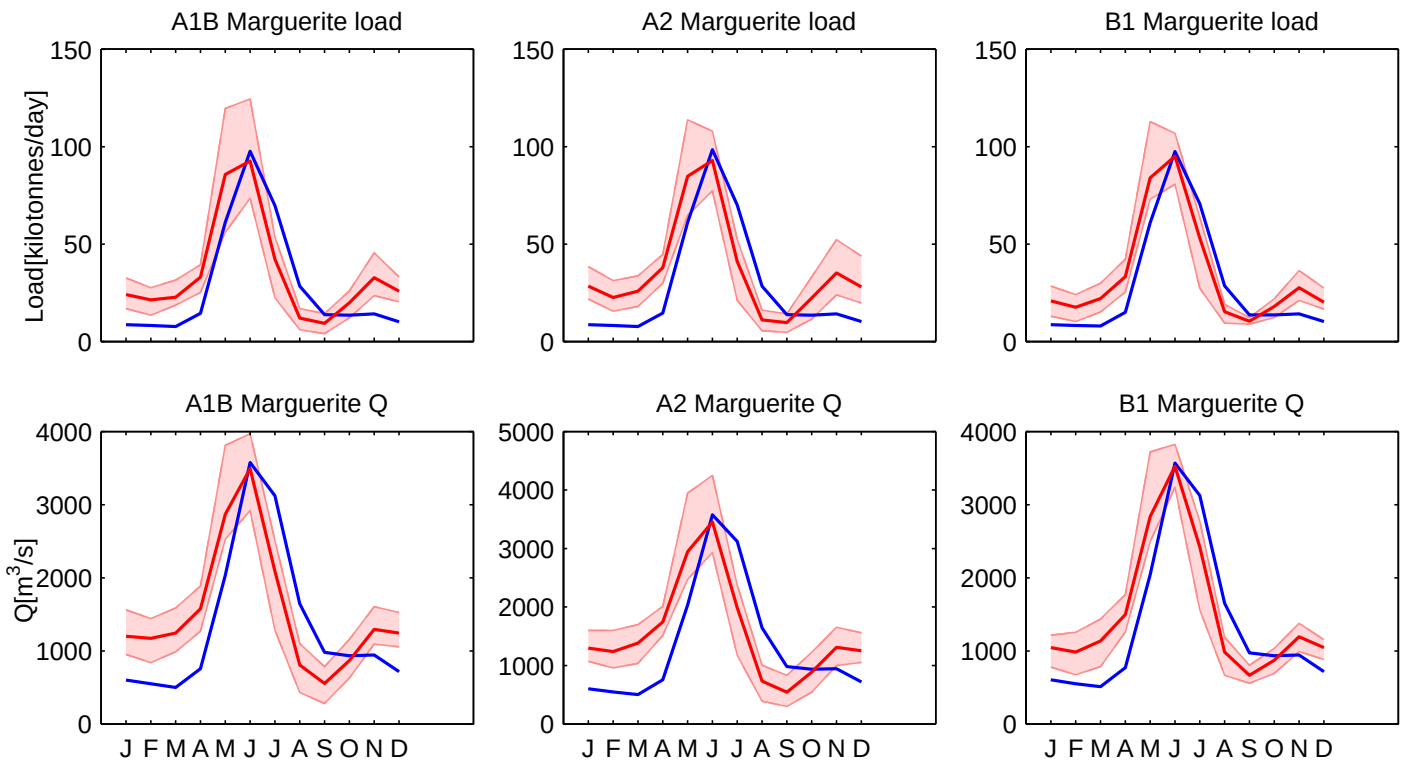

Figure C.3: Seasonal Q and suspended sediment load at Marguerite for scenarios A1B, A2, and B1 for baseline (blue line) and future ensemble mean (red line) and future ensemble range (red region).

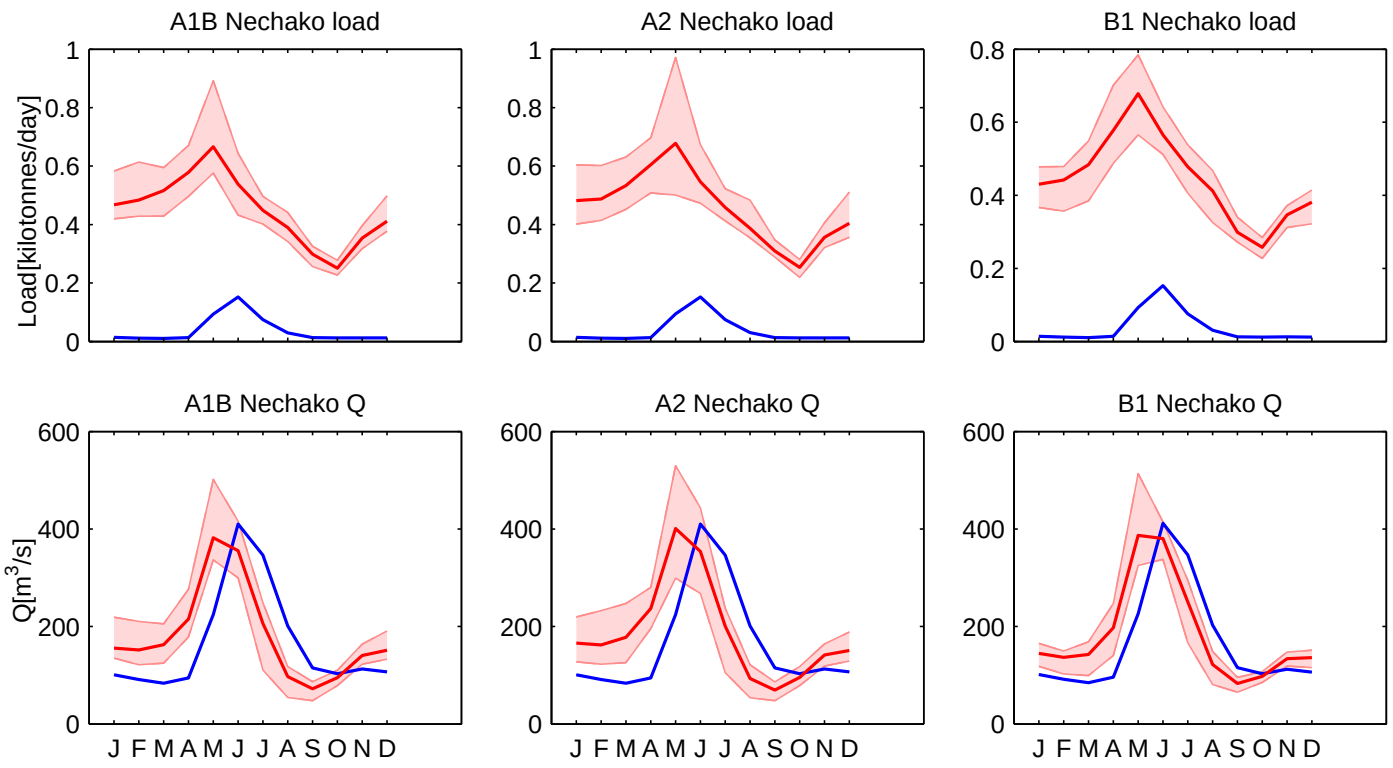

Figure C.4: Seasonal Q and suspended sediment load at Nechako for scenarios A1B, A2, and B1 for baseline (blue line) and future ensemble mean (red line) and future ensemble range (red region).

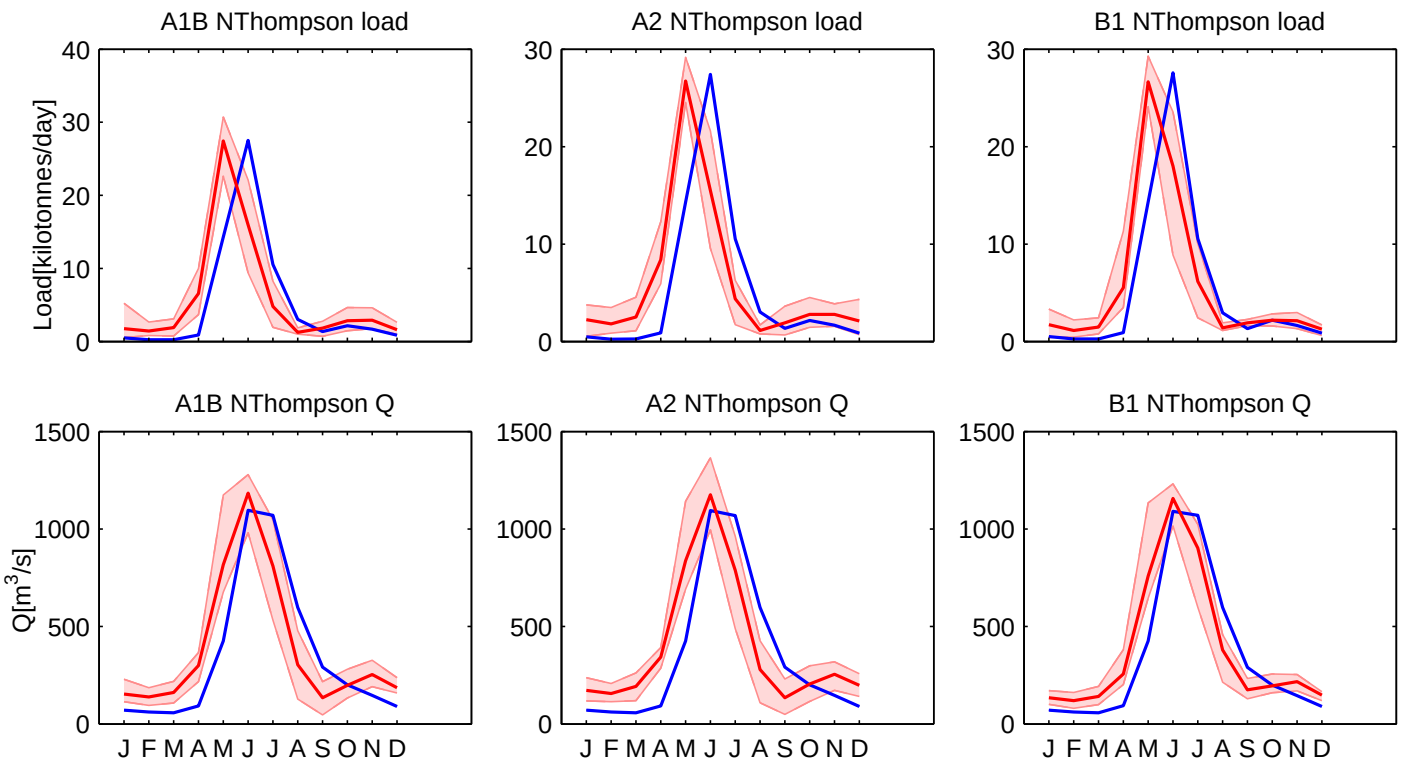

Figure C.5: Seasonal Q and suspended sediment load at North Thompson for scenarios A1B, A2, and B1 for baseline (blue line) and future ensemble mean (red line) and future ensemble range (red region).

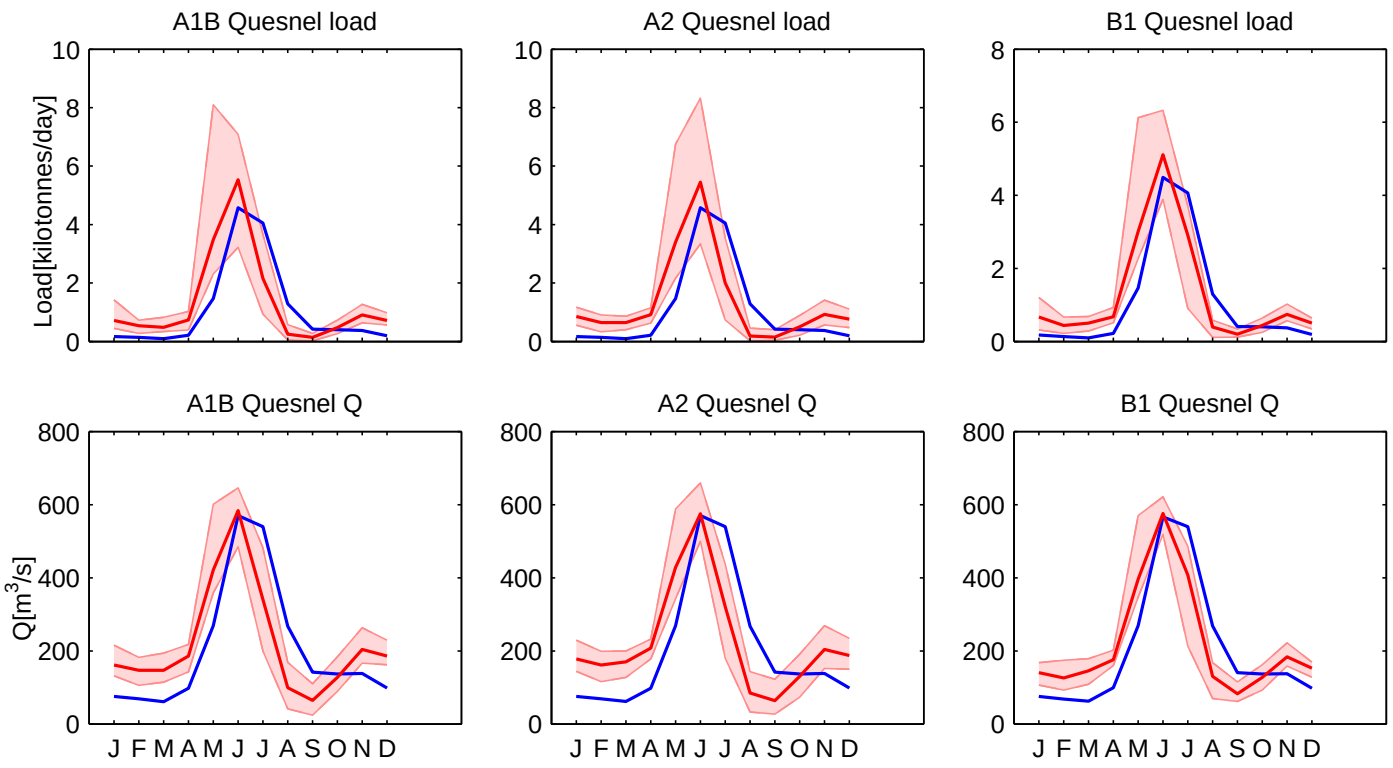

Figure C.6: Seasonal Q and suspended sediment load at Quesnel for scenarios A1B, A2, and B1 for baseline (blue line) and future ensemble mean (red line) and future ensemble range (red region).

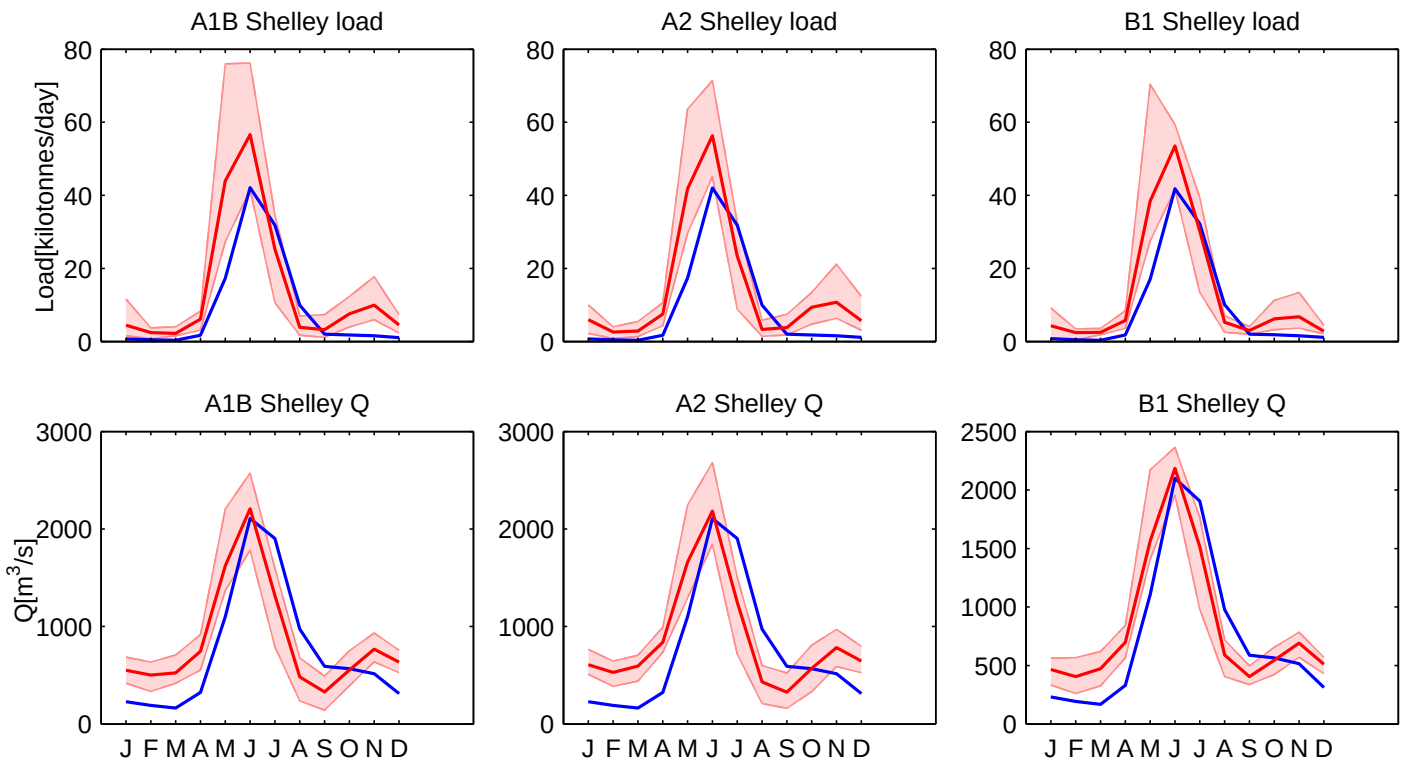

Figure C.7: Seasonal Q and suspended sediment load at Shelley for scenarios A1B, A2, and B1 for baseline (blue line) and future ensemble mean (red line) and future ensemble range (red region).

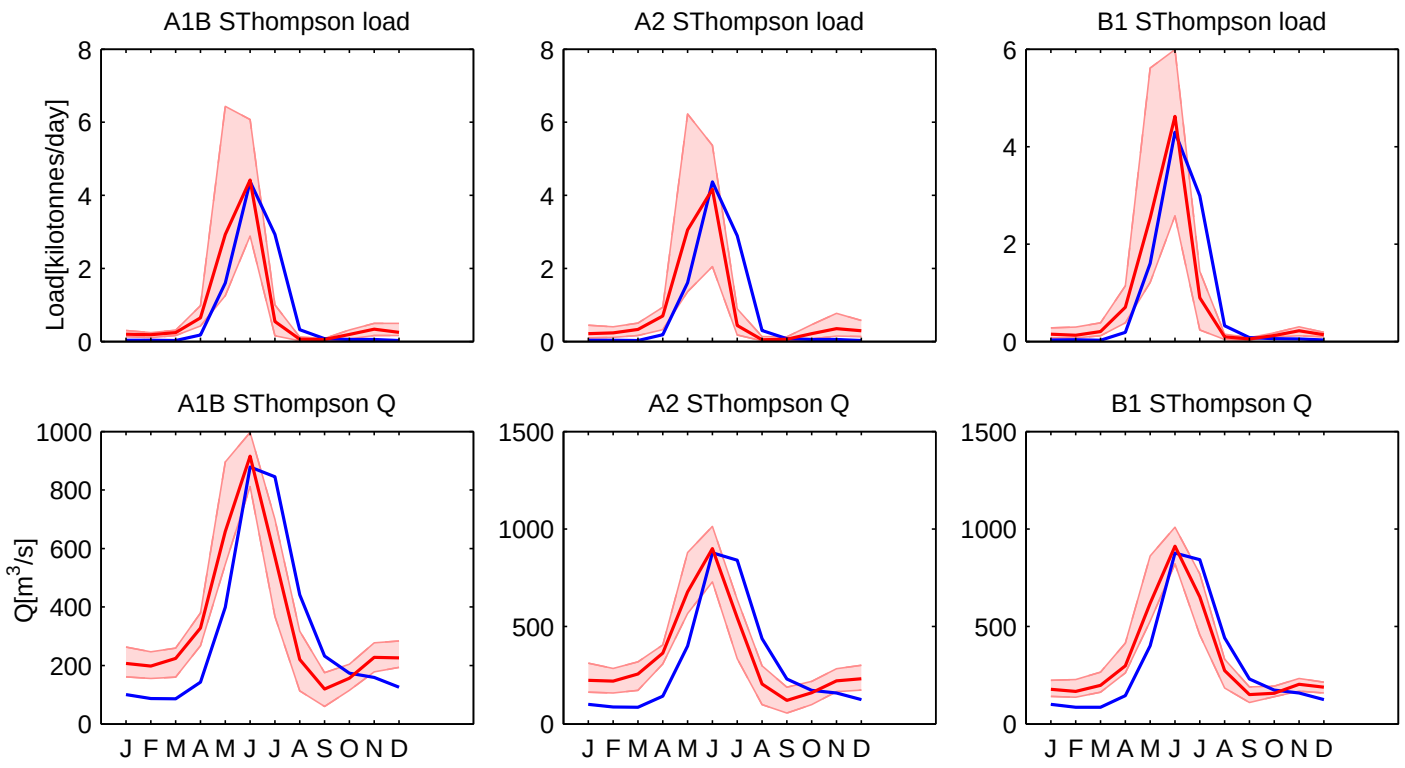

Figure C.8: Seasonal Q and suspended sediment load at South Thompson for scenarios A1B, A2, and B1 for baseline (blue line) and future ensemble mean (red line) and future ensemble range (red region).

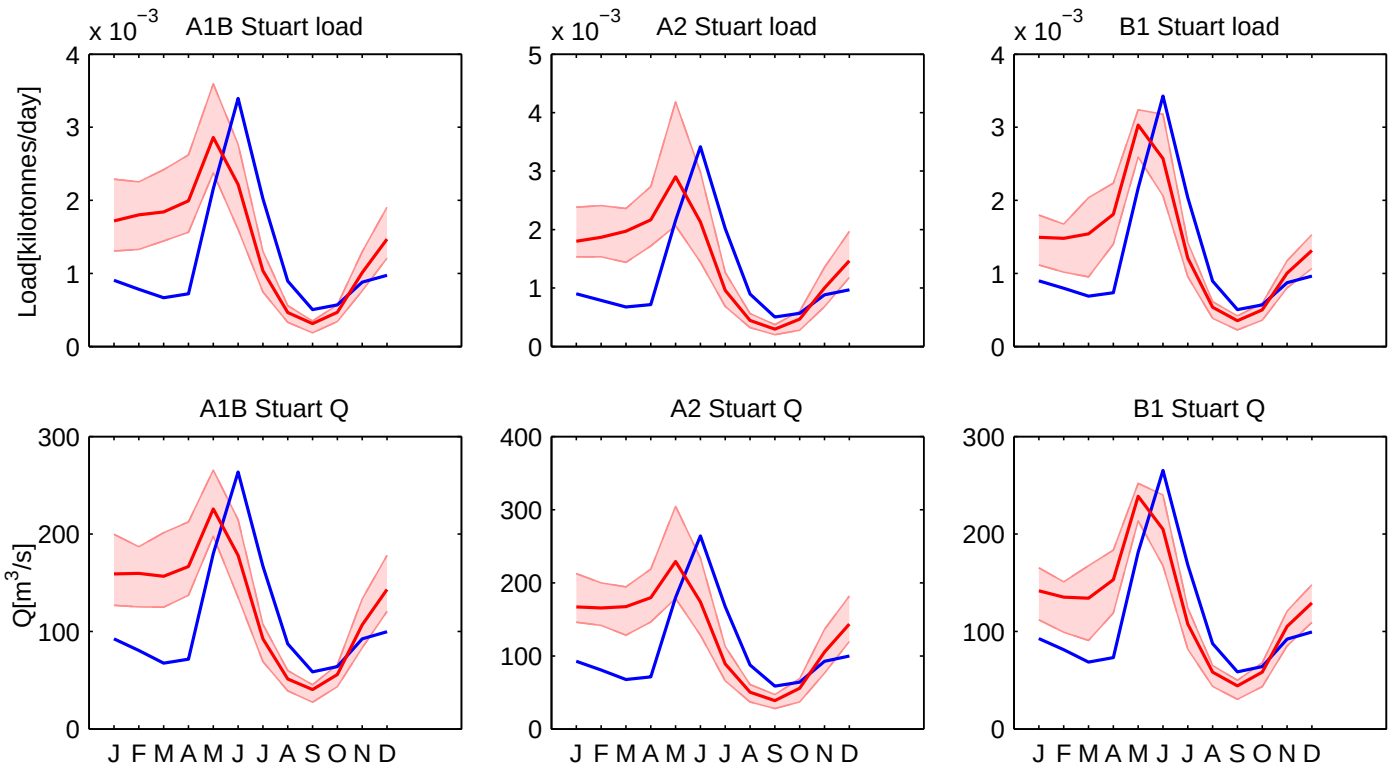

Figure C.9: Seasonal Q and suspended sediment load at Stuart for scenarios A1B, A2, and B1 for baseline (blue line) and future ensemble mean (red line) and future ensemble range (red region).

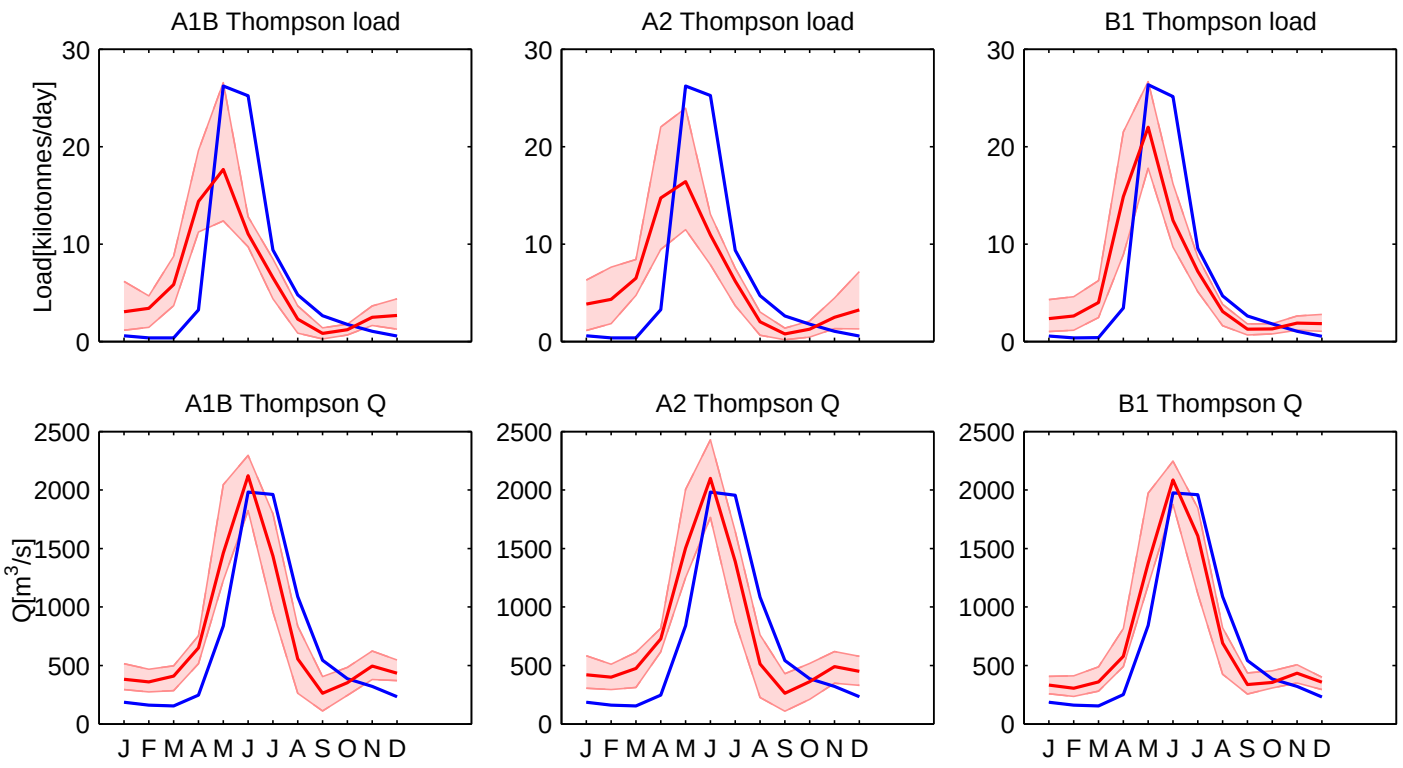

Figure C.10: Seasonal Q and suspended sediment load at Thompson for scenarios A1B, A2, and B1 for baseline (blue line) and future ensemble mean (red line) and future ensemble range (red region).